AD-A046 293 GTE SYLVANIA INC NEEDHAM HEIGHTS MASS ELECTRONIC SYS--ETC F/G 9/3
CPMFSK AS A MODULATION ON THE VLF-HF ATMOSPHERIC CHANNEL.(U)
OCT 77 T A SCHONHOFF F30602-76-C-0410

UNCLASSIFIED RADC-TR-77-318 NL

2 OF 2
ADA
046293



END
DATE
FILMED
12-77
DDC

References

1. R. R. Anderson and J. Salz, "Spectra of Digital FM", BSTJ, Vol. 44, pp. 1165-1189, July-August 1965.

2. W. P. Osborne and M. B. Luntz, "Coherent and Noncoherent Detection of CPFSK", IEEE Trans. Comm., COM-22, #8, August 1974, pp. 1023-1036.

3. T. A. Schonhoff, "Symbor Error Probabilities for M-ary Coherent Continuous Phase Frequency Shift Keying", ICC 1975 Conf. Recd., pp 34-5 to 34-8.

4. T. A. Schonhoff, "Symbol Error Probabilities for M-ary CPFSK: Coherent and noncoherent Detection", IEEE Trans. Comm., COM-24, #6, June 1976.

5. J. T. Gamble, "Linear Detection of Coherent FSK (CFSK) and MSK Signals in Low Frequency Atmospheric Noise", ICC 1975 Conf. Recd., pp. 34-14 to 34-18.

6. "World Distributions and Characteristics of Atmospheric Radio Noise", CCIR Report 322, 1964, Figure 27.

7. G. D. Forney, Jr., "The Viterbi Algorithm", Proc. IEEE, Vol. 61, No. 3, March 1973, pp. 268-278.

8. A. D. Whalen, Detection of Signals in Noise, Academic Press: New York, 1971.

9. J. N. Craig, Design of Lossy Filters, M.I.T. Press, Cambridge, Mass. 1970.

10. A. J. Viterbi, "Error Bounds for Convolutional Codes and an Asymptotically Optimum Decoding Algorithm", IEEE Trans. Int. Thy., IT-13, April 1967, pp. 260-269.

11. T. A. Schonhoff, "Bandwidth vs. Performance Considerations for CPFSK", NTC 1975 Conf. Recd., pp. 38-1 to 38-5.

12. H. M. Hall, Jr., "A New Model for 'Impulsive' Phenomena: Application to Atmospheric-Noise Communication Channels," Ph.D. dissertation, Stanford University, August 1966.

13. A. Giordano et al., "Interference Mitigation Techniques Program", interim report under contract N00014-76-C-0468 sponsored by ARPA.

14. J. W. Modestino and A. H. Levesque, private correspondence.

15. O. Ibukun, "Structural Aspects of Atmospheric Radio Noise in the Tropics," Proc. IEEE, Vol. 54, No. 3, March 1966, pp. 361-367.

16. J. W. Modestino, "Locally Optimum Receiver Structures for Known Signals in Non-Gaussian Narrowband Noise", 13th Annual Allerton Conf. on Ckt. and System Theory, Oct. 1975.

17. I. S. Gradshteyn and I. M. Ryzhik, Tables of Integrals, Series, and Products, Academic Press: New York, 1965.

18. W. Q. Crichlow et al., "Determination of the Amplitude-Probability Distribution of Atmospheric Radio Noise From Statistical Moments", Journal of Research, National Bureau of Standards - D: Radio Propagation, Vol. 64D, 1960, pp. 49-56.

19. K. E. Wilson, "Analysis of the Crichlow Graphical Model of Atmospheric Radio Noise at Very Low Frequencies", M. S. Thesis, Air Force Institute of Technology, Nov. 1974.

20. A. D. Spaulding, C. J. Roubique, and W. A. Crichlow, "Conversion of the Amplitude-Probability Distribution Function for Atmospheric Radio Noise from One Bandwidth to Another," Journal of Research, National Bureau of Standards - D Radio Propagation, Vol. 66D, No. 6, Nov.-Dec. 1962.

21. J. T. Gamble, "An Analysis of Linear and Nonlinear Coherent Detection in Atmospheric Noise At Very Low Frequency", Ph.D dissertation, Syracuse University, 1974.

22. A. Shohara, "VLF/LF Modem Performance in Atmospheric Noise-Volume 1: Theoretical Analysis", Interim Final Report, January 1976, DCA 100-75-C-0013.

23. C. D. Beach and D. C. George, "Error Performance of VLF and LF Receiving Systems with Nonlinear Atmospheric Noise Reduction", RADC-TR-70-190, Westinghouse Electric Corp., Sept. 1970. (AD875991)

24. M. G. Pelchat, R. C. Davis, and M. B. Luntz, "Coherent Demodulation of Continuous Phase Binary FSK Signals", 1972 Int. Telemetering Conf., pp. 181-190.

25. O. Y. Antonov, "Optimum Detection of Signals in Non-Gaussian Noise", Radio Eng. and Electronic Physics, V. 12, April 1967, pp. 541-548.

26. S. S. Rappaport and L. Kurz, "An Optimal Nonlinear Detection for Digital Data Transmission Through Non-Gaussian Channels", IEEE Trans. Comm., COM-14, No. 3, June 1966, pp. 266-274.

27. M. Abramowitz and I. A. Stegun, Handbook of Mathematical Functions, National Bureau of Standards, AMS 55.

28. A. Papoulis, Probability, Random Variables and Stochastic Processes, McGraw-Hill, New York: 1965, Section 7.2.

Appendix A

Selected Theoretical Results

This Appendix contains details of the theoretical effort. The emphasis here is the general determination of the probability of error when the received signal has been processed in a bandpass nonlinearity followed by a linear receiver. The basic approach that has been chosen is to model the output of the linear receiver as a finite sum of random variables (note: they need not be independent nor identically distributed). As explained in Section 5.1.2, we can define a variable . (Eq. 78)

$$y = \sum_{\ell=o}^{L} a_\ell y_\ell \tag{A1}$$

where

$$y_\ell = \xi(t_\ell) \cos (\zeta(t_\ell) - \delta(t_\ell) \tag{A2}$$

All the terms are defined in Section 5.1.2. We will use a type A Gram-Charlier Series to model the pdf of y.

Gram-Charlier Series

Other authors have used the Gram-Charlier approach to attempt to determine the performance of modulation systems in impulsive noise when nonlinearities are being used [22,23]. Beach and George [23] used a severely truncated (three or four terms) series and their results do not match empirical results [21] and Shohara [22] uses an approach which requires that all the samples be independent and identically distributed. This is applicable for PSK modulation, but does not lend itself to CPMFSK demodulation. Shohara recognized this and indicated in an Appendix ways which the problem might be solved.

The derivation of the Gram-Charlier series is given in many references [8, 22, 23]. Thus, just an overview will be given here. If we define a new variable

$$z = \frac{y-\mu_1}{\sigma} \tag{A3}$$

where $\mu = E\{y\}$ and $\sigma^2 = \text{Var}\{y\}$, the pdf of z can be given as [8]

$$p(z) = \phi(z) + \sum_{\ell=3}^{\infty} b_\ell \phi(z) \; H_\ell(z) \tag{A4}$$

where

$$\phi(z) = \frac{1}{\sqrt{2\pi}} e^{-\frac{z^2}{2}} \tag{A5}$$

and $H_\ell(z)$ is the ℓ^{th} Hermite polynomial.

$H_\ell(z)$ can either be determined by a recursion formula [8]

$$H_\ell(z) = zH_{\ell-1}(z) - (\ell-1)H_{\ell-2}(z) \tag{A6}$$

where $H_o(z) = 1$
and
$H_1(z) = z$, or it can be shown that (A7)

$$H_\ell(z) = \sum_{k=o}^{\lfloor \frac{\ell}{2} \rfloor + 1} \frac{(-1)^k \, n!}{(n-2k)!k!2^k} \; z^{n-2k} \tag{A8}$$

where $\lfloor \frac{\ell}{2} \rfloor$ indicates the nearest integer less than or equal to $\frac{\ell}{2}$.

To determine the coefficients b_ℓ in Eq. A4, we can multiply both sides of A4 by $H_m(z)$ and integrate over the real line.

$$\int_{-\infty}^{\infty} H_m(z)p(z)dz = \int_{-\infty}^{\infty} \phi(z)H_m(z)dz + \sum_{\ell=3}^{\infty} b_\ell \int_{-\infty}^{\infty} \phi(z)H_\ell(z)H_m(z)dz \tag{A9}$$

As long as $m \neq l$, the first term on the r.h.s. of A9 is, from [27, Section 22], 0. Furthermore, the Hermite polynomials are biorthogonal so that

$$\frac{1}{\sqrt{2\pi}} \int_{-\infty}^{\infty} e^{-\frac{z^2}{2}} H_l(z) H_m(z) = m!\ \delta_{lm} \tag{A10}$$

Where δ_{lm} is the Kronecker delta,

$$\delta_{lm} = \begin{cases} 1, & l=m \\ 0, & l \neq m \end{cases} \tag{A11}$$

Combining A9 and A10 we get

$$\int_{-\infty}^{\infty} H_m(z) p(z) dz = b_m m! \quad \text{or} \tag{A12}$$

$$b_m = \frac{1}{m!} \int_{-\infty}^{\infty} H_m(z) p(z) dz \tag{A13}$$

Since $H_m(z)$ is a polynomial in z, knowledge of the moments of z will allow the determination of b_m, and hence from A4, p(z). From A3, we know that

$$z^m = \frac{1}{\sigma^m} \sum_{k=0}^{m} \binom{m}{k} y^{m-k} (-\mu_1)^k \tag{A14}$$

$$\text{So} \quad E\{z^m\} = \frac{1}{\sigma^m} \sum_{k=0}^{m} \binom{m}{k} (-\mu_1)^k E\{y^{m-k}\} \tag{A15}$$

Hence, if we can determine the moments of y, we can calculate the moments of z. The next section discusses techniques to determine the moments of y.

From Eq. A4, it is clear that a practical determination of p(z) will necessitate a truncation of the infinite series. No known techniques have been found for determining the truncation error, and this is a question still to be addressed.

Before concluding this section, it is recalled from Section 5.1.2 in the text that the desired calculation is to determine the probability that y exceeds zero. This implies, from Eq. A3, that we desire

$$\Pr\{z > \frac{-\mu_1}{\sigma}\} = \int_{\frac{-\mu_1}{\sigma}}^{\infty} p(z)dz \tag{A16}$$

This can be seen to be

$$\Pr\{z > \frac{-\mu_1}{\sigma}\} = \int_{\frac{-\mu_1}{\sigma}}^{\infty} \phi(z)dz + \sum_{\ell=3}^{\infty} b_\ell \int_{\frac{-\mu_1}{\sigma}}^{\infty} \phi(z)H_\ell(z)dz \tag{A17}$$

From [27],

$$\int_{\frac{-\mu_1}{\sigma}}^{\infty} \frac{1}{\sqrt{2\pi}} e^{\frac{-z^2}{2}} dz = \frac{1}{2} \operatorname{erfc}\left(\frac{-\mu_1}{\sqrt{2}\sigma}\right). \tag{A18}$$

From [8], we know that

$$\phi(z)H_\ell(z) = (-1)^\ell \phi^{[\ell]}(z) \tag{A19}$$

where $\phi^{[\ell]}(z)$ is the ℓ^{th} derivative of $\phi(z)$. Therefore,

$$\int (-1)^\ell \phi^{[\ell]}(z) = (-1)^\ell \phi^{[\ell-1]}(z) = (-1)^{2\ell-1} \phi(z)H_{\ell-1}(z), \tag{A20}$$

so $$\int_{\frac{-\mu_1}{\sigma}}^{\infty} \phi(z) H_\ell(z) dz = \frac{1}{\sqrt{2\pi}} H_{\ell-1}\left(\frac{-\mu_1}{\sigma}\right) e^{-\frac{\mu_1^2}{2\sigma^2}} \quad \text{(A21)}$$

Hence

$$\Pr\{z > \frac{-\mu_1}{\sigma}\} = \frac{1}{2} \operatorname{erfc}\left(\frac{-\mu_1}{\sqrt{2}\sigma}\right) + \sum_{\ell=3}^{\infty} b_\ell H_\ell\left(\frac{-\mu_1}{\sigma}\right) e^{\frac{-\mu_1^2}{2\sigma^2}} \quad \text{(A22)}$$

This implies that it is unnecessary to use the Gram Charlier series to determine the pdf of z, but it can be used directly to determine the probability that z exceeds a threshold.

Determination of Moments of y

From Eq. A1, it can be shown that (A23)

$$y^k = \sum_{m_o=0}^{k} \sum_{m_1=0}^{k} \cdots \sum_{m_L=0}^{k} \frac{k!}{m_o!\ m_1! \cdots m_L!} (a_o y_o)^{m_o} (a_1 y_1)^{m_1} \cdots (a_L y_L)^{m_L}$$

with the added condition that

$$\sum_{\ell=0}^{L} m_\ell = k \quad \text{(A24)}$$

Eq. A23, which is a multinomial expression can be thought of as an extension of the binomial theorem. From A23, the k^{th} moment of y is

$$E\{y^k\} = \sum_{m_0=0}^{k} \sum_{m_1=0}^{k} \cdots \sum_{m_L=0}^{k} \frac{k!}{m_0!\, m_1! \cdots m_L!} \cdot a_0^{m_0}\, a_1^{m_1} \cdots a_L^{m_L}\, E\{y_0^{m_0}\, y_1^{m_1} \cdots y_L^{m_L}\} \tag{A-25}$$

with the condition of Eq. A24. If knowledge is available or derivable about the joint statistics of the various time samples, then Eq. A25 can be used to determine the k^{th} moment of y. On the other hand, if each of the time samples is independent, then

$$E\{y_0^{m_0} y_1^{m_1} \cdots y_L^{m_L}\} = E\{y_0^{m_0}\}E\{y_1^{m_1}\} \cdots E\{y_L^{m_L}\} \tag{A26}$$

Eq. A26 can be used in Eq. A25 to again calculate the k^{th} moment of y, however in the case of independent sample, a recursive technique can be devised.

From A1

$$y^k = \left(\sum_{\ell=0}^{L} a_\ell y_\ell\right)^k = (a_0y_0 + a_1y_1 + \cdots + a_Ly_L)^k \tag{A27}$$

Using the binomial theorem this can be written as

$$\sum_{n_0=0}^{k} \binom{k}{n_0} (a_0y_0)^{k-n_0} (a_1y_1 + a_2y_2 + \cdots + a_Ly_L)^{n_0} \tag{A28}$$

Using the binomial theorem on the second term of A28 gives

(A29)

$$\sum_{n_0=0}^{k} \binom{k}{n_0} (a_0y_0)^{k-n_0} \sum_{n_1=0}^{n_0} \binom{n_0}{n_1} (a_1y_1)^{n_0-n_1} (a_2y_2 + \cdots + a_Ly_L)^{n_1}$$

and repeated application gives

$$y^k = \sum_{n_0=0}^{k} \binom{k}{n_0} (a_0 y_0)^{k-n_0} \sum_{n_1=0}^{n_0} \binom{n_0}{n_1} (a_1 y_1)^{n_0-n_1} \cdots$$

$$\cdots \sum_{n_{L-1}=0}^{n_{L-2}} \binom{n_{L-2}}{n_{L-1}} (a_{L-1} y_{L-1})^{n_{L-2}-n_{L-1}} (a_L y_L)^{n_{L-1}} \quad \text{(A30)}$$

From this, taking the expected value of both sides allows a recursive technique for calculating $E\{y^k\}$. Clearly either technique requires the determination of moments of the individual samples y_ℓ, thus the next section will address the determination of these momemts.

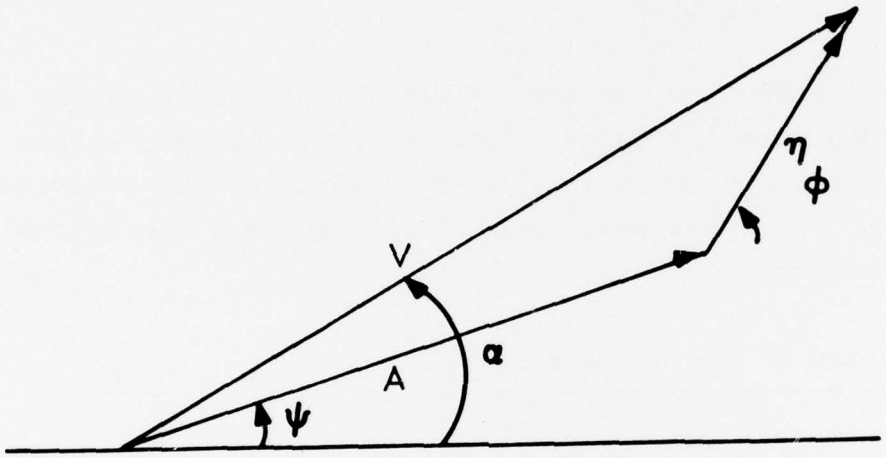
Determination of Moments of y_ℓ

From (A2),

$$y_\ell = \xi(t_\ell) \cos(\zeta(t_\ell) - \delta(t_\ell)) \quad \text{(A31)}$$

where from the text, $\xi(t_\ell)$ is the sampled signal plus noise envelope which has been processed by the nonlinearity, $\zeta(t_\ell)$ is the sampled signal plus noise phase, and $\delta(t_\ell)$ is the sampled filter phase. $\xi(t_\ell)$ and $\zeta(t_\ell)$ are random variables and $\delta(t_\ell)$ is deterministic.

Using the analytic noise models of Section 4, the joint pdf of $\xi(t_\ell)$ and $\zeta(t_\ell)$ can be derived as follows. We will temporarily drop the sampled representation. Consider figure A1, which shows a signal vector of magnitude A and phase ψ and an additive noise vector of magnitude η and phase ϕ. We are then interested in the resultant signl plus noise vector of magnitude v and phase α.



SIGNAL IS $\mathrm{Re}\left\{A_e\, i\psi_e\, jwt\right\}$

NOISE IS $\mathrm{Re}\left\{\eta_e\, i\phi_e\, jwt\right\}$

4403-77E

Figure A1. Envelope and Phase of Signal Plus Noise

It can be seen that

$$v = [(A \cos \psi + \eta \cos \phi)^2 + (A \sin \psi + \eta \sin \phi)^2]^{\frac{1}{2}} \qquad \text{(A-32)}$$

$$= [A^2 + \eta^2 + 2A\eta \cos (\phi - \psi)]^{\frac{1}{2}}$$

and

$$\alpha = \tan^{-1} \frac{A \sin\psi + \eta \sin \phi}{A \cos\psi + \eta \sin \phi} \qquad \text{(A-33)}$$

We know the joint pdf of η and ϕ , designated as $p_{H,\Phi}(\eta, \phi)$. To find the conditional joint pdf of v and α conditioned on A and ψ, we need the Jacobian of the transformations (A32) and (A33) [28]. With simple substitution, the Jacobian is η/v. As an example, consider the truncated Hall model with $\theta=3$. From section 4, the joint pdf of η and ϕ is

$$p_{H,\Phi}(\eta,\phi) = \begin{cases} \dfrac{b\,\gamma^2\eta}{\pi[\eta^2+\gamma^2]2} & , \quad 0 \leq \eta \leq E \\ 0 & , \quad \eta \geq E \end{cases} \qquad \text{(A-34)}$$

It follows that the conditional joint pdf of v and α is

$$p_{V,A}(v,\alpha|A,\psi) = \begin{cases} \dfrac{b\gamma^2 v\,[v^2 + A^2 - 2Av \cos (\alpha-\psi)]^{\frac{1}{2}}}{\pi[v^2 + A^2 - 2Av \cos (\alpha-\psi) + \gamma^2]^2} \\ \qquad , 0 \leq \eta \leq E \\ 0, \ \eta > E \end{cases} \qquad \text{(A-35)}$$

The signal plus noise sample passes through the zero-memory nonlinearity which is modeled in Section 2 by the transformation of variables.

$$\xi = \begin{cases} v, & v \leq t_h \\ k, & v > t_h \end{cases}$$

$$\zeta = \alpha \tag{A-36}$$

where k = 0 for a bandpass hole punch and $k=t_h$ for the bandpass clipper. Using (A-36), the joint conditional pdf of ξ, ζ is

$$p_{\Xi,z}(\xi,\zeta|A,\psi) = w_{t_h}(\xi)\, p_{v,A}(v,\alpha|A,\psi) + \delta(\xi-k) \int_{t_h}^{\infty} p_v(v|A,\psi)dv \cdot p_A(\zeta|A,\psi)dv \tag{A-37}$$

where $w_{t_h}(\xi)$ is a window function and $\delta(\xi-k)$ is the Direc-delta function correspondingly defined as

$$w_{t_h}(\xi) = \begin{cases} 1, & \xi \leq t_h \\ 0, & \xi > t_h \end{cases} \tag{A38}$$

and

$$\delta(\xi-k) = \begin{cases} 1, & \xi=k \\ 0, & \text{elsewhere} \end{cases} \tag{A-39}$$

$p_v(v|A,\psi)$ and $p_A(\zeta|A,\psi)$ are the conditional marginal densities for the envelope and phase respectively. Eq. A-37 can be understood by recognizing the first term as that part of the input pdf which is unaffected by the nonlinearity (input envelope is less than

the threshold), whereas the second term is the part which is affected by the nonlinearity.

It is important to note that the joint conditional pdf of ξ and ζ as shown in Eq. A-37 is non-zero on a finite range, i.e. for $\xi \leq t_h$. This will greatly facilitate any numerical techniques which must be used in further processing.

Now we make one further change of variables

$$\begin{aligned} y &= \xi \cos(\zeta-\delta) \\ x &= \xi \sin(\zeta-\delta), \end{aligned} \tag{A-40}$$

the joint conditional pdf of x and y is $p_{X,Y}(x,y|A,\psi)$

(A-41)

$$p_{X,Y}(x,y|A,\psi) = \frac{1}{\sqrt{x^2+y^2}} p_{\Xi,Z}(\sqrt{x^2+y^2},\ \tan^{-1}(\frac{x}{y})+\delta|A,\psi)$$

from which the marginal density of y is

$$p_Y(y|A,\psi) = \int_{-\sqrt{t_h^2-y^2}}^{\sqrt{t_h^2-y^2}} p_{X,Y}(x,y|A,\psi)dx \tag{A-42}$$

The m^{th} conditional moment of y is then

$$E\{y^m|A,\psi\} = \int_{-t_h}^{t_h} y^m\, p_Y(y|A,\psi)\, dy \tag{A-43}$$

In all the foregoing, we have suppressed the sampled representation. None of the noise models known to the author allow analytic determination of all the above equations. It is interesting to

note that even Gaussian noise, for which the input pdf of the envelope is a Rician, does not allow full analytic solution to all the above equations. Hence, numerical approaches must be used in the above integrations. This in turn requires a study of the resolution required for the numerical integrations. Time constraints precluded this study and the ensuing numerical determinations of the moments of individual samples.

APPENDIX B

Statistical Relationships for Hall and Truncated Hall Models

This appendix contains the derivations of the expressions presented in Table 5.

Envelope PDF for Truncated Hall Distributions; $\theta = 2, 3$

The envelope pdf for the truncated Hall distributions ($\theta = 2, 3$) are defined to be

$$p_E(\eta) = \frac{b(\theta-1)\gamma^{\theta-1}\eta}{(\eta^2+\gamma^2)^{(\theta+1)/2}} \qquad 0 \le \eta \le E$$

$$= 0 \qquad \eta > E \tag{B-1}$$

where b is chosen so that

$$\int_0^E p_E(\eta)d\eta = 1 \tag{B-2}$$

Using the transformation $\eta = \gamma\tan z$, $0 \le z \le \tan^{-1}(E/\gamma)$ in Equation (A-2) leads to

$$b = \frac{D^{\theta-1}}{D^{\theta-1}-1} \tag{B-3}$$

where $D = \sqrt{1+(E/\gamma)^2}$

Thus, for $\theta = 2$, the envelope pdf is given by

$$P_E(\eta) = \frac{D\gamma}{D-1} \frac{\eta}{(\eta^2+\gamma^2)^{3/2}} \quad , \quad 0 \leq \eta \leq \gamma\sqrt{D^2-1}$$

$$= 0 \quad , \quad \eta > \gamma\sqrt{D^2-1} \qquad \text{(B-4)}$$

and, for $\theta = 3$,

$$P_E(\eta) = \frac{D^2}{D^2-1} \frac{2\gamma^2\eta}{(\eta^2+\gamma^2)^2} \quad , \quad 0 \leq \eta \leq \gamma\sqrt{D^2-1}$$

$$\text{(B-5)}$$

$$= 0 \quad , \quad \eta > \gamma\sqrt{D^2-1}$$

Moments of Envelope pdf

The moments of the envelope are defined by

$$\mu_j = \int_0^\infty \eta^j \, p(\eta) d\eta$$

$$\text{(B-6)}$$

$$= \int_0^\infty \frac{(\theta-1)\,\gamma^{\theta-1}\eta^{j+1}}{(\eta^2+\gamma^2)^{\frac{\theta+1}{2}}} d\eta \qquad \theta = 4, 5$$

and

$$= \frac{D^{\theta-1}}{D^{\theta-1}-1} \int_0^E \frac{(\theta-1)\gamma^{\theta-1}\eta^{j+1}}{(\eta^2+\gamma^2)^{\frac{\theta+1}{2}}}\, d\eta \qquad \theta = 2,\ 3 \qquad \text{(B-7)}$$

The transformation used to obtain (B-3) above yields expressions for the convergent moments*.

Thus integrals of the form

$$\int \frac{\eta^{j+1}}{(\eta^2+\gamma^2)^{\frac{\theta+1}{2}}}\, d\eta = \frac{1}{\gamma^{\theta-j-1}} \int \frac{\tan^{j+1} z \sec^2 z}{\sec^{\theta+1} z}\, dz \qquad \text{(B-8)}$$

$$= \frac{1}{\gamma^{\theta-j-1}} \int \sin^{j+1} z \cos^{\theta-j-2} z\, dz$$

can be evaluated for specific values of j and θ, using the appropriate limits of integration. Substitution of $D = \sqrt{1+E^2/\gamma^2}$ in the case of truncated distributions results in the expressions given in Table 5. For example, the mean of the envelope pdf for $\theta = 2$ is given by

$$\mu_1 = \frac{D}{D-1}\,\gamma \int_0^E \frac{\eta^2}{(\eta^2+\gamma^2)^{\frac{3}{2}}}\, d\eta = \frac{D\gamma}{(D-1)} \int_0^E \frac{\sin^2 z}{\cos z}\, dz$$

$$= \frac{D}{D-1}\,\gamma \left\{ \log\left(D + \sqrt{D^2-1}\right) - \frac{\sqrt{D^2-1}}{D} \right\}$$

---

*For $\theta = 4$, moments μ_1, μ_2 converge; for $\theta = 5$, μ_j, $j = 1, 2, 3$ converge; all moments of the truncated distributions exist.

Amplitude Probability Distributions: APD

The amplitude probability distribution provides the probability of the variable exceeding a level R, i.e.,

$$\Pr\{\eta>R\} = \int_R^\infty p(\eta)d\eta \tag{B-10}$$

For the Hall distributions with $\theta = 4, 5$

$$\Pr\{\eta>R\} = (\theta-1)\gamma^{\theta-1}\int_R^\infty \frac{\eta d\eta}{(\eta^2+\gamma^2)^{\frac{\theta+1}{2}}} \tag{B-11}$$

and for $\theta = 2, 3$

$$\Pr\{\eta>R\} = \frac{D^{\theta-1}}{D-1}\ (\theta-1)\gamma^{\theta-1}\int_R^E \frac{\eta d\eta}{(\eta^2+\gamma^2)^{\frac{\theta+1}{2}}} \tag{B-12}$$

Using the substitution $z = \eta^2+\gamma^2$,

(B-13)

$$(\theta-1)\int \frac{\eta d\eta}{(\eta^2+\gamma^2)^{\frac{\theta+1}{2}}} = (\theta-1)\int \frac{dz}{2z^{\frac{\theta+1}{2}}} = \frac{-1}{z^{\frac{\theta-1}{2}}} = \frac{-1}{(\eta^2+\gamma^2)^{\frac{\theta-1}{2}}}$$

Therefore the Hall distributions have the following APD's:

For $\theta = 2$

$$\Pr\{\eta>R\} = \frac{D}{D-1}\,\gamma\left[-\frac{1}{(E^2+\gamma^2)^{\frac{1}{2}}}+\frac{1}{(R^2+\gamma^2)^{\frac{1}{2}}}\right]$$

$$= \frac{D}{D-1}\left[\frac{1}{\left(1+\frac{R^2}{\gamma^2}\right)^{\frac{1}{2}}}-\frac{1}{D}\right] \qquad \text{(B-14)}$$

For $\theta = 3$

$$\Pr\{\eta>R\} = \frac{D^2}{D^2-1}\,\gamma^2\left[\frac{-1}{(E^2+\gamma^2)}+\frac{1}{(R^2+\gamma^2)}\right] \qquad \text{(B-15)}$$

$$= \frac{D^2}{D^2-1}\left[\frac{-1}{\left(1+\frac{R^2}{\gamma^2}\right)}-\frac{1}{D^2}\right]$$

For $\theta = 4$

$$\Pr\{\eta>R\} = \frac{\gamma^3}{(R^2+\gamma^2)^{\frac{3}{2}}} = \frac{1}{\left(1+\frac{R^2}{\gamma^2}\right)^{\frac{3}{2}}} \qquad \text{(B-16)}$$

For $\theta = 5$

$$\Pr\{\eta>R\} = \frac{\gamma^4}{(R^2+\gamma^2)^2} = \frac{1}{\left(1+\frac{R^2}{\gamma^2}\right)^2} \tag{B-17}$$

Marginal Density of Quadrature Components

The amplitudes of the quadrature voltage components are related to their envelope v by the transformation

$$\begin{aligned} \eta_c &= \eta \cos\phi \\ \eta_s &= \eta \sin\phi \end{aligned} \tag{B-18}$$

where ϕ is assumed to be uniformly distributed and independent of η.

Therefore, for $\theta = 4$ and 5 where

$$P(\eta) = \frac{(\theta-1)\gamma^{\theta-1}}{(\eta^2+\gamma^2)^{(\theta+1)/2}}\eta \qquad 0 \le \eta \le \infty \tag{B-19}$$

the transformation (A-18) gives

$$P(\eta_c) = \int_{-\infty}^{\infty} \frac{(\theta-1)\gamma^{\theta-1}}{2\pi} \frac{d\eta_s}{(\eta_c^2+\eta_s^2+\gamma^2)^{\frac{\theta+1}{2}}} \tag{B-20}$$

The quadrature components η_c and η_s are identically distributed and $p(\eta_s) = p(\eta_c)$.

Letting $a^2 = \eta_c^2+\gamma^2$ in (B-20) and making the substitution $\eta_s = a \tan z$, yeilds integrals of the form

$$\int \frac{d\eta_s}{(\eta_s^2+a^2)^{\frac{\theta+1}{2}}} = \frac{1}{a^\theta} \int \cos^{\theta-1} z \, dz \qquad \text{(B-21)}$$

for which recursion formulas exist. For $\theta = 5$

$$p(\eta_c) = \frac{3\gamma^4}{4(\eta_c^2+\gamma^2)^{5/2}} \qquad -\infty < \eta_c < \infty \qquad \text{(B-22)}$$

For $\theta = 4$

$$p(\eta_c) = \frac{2\gamma^3}{(\eta_c^2+\gamma^2)^2} \qquad \text{(B-23)}$$

For $\theta = 2$ and 3, the marginal density is obtained by substituting (B-18) in equation (B-1) and integrating with respect to η_s over the region defined by $\eta_c^2 + \eta_s^2 \leq E^2$. Thus

$$p(\eta_c) = \frac{D^{\theta-1}}{D^{\theta-1}_{-1}} \frac{(\theta-1)}{2\pi} \int_{-\sqrt{E^2-\eta_c^2}}^{\sqrt{E^2-\eta_c^2}} \frac{\gamma \, d\eta_s}{(\eta_c^2+\eta_s^2+\gamma^2)^{\frac{\theta+1}{2}}} \quad |\eta_c| \leq E \qquad \text{(B-24)}$$

For $\theta = 3$

$$p(\eta_c) = \frac{D^2}{(D^2-1)} \cdot \frac{\gamma^2}{(\eta_c^2+\gamma^2)^{3/2}\pi} \left\{ \tan^{-1} \sqrt{\frac{E^2-\eta_c^2}{\eta_c^2+\gamma^2}} - \frac{\sqrt{E^2-\eta_c^2}\cdot\sqrt{\eta_c^2+\gamma^2}}{E^2+\gamma^2} \right\},$$

$$|\eta_c| \leq E \qquad (B\text{-}25)$$

$$= 0, \quad |\eta_c| > E$$

For $\theta = 2$

$$p(\eta_c) = \frac{1}{(D-1)\pi} \frac{\sqrt{\gamma^2 D^2 - (\eta_c^2+\gamma^2)}}{(\eta_c^2+\gamma^2)} \qquad |\eta_c| \leq \gamma\sqrt{D^2-1}$$

$$= 0 \qquad |\eta_c| > \gamma\sqrt{D^2-1} \qquad (B\text{-}26)$$

Appendix C

Statistical Relationships for the Generalized Laplace Variable

The probability that the generalized Laplace variable, s exceeds the threshold, R, is given by

$$\Pr\{s>R\} = \int_R^\infty p(s)\, ds \tag{C-1}$$

$$= 1 - \int_0^R \frac{s^r K_{1-r}\left(\frac{s}{k\sigma}\right)}{(k\sigma)^{r+1}\,\Gamma(r)\,2^{r-1}}\, ds \tag{C-2}$$

Using Item 6.561-12 in [17] to evaluate the above equation yields

$$\Pr\{s>R\} = \left(\frac{R}{k\sigma}\right)^r \frac{1}{\Gamma(r)\,2^{r-1}}\, K_{-r}\left(\frac{R}{k\sigma}\right) \tag{C-3}$$

Since $K_{-r}\left(\frac{R}{k\sigma}\right) = K_r\left(\frac{R}{k\sigma}\right)$, equation (45) follows.

If s denotes the envelope of the quadrature components x and y, the pdf of x (or y) can be found using the transformations

$$x = s\cos\phi$$

and $$y = s\sin\phi \tag{C-4}$$

where ϕ is a uniformly distributed random variable in the interval $(0, 2\pi)$.

The pdf of x can then be found from

$$p(x) = \int_{-\infty}^{\infty} p(x,y)\, dy \qquad \text{(C-5)}$$

$$= \int_{-\infty}^{\infty} \frac{1}{2\pi} \frac{(\sqrt{x^2+y^2})^{r-1}}{(k\sigma)^{r+1}\,\Gamma(r)\,2^{r-1}} K_{1-r}\left(\frac{\sqrt{x^2+y^2}}{k\sigma}\right) dy$$

Noting that $p(-x) = p(x)$ and using item 6.596-3 in [17] yields

$$p(x) = \frac{|x|^{r-\frac{1}{2}}}{(k\sigma)^{r+\frac{1}{2}}\,\pi\Gamma(r)\,2^{r-\frac{1}{2}}} K_{\frac{1}{2}-r}\left(\frac{|x|}{k\sigma}\right)$$

Appendix D

Transformations for Probability Graph Paper

The transformation of the abscissa values for the probability graph paper as used here disagrees somewhat with the transformations used by Crichlow and Wilson. The point of disagreement is the value of the constant multiplying the right hand side of the equation. In order to clarify any problems, here is the derivation of the abscissa transformation, when the ordinate transformation is known:

$$y' = 20 \log_{10} y \tag{D1}$$

when the abscissa transformation is assumed to be of the general format:

$$x' = C \log_{10} (-\ln x) \tag{D2}$$

and assuming that the Rayleigh function plots as a straight line of slope -0.5. The Rayleigh pdf is

$$p(z)dz = \frac{z}{\sigma^2} \exp\left(-\frac{z^2}{2\sigma^2}\right) dz \tag{D3}$$

Since the rms value of z is $\sqrt{2}\,\sigma$, let $x = \frac{z}{\sqrt{2}\,\sigma}$, (D4)

resulting in $p(x)dx = 2x \exp(-x^2)dx$ (D5)

The APD of R is $APD(R) = \int_R^\infty p(x)dx$

$$= \exp(-R^2) \tag{D6}$$

The slope of the Rayleigh line is -0.5

$$\frac{y'}{x'} = -0.5 = \frac{20 \log R}{C \log(-\ln(APD(R)))} \tag{D7}$$

$$= \frac{20 \log R}{2C \log R}$$

From this we can see that

$$C = -20 \tag{D8}$$

and Eq. 55 in the text follows.

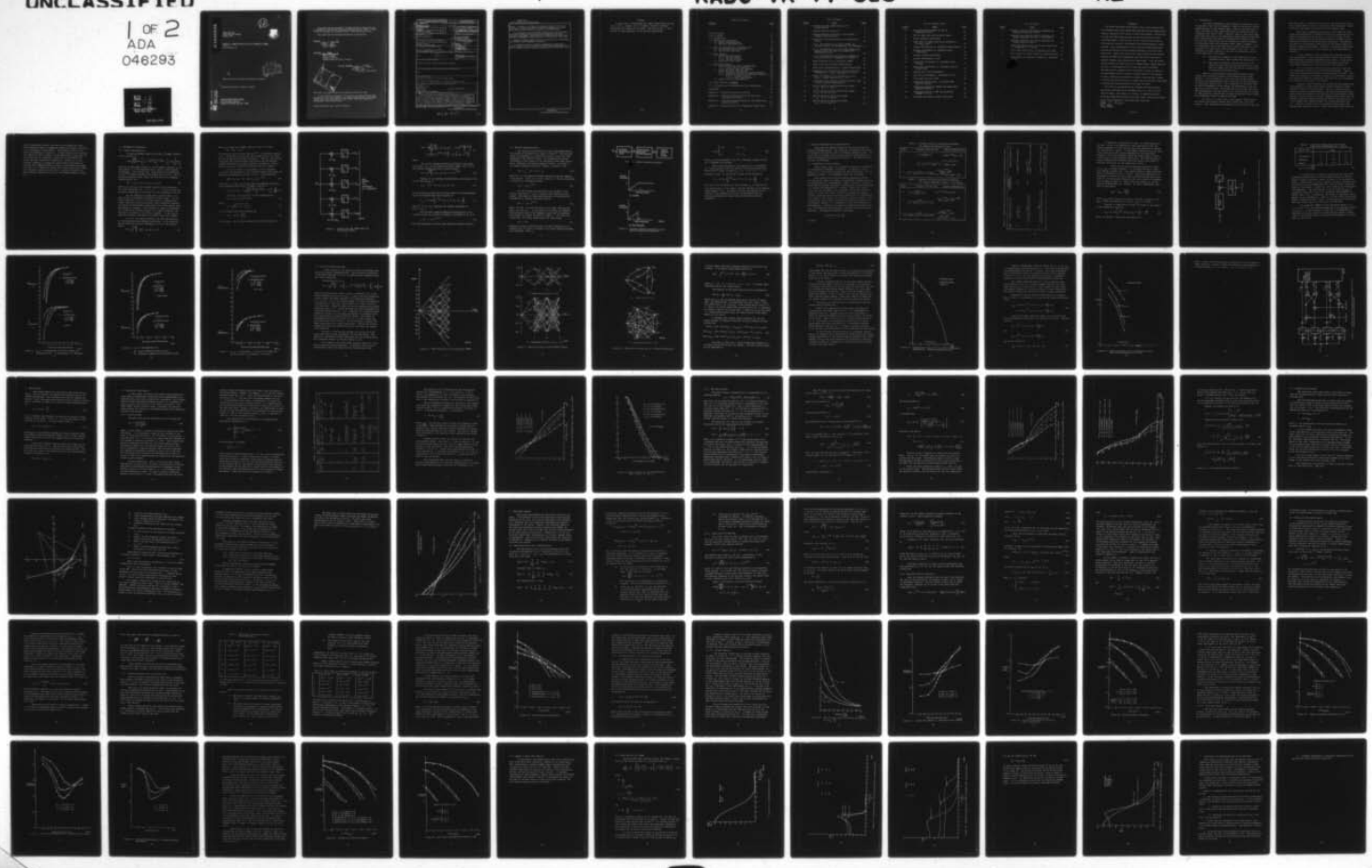
MISSION
of
Rome Air Development Center

RADC plans and conducts research, exploratory and advanced development programs in command, control, and communications (C^3) activities, and in the C^3 areas of information sciences and intelligence. The principal technical mission areas are communications, electromagnetic guidance and control, surveillance of ground and aerospace objects, intelligence data collection and handling, information system technology, ionospheric propagation, solid state sciences, microwave physics and electronic reliability, maintainability and compatibility.



AD-A046 293 GTE SYLVANIA INC NEEDHAM HEIGHTS MASS ELECTRONIC SYS--ETC F/G 9/3
CPMFSK AS A MODULATION ON THE VLF-HF ATMOSPHERIC CHANNEL.(U)
OCT 77 T A SCHONHOFF F30602-76-C-0410
UNCLASSIFIED RADC-TR-77-318 NL

1 OF 2
ADA
046293



AD A046293

RADC-TR-77-318
Final Technical Report
October 1977

CPMFSK AS A MODULATION ON THE VLF-HF ATMOSPHERIC CHANNEL

GTE Sylvania, Inc.

DDC
RECEIVED
NOV 7 1977
F

Approved for public release; distribution unlimited.

Laboratory Directors' Fund No. 01717608

DDC FILE COPY

ROME AIR DEVELOPMENT CENTER
Air Force Systems Command
Griffiss Air Force Base, New York 13441

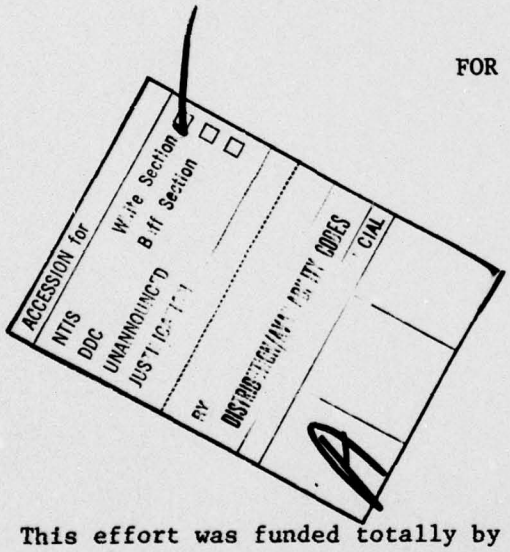
This report has been reviewed by the RADC Information Office (OI) and is releasable to the National Technical Information Service (NTIS). At NTIS it will be releasable to the general public, including foreign nations.

This report has been reviewed and approved for publication.

APPROVED: John T. Gamble
JOHN T. GAMBLE
Project Engineer

APPROVED: Fred I. Diamond
FRED I. DIAMOND
Technical Director
Communications and Control Division

FOR THE COMMANDER: John P. Huss
JOHN P. HUSS
Acting Chief, Plans Office



This effort was funded totally by the Laboratory Directors' Fund.

If your address has changed or if you wish to be removed from the RADC mailing list, or if the addressee is no longer employed by your organization, please notify RADC (DCCL) Griffiss AFB NY 13441. This will assist us in maintaining a current mailing list.

Do not return this copy. Retain or destroy.

SECURITY CLASSIFICATION OF THIS PAGE *(When Data Entered)*

REPORT DOCUMENTATION PAGE

READ INSTRUCTIONS BEFORE COMPLETING FORM

1. REPORT NUMBER: RADC-TR-77-318	2. GOVT ACCESSION NO.
3. RECIPIENT'S CATALOG NUMBER	
4. TITLE *(and Subtitle)*: CPMFSK AS A MODULATION ON THE VLF-HF ATMOSPHERIC CHANNEL.	5. TYPE OF REPORT & PERIOD COVERED: Final Technical Report. 16 August 1976 - 31 May 1977
6. PERFORMING ORG. REPORT NUMBER: N/A	
7. AUTHOR(s): Thomas A. Schonhoff	8. CONTRACT OR GRANT NUMBER(s): F3602-76-C-0410
9. PERFORMING ORGANIZATION NAME AND ADDRESS: GTE Sylvania - Electronic Systems Group, Eastern Division, Needham Heights MA 02194	10. PROGRAM ELEMENT, PROJECT, TASK AREA & WORK UNIT NUMBERS: 61101F, 01717608
11. CONTROLLING OFFICE NAME AND ADDRESS: Rome Air Development Center (DCCL), Griffiss AFB NY 13441	12. REPORT DATE: October 1977
	13. NUMBER OF PAGES: 112
14. MONITORING AGENCY NAME & ADDRESS *(if different from Controlling Office)*: Same	15. SECURITY CLASS. *(of this report)*: UNCLASSIFIED
	15a. DECLASSIFICATION/DOWNGRADING SCHEDULE: N/A

16. DISTRIBUTION STATEMENT *(of this Report)*

Approved for public release; distribution unlimited.

17. DISTRIBUTION STATEMENT *(of the abstract entered in Block 20, if different from Report)*

Same

18. SUPPLEMENTARY NOTES

RADC Project Engineer: Dr. John T. Gamble (DCCL)

This effort was funded totally by the Laboratory Directors' Fund.

19. KEY WORDS *(Continue on reverse side if necessary and identify by block number)*

Modulation
Atmospheric Noise
Error Rates
Impulse Noise
Non-Linear Receiver Analysis

20. ABSTRACT *(Continue on reverse side if necessary and identify by block number)*

Continuous phase multi-frequency shift keying (CPMFSK) is investigated as a potential modulation on the VLF-HF additive atmospheric noise channel. The effects of pre-detection filtering and general concerns of receiver design are addressed. Monte Carlo simulation is used to evaluate the error rate performance of CPMFSK in terms of E_B/σ^2 where E_B is the energy per bit and σ^2 is the received atmospheric noise variance. The error rate performance is determined for linear receivers as well as non-linear receivers consisting of linear receivers preceded by a zero-memory nonlinearity, such as a clipper or a hole

DD FORM 1 JAN 73 1473 EDITION OF 1 NOV 65 IS OBSOLETE

UNCLASSIFIED

SECURITY CLASSIFICATION OF THIS PAGE *(When Data Entered)*

406 451

puncher. In addition to the Monte Carlo simulation approach to error rate performance, a theoretical approach to analytically estimate error rate was begun, and the present status of this approach is documented herein.

In the attempt to derive theoretical estimates of error-rate performance, it was found necessary to derive and evaluate mathematically tractable atmospheric noise models. These models are constrained to match some of the empirically determined first-order statistics of the atmospheric channel ~~(6)~~.

Finally, transmitted signal power spectral densities (p.s.d.) are derived and displayed for the modulations of interest.

It is found that the use of CPMFSK as a modulation on channels with additive atmospheric noise requires less E_B/σ^2 to achieve a given error rate than is necessary using more conventional modulations such as PSK, MSK, or CFSK.

Preface

I would like to acknowledge the useful suggestions and support of Dr. J. Gamble, Dr. A. Giordano, and Ms. Z. Huntoon throughout the course of this study. The work of Ms. Y. Perlmutter in noise modeling is also greatly appreciated.

Table of Contents

Section			Page
List of Figures			iv
List of Tables			vi
1.0	Introduction		1
2.0	Mathematical Background		4
	2.1	Signal Representations	4
	2.2	Receiver Representations	8
3.0	Receiver Implementation Considerations		11
	3.1	Predetection Filter Effects	11
	3.2	Use of MLSE Algorithm	20
4.0	Noise Models		31
	4.1	Analytical Noise Models	32
		4.1.1 The Hall Model	32
		4.1.2 The Mixture Model	38
	4.2	Simulation Noise Model	44
5.0	Error-Rate Results		50
	5.1	Theoretical Error Rate Considerations	50
		5.1.1 Linear Receiver Approach	52
		5.1.2 Nonlinear Receiver Approach	54
	5.2	Simulation Error Rate Results	58
		5.2.1 Simulation Results for Linear Receivers	60
		5.2.2 Simulation Results for Nonlinear Receivers	65
		5.2.2.1 Clipper Results	66
		5.2.2.2 Hole Punch Results	71
	5.3	Summary of Error Rate Results	78
6.0	Power Spectra for CPMFSK		79
7.0	Conclusions and Recommendations for Further Work		85
References			87
Appendix A - Selected Theoretical Results			89
Appendix B - Statistical Relationships for Hall and Truncated Hall Models			101
Appendix C - Statistical Relationships for the Generalized Laplace Variable			109
Appendix D - Transformations for Probability Graph Paper			111

List of Figures

Figure	Title	Page
1	Optimum High SNR CPMFSK Receiver for Gaussian Noise	6
2	General Receiver Structure	9
3	Envelope Transfer Functions of Zero-Memory Bandpass Nonlinearities	9
4	Technique to Determine Effect of Predetection Filter	15
5	C_d vs. 3dB Bandwidth for Binary CPMFSK and Various Filters: (a) Butterworth; (b) Chebyshev	17
6	C_d vs. 3dB Bandwidth for (a) Binary CPMFSK with Bessel Filter (b) Quaternary CPMFSK with Butterworth Filter	18
7	C_d vs. 3dB Bandwidth for Quaternary CPMFSK and Various Filters (a) Chebyshev; (b) Bessel	19
8	Phase Trajectories for Quaternary CPMFSK	21
9	Phase Trellises for Some CPMFSK Signals	22
10	Phase State Representation of Phase Trajectories	23
11	Probability of Bit Error for Viterbi Algorithm Demodulation - Binary Signaling (h = 2/3)	26
12	Effect of Change in D on Probability of Bit Error - Binary Modulation (h = 2/3)	28
13	Functional Block Diagram of Binary Receiver with Viterbi Algorithm Demodulation	30
14	APD for Empirical and Truncated Hall Model (V_d = 2, 4, 6, and 8)	36
15	APD for Empirical and Truncated Hall Model (V_d = 10, 12, and 14)	37
16	APD for Empirical and Mixture Model (V_d = 2, 4, 6, and 8)	41
17	APD for Empirical and Mixture Model (V_d = 10, 12, and 14)	42

List of Figures (Cont.)

Figure	Title	Page
18	Crichlow Graphical Model of APD of Atmospheric Noise	45
19	APD for Empirical and Simulation Model	49
20	Linear Receiver Performance	64
21	Mean Value of Signal Plus Noise Envelope vs. 10 $\log_{10}$ (E_B/σ^2)	67
22	Clipper Performance vs. Threshold Level (Binary)	68
23	Clipper Performance vs. Threshold Level (Quaternary)	69
24	Optimum Clipper Performance	70
25	Clipper Performance @ 0 dB	72
26	Hole Punch Performance vs. Threshold Level (Binary)	73
27	Hole Punch Performance vs. Threshold Setting (Quaternary)	74
28	Optimum Hole Punch Performance	76
29	Hole Punch Performance - Threshold @ 0 dB	77
30	One-Sided Spectrum of MSK	80
31	Normalized Binary CPFSK - One Sided Power Spectral Density	81
32	Normalized Quaternary CPMFSK One-Sided Power Spectral Density	82
33	Normalized Spectra of MSK and Quaternary CPMFSK (h = 0.4)	84
A1	Envelope and Phase of Signal Plus Noise	96

List of Tables

Table	Title	Page
1	Transfer Functions and Impulse Responses for Lowpass Butterworth Filters	12
2	Transfer Functions and Impulse Responses for Lowpass Chebyshev Filters (.1 dB Ripple)	12
3	Transfer Functions and Impulse Responses for Lowpass Bessel Filters	13
4	Group Path Delays (sec) for Filters Normalized to Bandwidth of 1 rad/sec	16
5	First Order Statistics of Truncated Hall Model	34
6	Error Rates for Binary CPFSK vs. Deviation Ratio	61
7	Error Rates for Quaternary CPMFSK vs. Deviation Ratio	62

EVALUATION

This effort investigated the quantitative value of using Constant Phase Multi-Frequency Shift Keying (CPMFSK) modulation and multi-baud demodulation in impulsive, Non-Gaussian noise typical of sub-HF radio channels. Previous work has shown that CPMFSK modem techniques are much more efficient than more conventional modems in Gaussian noise, and also, that non-linear impulsive noise reduction increases in effectiveness as the detection-element's length increases. Thus, the combination of noise reduction and CPMFSK multi-baud detection was expected to provide enhanced performance in real-world atmospheric noise. However, the results of this study indicate that the relative advantage of CPMFSK multi-baud-detection (over MSK) and non-linear noise reduction diminishes with increasing noise impulsiveness. Thus, the attractiveness of CPMFSK for impulsive VLF-HF is somewhat reduced. Another aspect of this work, an investigation of noise clipping and blanking thresholds, reaffirmed previous assumptions that a hard-limiter was equal or superior to any other bandpass clipper or blanker in reducing impulsive noise; however, an equally interesting, and potentially valuable, finding was that a blanker is significantly more effective than a clipper when the threshold is constrained to be higher than the mean envelope of the signal plus noise.

This effort has provided definitive, although lower than originally conjectured, performance results for CPMFSK signals in a realistic sub-HF radio environment. Nevertheless, the findings, in predetection receiver structures, demodulation efficiency, and signal spectra, definitely contribute to the state of knowledge in radio communication technology.

John T. Gamble

JOHN T. GAMBLE
Project Engineer

1. Introduction

The VLF-HF Atmospheric Noise Channel is characterized by an impulsive like noise environment. Much of the present digital communications on this channel employ constant envelope modulations, and most of these modulations can be considered forms of Frequency Shift Keying (FSK). Specific types of FSK modulations which have been used on the Atmospheric Noise Channel are Minimum Shift Keying (MSK) and Coherent Frequency Shift Keying (CFSK). Both of these modulations can be described as specific examples of Continuous Phase Multi-Frequency Shift Keying (CPMFSK), i.e., the modulation uses an FSK type signal wherein the phase is constrained to be continuous from one symbol to the next. This constraint of phase continuity can have two beneficial results on the qualities of the signal:

(1) The spectral occupancy of the signal can be considerably smaller than traditional modulations [1].

(2) The signal has memory, and utilization of this memory by observing the received waveform for more than one symbol interval can result in significantly improved performance [2-4].

Most of the performance improvements determined previously have assumed an additive white Gaussian noise (WGN) channel. It is interesting to note that for the WGN channel, the error-rate performance of MSK is the same as the performance of Phase Shift Keying (PSK). Yet, reference [5] indicates that on the VLF Atmospheric Noise Channel the performance of MSK is superior to that of PSK. This seems to be due to the fact that MSK demodulation uses essentially 2-bit time intervals of signal to make decisions, whereas PSK (and most traditional modulations) use independent symbol-to-symbol decisions.

In [2-4] it is shown that a more general CPMFSK signal can achieve performance results which exceed MSK in the WGN channel. This improvement performance is due largely to the fact

that more memory is imposed on the signal, and observation intervals of many symbols ($n \geq 3$) are utilized to make decisions. These facts were the primary motivations for the present study.

This report documents the result of this study to investigate the performance of CPMFSK when used as a modulation on the additive Atmospheric Noise Channel. It was the intent of the study to determine the error-rate performance of CPMFSK by both theoretical estimation and Monte-Carlo simulation. Furthermore, the effect of pre-detection filtering and the general concern of receiver design was addressed. Finally, transmitted signal power spectral densities (p.s.d.) were derived for the modulations of interest.

In the attempt to derive theoretical estimates of error-rate performance, it was found necessary to derive and evaluate mathematically tractable Atmospheric Noise models. These models were constrained to match some of the empirically determined first-order statistics of the Atmospheric Noise Channel [6].

All of the goals of the study were achieved except for the theoretical estimation of error-rate performance. However, error-rate performance by means of simulation was obtained. This report will document the present status of the theoretical effort, but time and budgetary constraints precluded the full development and results of this phase of the study.

Section 2 below outlines the mathematical development and the definition of terms which should greatly augment an understanding of the rest of the report. Section 3 considers more realistic receiver implementations, with specific emphasis being given toward the effects of various types of predetection filters. Section 3 also considers a receiver implementation based upon the Maximum Likelihood Sequence Estimation (MLSE) algorithm, or as it is perhaps more commonly known, the Viterbi Algorithm (VA) [7]. Section 4 present the noise modeling results which were accomplished during the study. Three noise models were used, two

for the theoretical effort, and one for the simulation effort. These models are shown to adequately match first-order statistics of the Atmospheric Noise Channel. The primary results of the study are presented in Section 5. A brief review of the theoretical effort is given, however, as mentioned above, this phase of the effort was not completed, so the bulk of the theoretical effort has been relegated to Appendix A. Section 5, in turn, consists primarily of simulation results which nonetheless do indicate that CPMFSK modulation yields a performance improvement over MSK, i.e., CPMFSK can achieve error rates equivalent to MSK with a smaller signal-to-noise ratio. Section 6 presents the power spectral densities (p.s.d.) of the CPMFSK signals of interest.

2. Mathematical Background

2.1 Signal Representation

A received CPMFSK signal during the i^{th} symbol interval can be written as

$$r(t)=\sqrt{\frac{2E_s}{T_s}}\ \cos\left[\omega_c t+\frac{d_i \pi h(t-(i-1)T_s)}{T_s}+\sum_{j=1}^{i-1}\pi h d_j\right]+n(t) \quad (1)$$

where E_s is the symbol energy, T_s is the symbol interval, ω_c is the carrier, h is the deviation ratio, and d_i is the digital information. The term $\sum_{j=1}^{i-1}\pi h d_j$ is the phase at the beginning of the i^{th} interval which can be assumed zero for i=1. n(t) is additive impulsive noise, which can be written in a bandpass representation [8].

$$n(t) = n_c(t)\ \cos\ \omega_c t - n_s(t)\ \sin\ \omega_c t \quad (2)$$

where $n_c(t)$ and $n_s(t)$ are lowpass impulsive noise processes. For M-ary modulation, $d_i = \pm 1, \pm 3, \ldots, \pm (M-1)$ and any two adjacent frequencies in the signal set are separated by h/T Hz.

For the commonly used MSK, h=0.5 and for CFSK, h=1.0. This results in orthogonal signaling for both cases. If h is chosen other than 0.5 or 1.0 and the signal is observed for n symbol intervals, better performance than orthogonal signaling can result and performance improvements over traditionally used modulations is possible. The procedure to improve performance is to observe the received signal for n symbol intervals, and then make a decision on one of the n symbols. In the case of coherent detection, the decision is made on the first symbol.

In [2-4], the optimum receiver for high SNR detection in a Gaussian noise environment was derived. It is useful to use the shorthand notation developed in [2] for the received signal.

$$r(t) = \sqrt{\frac{2E_s}{T_s}}\ \mathcal{A}(t, d_1, D_k) + n(t) \quad (3)$$

where d_1 is the first symbol, and D_k is the (n-1) tuple

$$D_k = \{d_2, \ldots, d_n\}.$$

The vector D_k can of course take on $M^{n-1} = m$ different possibilities. With these definitions, the optimum receiver for high SNR can be depicted as shown in Figure 1. That is, the receiver correlates the received signal with each of the M^n possible n-symbol waveforms that could have been transmitted. After n symbol intervals, a decision is made on the first symbol.

It will be useful in the sequel to use a baseband equivalent representation of the received signal rather than the bandpass representations of Eqs. 1 and 3. Correspondingly

$$\mathcal{S}(t, d_1, D_k) = \mathrm{Re}\{s(t, d_1, D_k)e^{j\omega_c t}\} \tag{4}$$

Using Eqs. 1, 3 and 4 we can see that the baseband equivalent signal waveform during the i^{th} symbol interval is

$$s(t, d_1, D_k) = \exp\left\{j\left[\frac{d_i \pi h(t-(i-1)T_s)}{T_s} + \pi h \sum_{j=1}^{i-1} d_j\right]\right\}. \tag{5}$$

Similarly, the noise n(t) can be represented as

$$n(t) = \mathrm{Re}\{\eta(t)e^{j\phi(t)}e^{j\omega_c t}\} \tag{6}$$

where

$$\eta(t) = \sqrt{n_c^2(t) + n_s^2(t)} \tag{7}$$

is the lowpass equivalent envelope and

$$\phi(t) = \tan^{-1}\frac{n_s(t)}{n_c(t)} \tag{8}$$

is the phase. We can then represent the received signal as

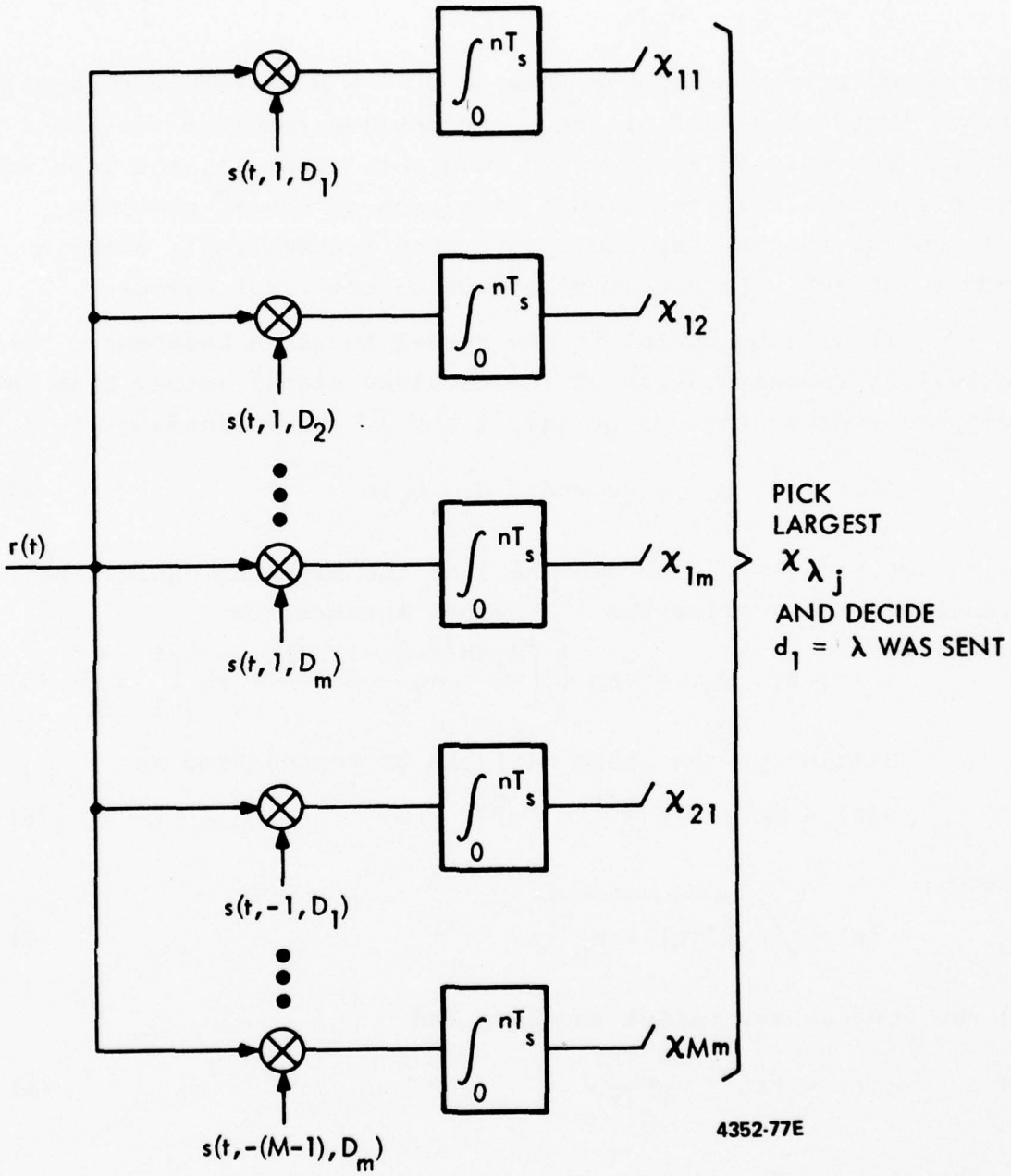


Figure 1. Optimum High SNR CPMFSK Receiver for Gaussian Noise

$$r(t) = \mathrm{Re}\left\{\left[\sqrt{\frac{2E_s}{T_s}}\, s\,(t, d_l, D_k) + \eta\,(t) e^{j\phi(t)}\right] e^{j\omega_c t}\right\} \qquad (9)$$
$$= \mathrm{Re}\left\{v(t)\, e^{j\alpha(t)}\, e^{j\omega_c t}\right\} = \mathrm{Re}\left\{r(t)\, e^{j\omega_c t}\right\}$$

where

$v(t)$ is the lowpass equivalent envelope of the signal plus noise, $\alpha(t)$ is the lowpass equivalent phase, and $r(t)$ is the complex lowpass equivalent received signal

$$r(t) = \sqrt{\frac{2E_s}{T_s}}\, s(t, d_l, D_k) + \eta(t)\, e^{j\phi(t)} \qquad (10)$$

Whereas in the bandpass representation, the output of one of the correlators is

$$x_{\lambda j} = \int_0^{nT_s} r(t)\, s(t, d_\lambda, D_j)\, dt, \qquad (11)$$

It can quickly be shown that the same output can be represented using the baseband equivalent signals as

$$x_{\lambda j} = 1/2\ \mathrm{Re}\left\{\int_0^{nT_s} r(t)\, s^*\,(t, d_\lambda, D_j)\, dt\right\} \qquad (12)$$

where $s^*\,(t, d_\lambda, D_j)$ indicates the complex conjugate of $s(t, d_\lambda, D_j)$.

The alternate complex baseband representation of the received signal as envelope and phase as indicated in Eq. 9 is

$$r\,(t) = v\,(t)\, e^{j\alpha(t)}. \qquad (13)$$

This representation is useful when examining receiver effects.

2.2 Receiver Representations

The receiver structures which were investigated during this study can be depicted as shown in Figure 2. The received signal is processed in a prediction filter to limit the input bandwidth of the additive noise. The predetection filters considered in this report are the physically realizable Butterworth, Chebyshev, and Bessel bandpass filters. In terms of the complex baseband equivalent signals, as shown in [8],

$$y(t) = \int_{-\infty}^{\infty} h(\tau)\, r(t-\tau)\, d\tau \tag{14}$$

where $h(t)$ is the complex baseband equivalent impulse response of the filter. Since $y(t)$ is also complex, it can be represented in terms of an envelope and phase

$$y(t) = \rho(t)\, e^{j\beta(t)} \tag{15}$$

The zero memory nonlinearities are included in the receiver structure to limit or delete large impulsive noise spikes. The output of these nonlinearities can similarly be represented in envelope and phase form as

$$Z(t) = \xi(t)\, e^{j\zeta(t)} \tag{16}$$

where $\xi(t)$ and $\zeta(t)$ are functions of the input envelope and phase $\rho(t)$ and $\beta(t)$. In this study, we consider the commonly used nonlinearities of the bandpass clipper and the bandpass hole puncher or blanker as shown in Figure 3. For these nonlinearities, the output phase equals the input phase

$$\zeta(t) = \beta(t) \tag{17}$$

whereas the output envelope equals the input envelope up to a threshold and it equals a constant if the input envelope exceeds that threshold. That is,

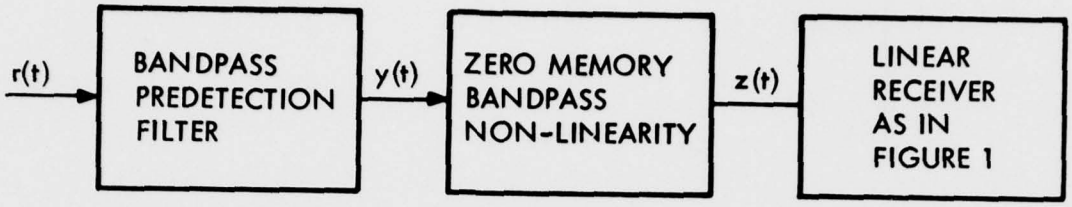
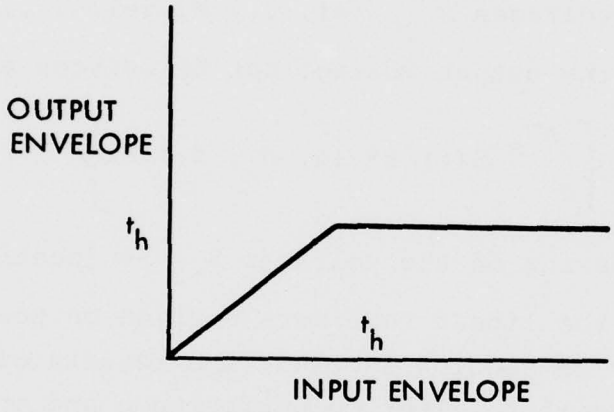
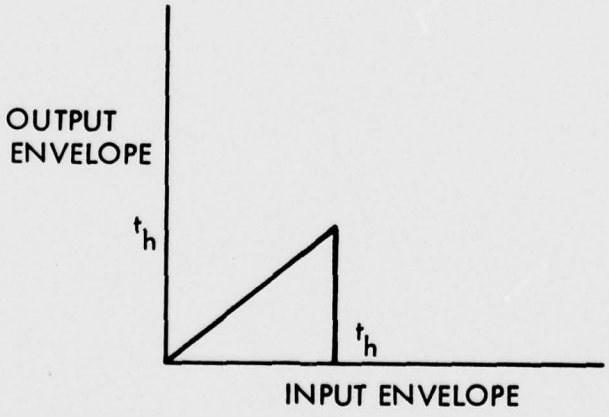


Figure 2: General Receiver Structure



(a) CLIPPER



(b) HOLE PUNCHER

Figure 3: Envelope Transfer Functions of Zero-Memory Bandpass Nonlinearities

$$\xi(t) = \begin{cases} \rho(t) & , \quad \rho(t) \leq t_h \\ K & , \quad \rho(t) > t_h \end{cases} \tag{18}$$

where t_h is the threshold; $K=t_h$ for a bandpass clipper and $K=0$ for a bandpass hole puncher.

After the nonlinearity, the signal $Z(t)$ is correlated in a linear receiver with all possible noise-free signals producing the M^n output voltages $x_{\lambda j}$, $\lambda=1, .., M$, $j=1, ..., m$. Similarly to Eq. 12, the output voltage can be written as

$$x_{\lambda j} = 1/2 \text{ Re} \left\{ \int_0^{nT_s} Z(t)\ s^*(t, d_\lambda, D_j)\ dt \right\} \tag{19}$$

The rest of the processing on the voltages $x_{\lambda j}$ is identical to that which exists in the linear receivers derived on the Gaussian noise channel [2-4]. In Section 3 below, the results of the effects of the predetection filter on performance and one receiver implementation based upon the MLSE algorithm are presented.

3. Receiver Implementation Considerations

There were two separate phases of the study concerning receiver implementations. The first was to determine the effect of preceding the receiver with a realizable bandpass filter. The second was to consider more realistic receiver implementations than the mathematical structure of Figure 1. The MLSE algorithm receiver is discussed.

3.1 Predetection Filter Effects

Three generic types of realizable filters were considered: the Butterworth, Chebyshev, and Bessel. In addition, filter order of 2, 3 and 4 were evaluated for each filter type. For the Chebyshev filter, a .1 dB passband ripple was considered.

The transfer functions and impulse responses of these filters can be found in a number of references, however they will be included here for completeness. Table 1 gives the transfer functions and impulse responses of Butterworth filters normalized to a lowass 3 dB bandwidth of 1 rad/sec. Similarly, Table 2 gives the same information for Chebyshev filters with passband ripple of .1 dB. For Bessel filters, the normalized lowpass transfer functions are not normally designed for a 3 dB bandwidth of 1 rad/sec., but rather for a constant group path delay. Correspondingly, the transfer functions and impulse responses must be frequency scaled. It is necessary to know the normalized 3. dB bandwidths. In Table 3 is shown the normalized transfer function, the frequency transformation b, and the corrected impulse responses. The Laplace transform relationship

$$H\ (bs) \longleftrightarrow \frac{1}{b}\ h\ \left(\frac{t}{b}\right) \tag{20}$$

is used.

Table 1: Transfer Functions and Impulse Responses for Lowpass Butterworth Filters

Order	Transfer Function H(s)	Impulse Response h(t)
2	$\frac{1}{s^2 + 1.414s + 1}$	$1.414e^{-.707t}\sin .707t$
3	$\frac{1}{(s + 1)(s^2 + 1.848s + 1)}$	$e^{-t}+1.155e^{-\frac{1}{2}t}\sin (.866t+1.047)$
4	$\frac{1}{(s^2 + .765s+1)(s^2 + 1.848s+1)}$	$2.416e^{-.924t}\sin (.382t+.392) - e^{-.382t}\sin(.924t+1.178)$

Table 2: Transfer Functions and Impulse Responses for Lowpass Chebyshev Filters (.1 dB ripple)

Order	Transfer Function H(s)	Impulse Response h(t)
2	$\frac{3.27}{s^2 + 2.36s + 3.31}$	$2.37e^{-1.18t}\sin(1.38t)$
3	$\frac{1.59}{(s + .969)(s^2+.97s + 1.69)}$	$.941e^{-.969t}+1.014e^{-.485t}\sin(1.206t-1.19)$
4	$\frac{.817}{(s^2+.528s+1.33)(s^2+1.275s+.622)}$	$1.426e^{-.638t}\sin(.464t + .285) - .59e^{-.264t}\sin(1.123t + .747)$

Table 3. Transfer Functions and Impulse Responses for Lowpass Bessel Filters

Order	Transfer Function H(s)	Frequency Transformation	Impulse Response h(t)
2	$\frac{3}{s^2 + 3s + 3}$	1.35	$2.556e^{-1.11t}\sin(.6415t)$
3	$\frac{15}{(s + 2.322)\ (s^2+3.67\ s+6.47)}$	1.75	$2.588e^{-1.327t}$ $+2.685e^{-1.05t}\sin(1.002t-1.302)$
4	$\frac{105}{(s^2+5.77\ s+9.07)\ (s^2+4.207\ s+11.6)}$	2.1	$8.152e^{-1.379t}\sin(.413t+.196)$ $-2.66e^{-t}\ \sin(1.265t+.638)$

In choosing a predetection filter, two requirements are desired. First it is desirable in many applications that the filter bandwidth be narrow so that the noise power which reached the correlators is small. If zero-memory nonlinearities are used, it has been found that wider bandwidths are more desirable. Secondly, the filter bandwidth should be large enough to effectively pass the signal without distortion. The block diagram of Figure 4 depicts the technique which was used in this study to determine one effect of the predetection filter.

One of the M^n complex baseband equivalent signals $s(t,d_l, D_k)$ is chosen randomly. It is passed through a filter with impulse response $h(t)$. The output signal is then correlated with an unfiltered version of itself. The delay compensation is necessary to correct for the group path delay through the filter. From [9], the group path delays for the nine filters of consideration is shown in Table 4. These group path delays are for the normalized bandwidths of 1 rad/sec. For other bandwidths, they must be adjusted by

$$t_{new} = t_{old} \quad \frac{B_{old}}{B_{new}} \tag{21}$$

where t_{old} is the group path delay as indicated in Table 4, and B_{new} is the new bandwidth in rad/sec. B_{old} = 1 rad/sec.

Clearly, if there were no filter in Figure 4, the output of the correlation would be

$$x_{lk} = \frac{1}{2} \quad Re\left\{ \int_0^{nT_s} |s(t,d_l, D_k)|^2 \, dt \right\} = \frac{nT_s}{2} \tag{22}$$

Hence, we define a correlation degradation as

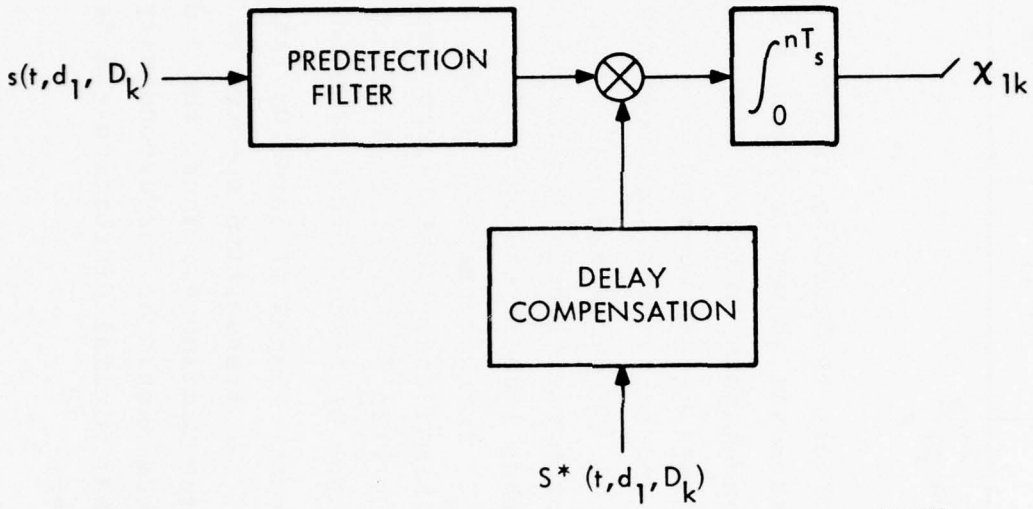


Figure 4. Technique to Determine Effect of Predection Filter

Table 4. Group Path Delays (sec) for Filters Normalized to Bandwidths of 1 rad/sec.

Filter type	Order		
	2	3	4
Butterworth	1.6	2.3	3.1
Chebyshev	.8	1.85	2.8
Bessel	1.45	1.85	2.19

$$C_d = 20 \log \frac{2x_{1k}}{nT_s} \tag{23}$$

It is difficult to directly relate C_d to the error rate performance because noise is not included in Figure 4 and the effect on other correlators (refer to Figure 1) is not being included. Nevertheless, C_d can be used as a guide in choosing predetection filters and bandwidths such that negligible distortion occurs in the signal. Figures 5,6, and 7 show C_d as a function of 3 dB bandwidth. From the figures, it can be seen that x_{1k} is degraded by less than 1 dB if the one-sided 3 dB bandwidth is greater than $.6/T_s$. Furthermore, the effect of different filters appears to be a minimal one. That is, as long as the filter bandwidth is moderately wide ($>.6/T_s$), it does not seem to matter too much what filter type or filter order is being used.

For quaternary CPMFSK of large deviation ratios (i.e., h = .6 or h = .8), the transmitted spectra is considerably larger than for h = .4 (see Section 6.) Thus, the 3 dB bandwidths of predetection filters should be correspondingly larger in these cases to ensure that minimal distortion and degradation is introduced by the filter.

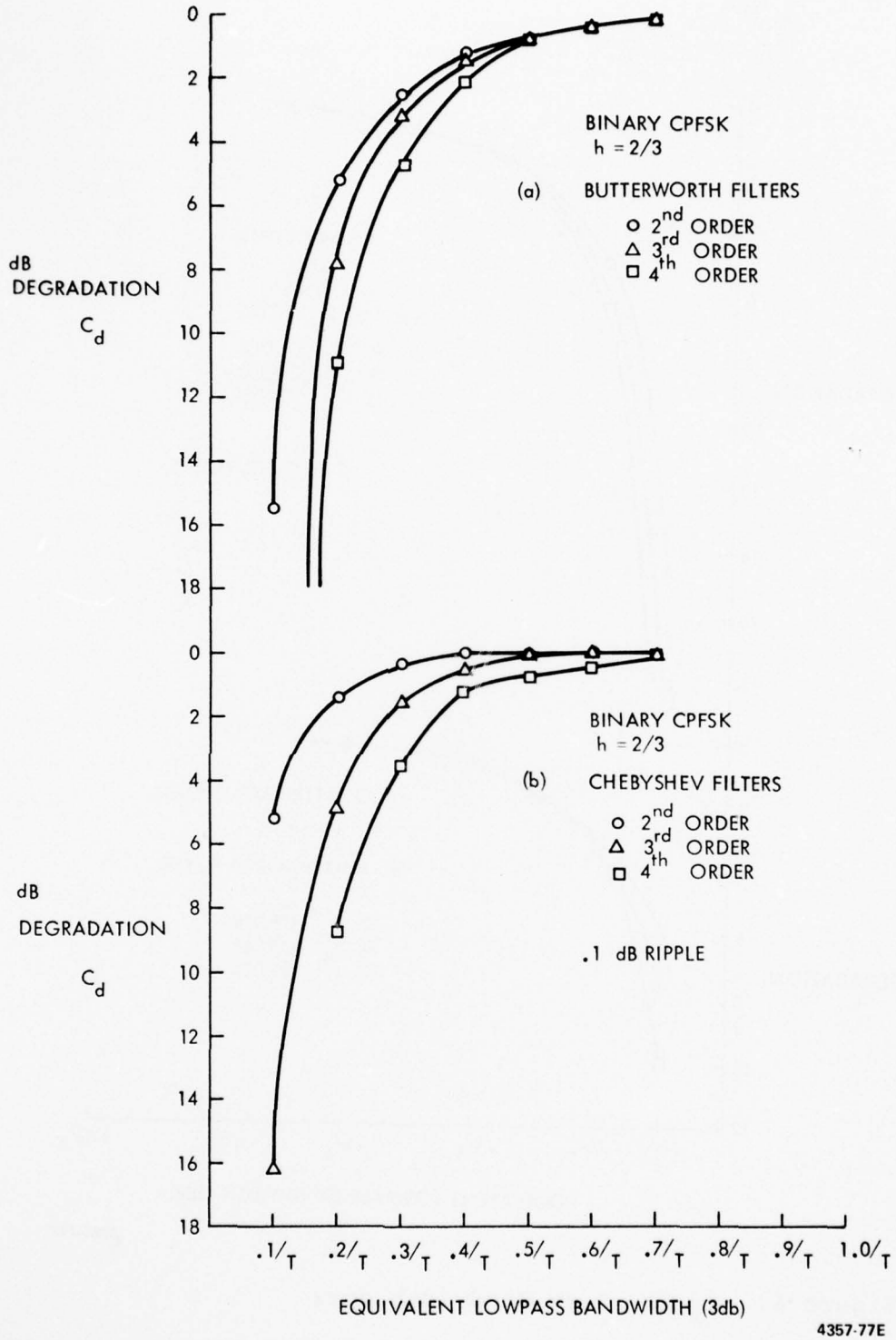


Figure 5. C_d vs. 3 dB Bandwidth for Binary CPMFSK and Various Filters: (a) Butterworth; (b) Chebyshev

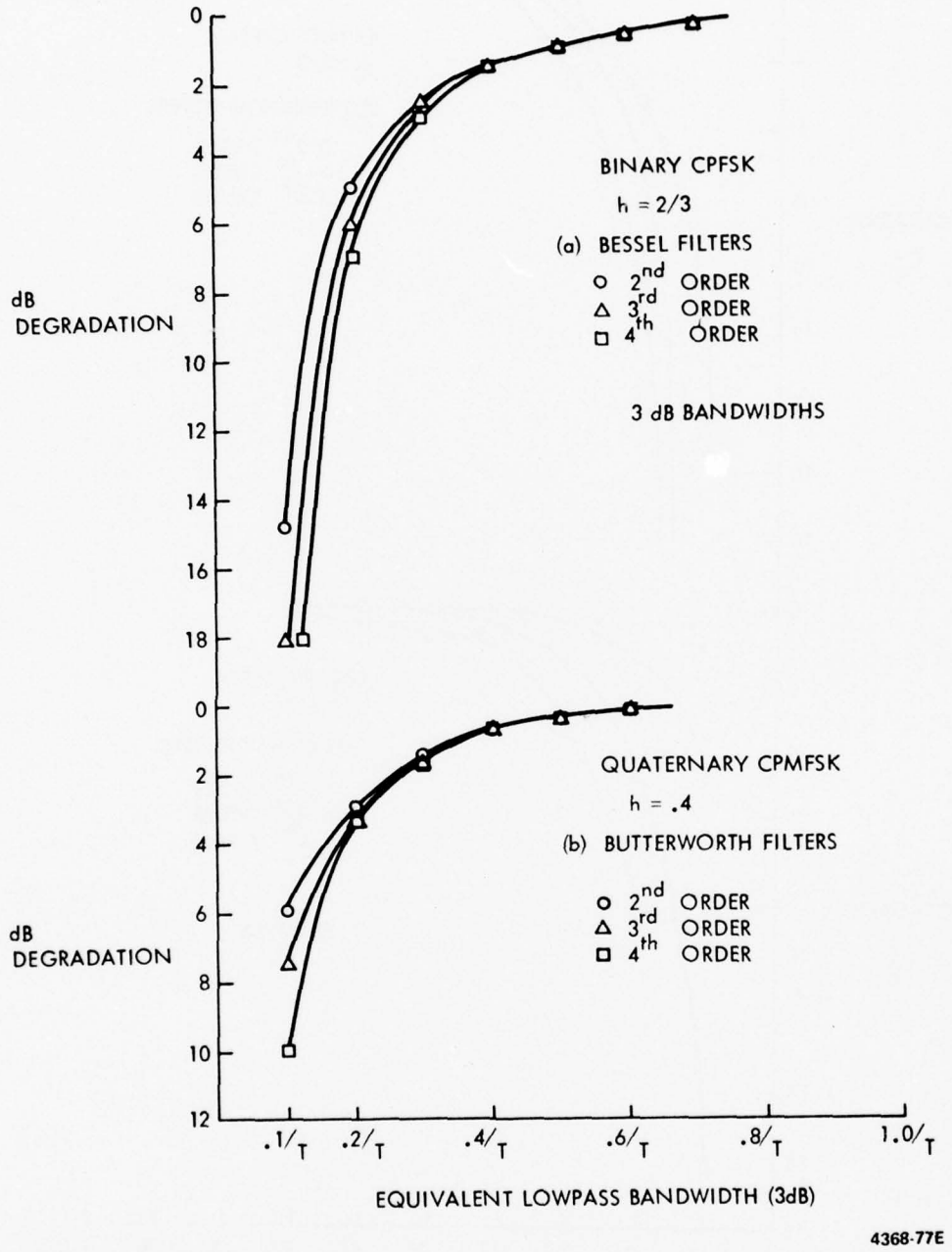


Figure 6. C_d vs. 3 dB Bandwidth for:

(a) Binary CPFSK with Bessel Filter

(b) Quaternary CPMFSK with Butterworth Filter

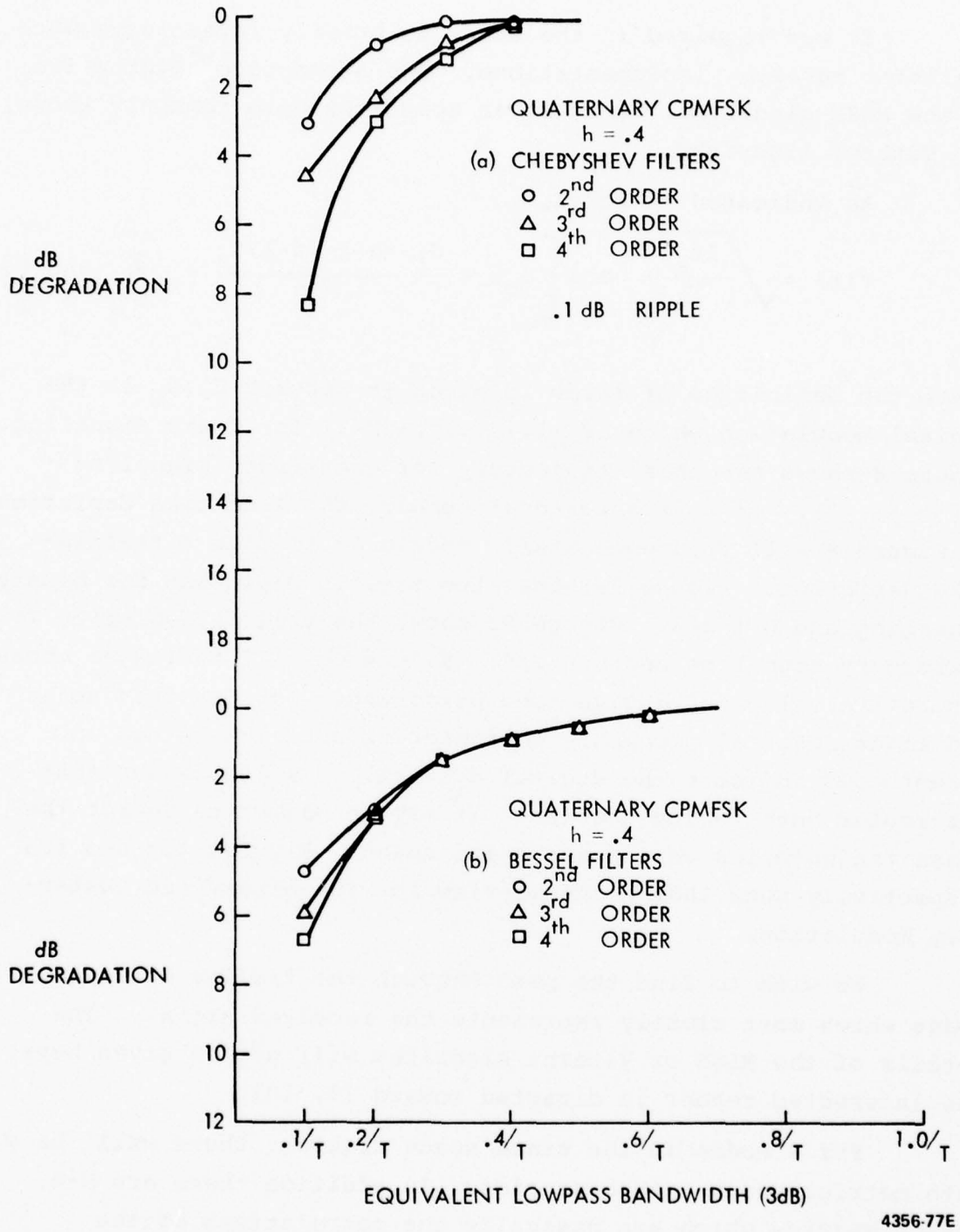


Figure 7. C_d vs. 3 dB Bandwidth for Quaternary CPMFSK and Various Filters (a) Chebyshev; (b) Bessel

3.2 Use of the MLSE Algorithm

It was required in the study to briefly investigate more realistic receiver implementations. One attractive alternative is the MLSE algorithm, or as it is sometimes more commonly known, the Viterbi Algorithm

As indicated in Eq. 1,

$$r(t) = \sqrt{\frac{2E_s}{T_s}} \cos\left[\omega_c t + \frac{d_i \pi h (t-(i-1)T_s}{T_s} + \sum_{j=o}^{i-1} \pi h d_j\right] \quad (24)$$

where the definition of terms is given in Section 2. d_i is the digital modulation which is $\pm 1, \pm 3, \ldots, \pm(M-1)$ for M-ary signaling. Figure 8 shows the phase trajectory for quaternary signaling ($d_1 = \pm 1, \pm 3$). If h is a rational number, the tree-like depiction of Figure 8 will fold upon itself modulo 2π to give a trellis-like depiction. Figure 9a shows the trellis depiction for binary signaling and h = 2/3. Figure 9b shows the trellis depiction for quaternary signaling and h = 2/5. Reference [11] indicates these respective values of h give good performance for Gaussian noise and tight spectral occupancy characteristics. The values in parentheses indicate the digital $d_i = \pm 1, \pm 3$ which causes that particular path in the trellis. It may be easier to depict the phase trajectories as a phase state space. Figures 10a and 10b respectively show that point-of-view for the binary and quaternary modulation.

We wish to find the path through the trellis or state space which most closely represents the received signal. The details of the MLSE or Viterbi Algorithm will not be given here. The interested reader is directed toward [7, 10].

For N nodes in the state space diagram, there will be N path metrics and N path histories. In addition there are M·N branch metrics which are basically the correlations of the

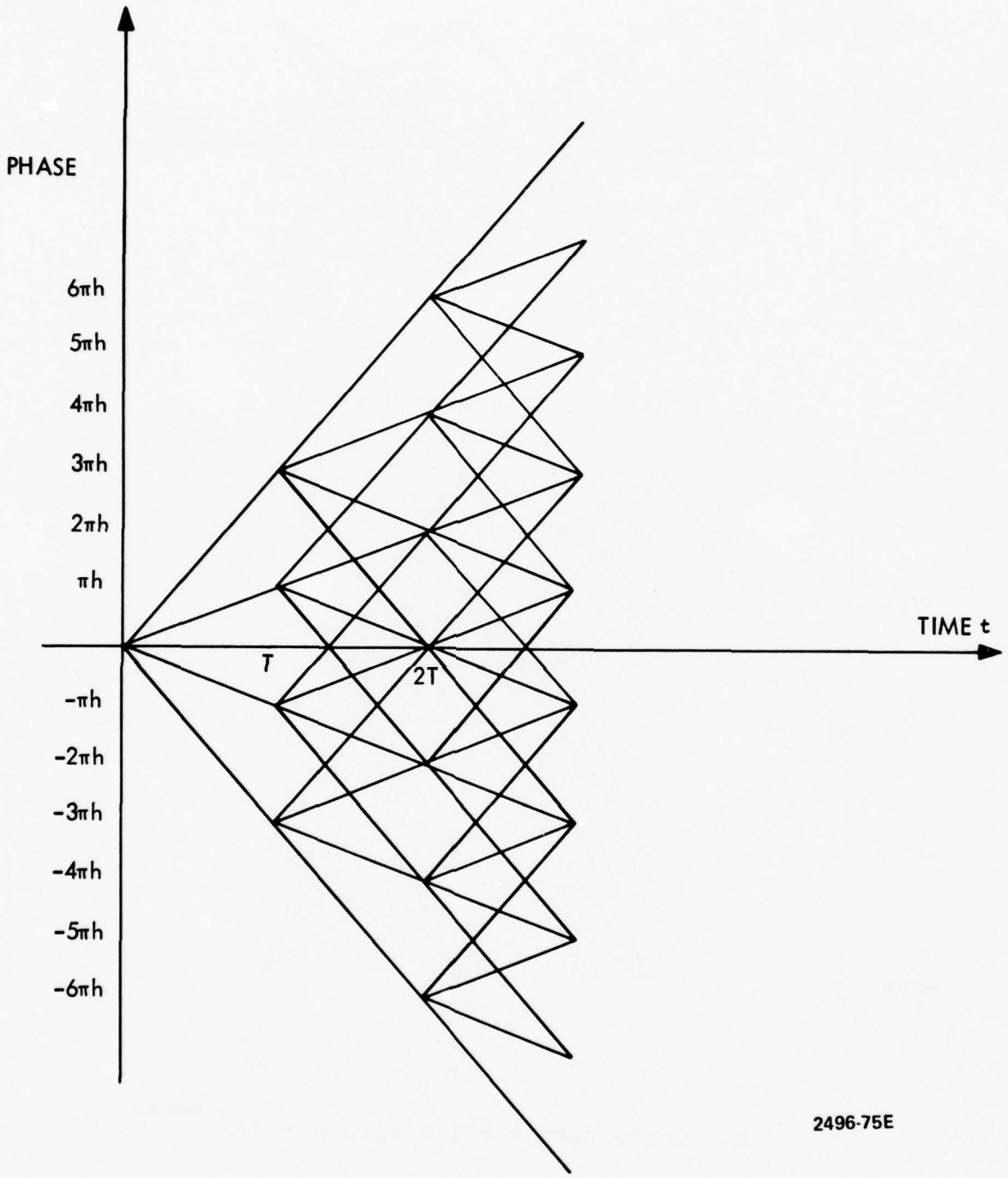
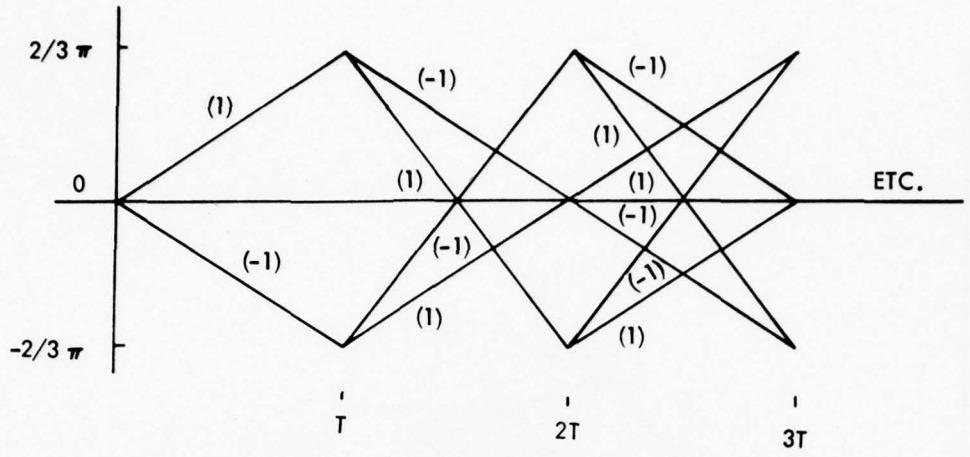
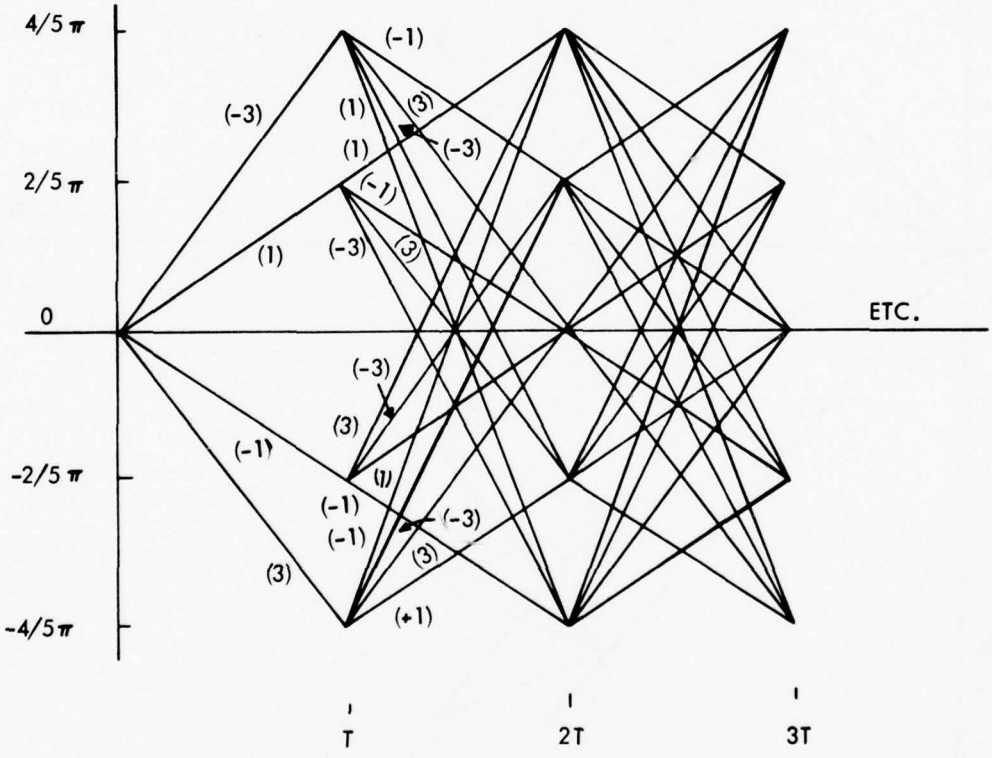


Figure 8. Phase Trajectories for Quaternary CPMFSK



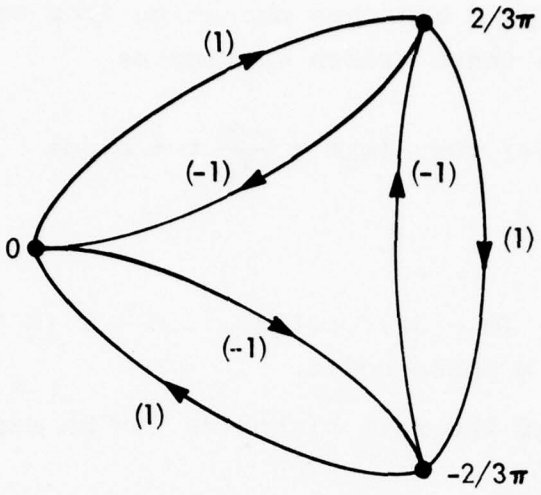
a. Binary Trellis with h = 2/3



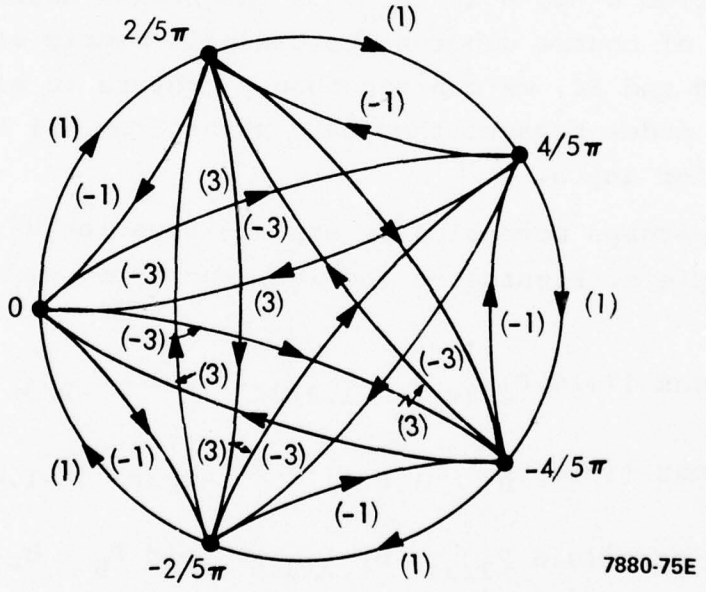
b. Quaternary Trellis with h = 2/5

7877-75E

Figure 9: Phase Trellises for Some CPMFSK Signals



a. Binary with h = 2/3



b. Quaternary with h = 2/5

Figure 10: Phase State Representation of Phase Trajectories

received signal with the M branches emanating from each of the N nodes. If we denote these branch metrics as

$$b_{mn} = \int_{o}^{T_s} r(t) \cos \left[\omega_c t + \frac{m\pi h}{T_s} t + n\right] dt \qquad (25)$$

where $m = -(M-1), -(M-3), \ldots, 1, 3, \ldots, M-1$ (M terms) and n represents one of the N phase nodes.

The updating of the path histories can be expressed as

$$\text{new } P_n = \max_{n'} [\text{old } P_{n'} + b_{mn'}] \qquad (26)$$

where new P_n is the new updated path metric for the n^{th} phase node, the maximization is accomplished over only those n' which have paths from n' to n and $b_{mn'}$ is the branch metric from n' to n. Old $P_{n'}$ of course denotes the old path metric at n'. Referring to Figures 9 and 10, we can see that n' refers to all of the other n - 1 phase nodes because there are paths from all other phase nodes to n for any n.

To perhaps more clearly explain Equation 26, for the binary example of Figures 9a and 10a, the three updates of path metrics are

$$\begin{aligned}
\text{new } P_o &= \max [(\text{old } P_{2/3\pi} + b_{-1,2/3\pi}), (\text{old } P_{-2/3\pi} + b_{1,-2/3\pi})] \\
\text{new } P_{2/3\pi} &= \max [(\text{old } P_0 + b_{1,0}), (\text{old } P_{-2/3\pi} + b_{-1,-2/3\pi})] \qquad (27) \\
\text{new } P_{-2/3\pi} &= \max [(\text{old } P_{2/3\pi} + b_{1,2/3\pi}), (\text{old } P_0 + b_{-1,0})]
\end{aligned}$$

For each P_n, after the n' which accomplishes Equation 26 is found, the path histories are updated. The path history update can be expressed as

$$\text{new } H_n = \text{old } H_{n'}, \; m \tag{28}$$

which shows that the new path History H_n is produced by appending to the old $H_{n'}$ the data digit m which corresponds to the branch from n' to n. The n' used is of course the one which satisfies Equation 26 for each n.

Ideally, we would like to collect path metrics and path histories for the entire duration of a message. In practice, it has been found that it is not necessary to wait until the end of a message to start making symbol estimates, but after some delay D estimates can be made. Hence, once the length of the histories equals D, a path is chosen which has the largest path metric and the oldest symbol in that path history is chosen as the symbol estimate of a previous received symbol with delay D.

The choice of D depends upon the application, and was investigated by simulation.

Monte Carlo simulations programs were developed and exercised for the binary case with h = 2/3, corresponding to Figures 9a and 10a. Gaussian noise was used, and Figure 11 shows the simulated probability of bit error results, as circles on the graph. These results are for a Viterbi Algorithm delay D = 3. Also shown is the theoretical bound from [11] which approximates the error performance of a correlation receiver which observes three bits (n = 3) before a decision is made. As can be seen, the performance of both techniques are equivalent.

If the Viterbi Algorithm delay D is increased, performance will improve, and if decisions are delayed until the entire message has been sent, the best performance possible will result. However, this is not truly necessary for eventually a point is reached for which an increasing of D beyond that point achieves virtually the same results.

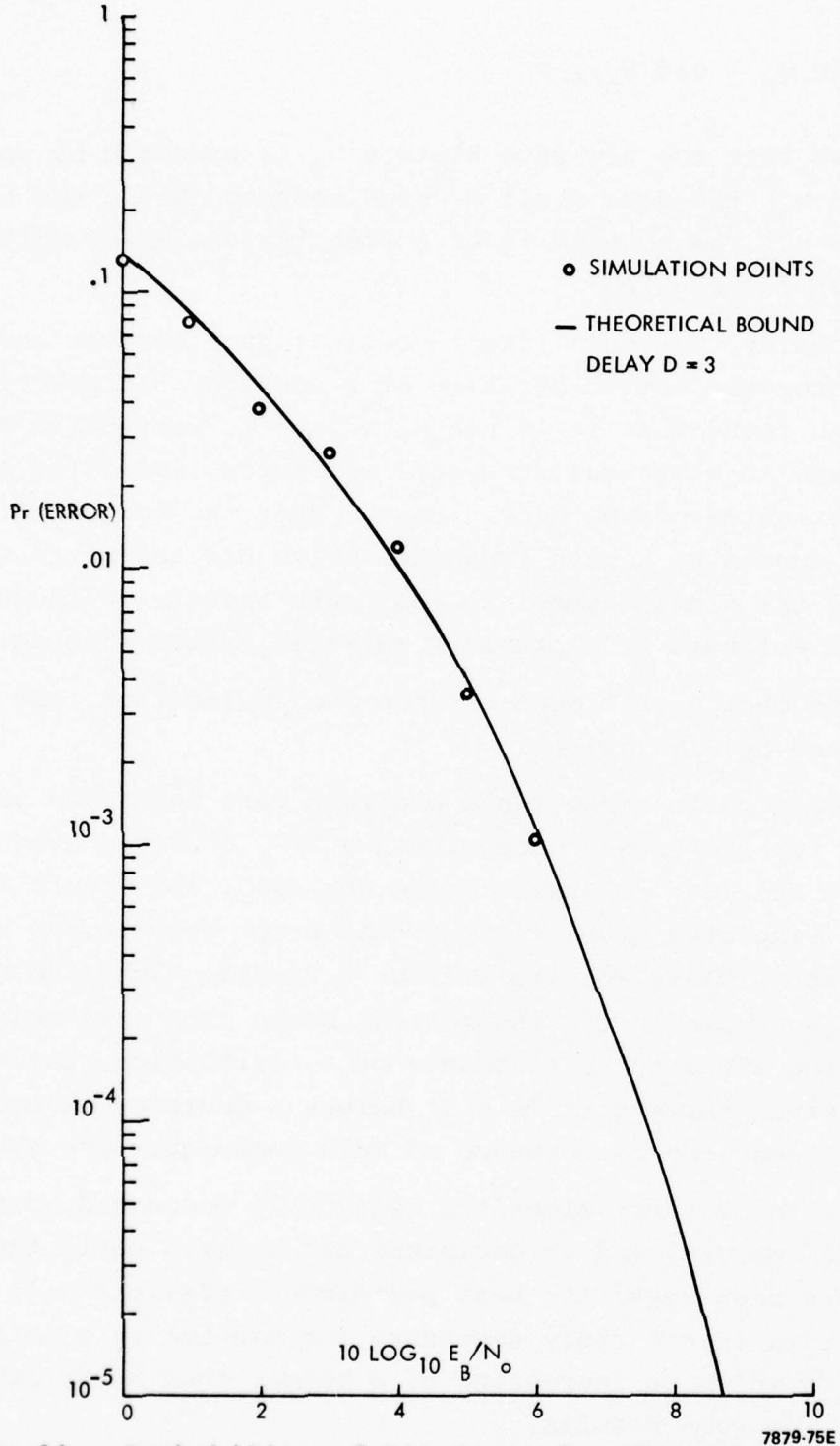


Figure 11: Probability of Bit Error for Viterbi Algorithm Demodulation - Binary Signaling h = 2/3

Figure 12 shows some simulated results for D = 2, 3, and 5. Results were also obtained for D = 7, but they are graphically indistinguishable from the D = 5 points. This same improvement can be achieved by using a correlation receiver which observes five bits (n = 5), but this requires an increase in equipment complexity, whereas the Viterbi Algorithm Receiver does not.

The Viterbi Algorithm Receiver is only practical when the deviation ratio h is a rational number such that the state space depiction of Figure 10 has a small number of phase nodes. Fortunately, CPMFSK is a modulation which is robust enough such that these "convenient" values of h result in good performance.

Equation 25 implies that M·N correlators are required. This, in fact, is unnecessary as we can see by rewriting Equation 25 as

$$b_{mn} = \cos(n) \int_0^{T_s} r(t) \cos\left[\omega_c t + \frac{m\pi h}{T_s} t\right] dt - \sin(n) \int_0^{T_s} r(t) \sin\left[\omega_c t + \frac{m\pi h}{T_s} t\right] dt \quad (29)$$

Since the N phase nodes are known, it can be seen that only two quadrature correlators are required for each m. Denoting these by

$$x_m = \int_0^{T_s} r(t) \cos\left[\omega_c t + \frac{m\pi h}{T_s} t\right] dt$$

and (30)

$$y_m = \int_0^{T_s} r(t) \sin\left[\omega_c t + \frac{m\pi h}{T_s} t\right] dt$$

b_{mn} can be written as

$$b_{mn} = \cos(n) \cdot x_m - \sin(n) \cdot ym \quad (31)$$

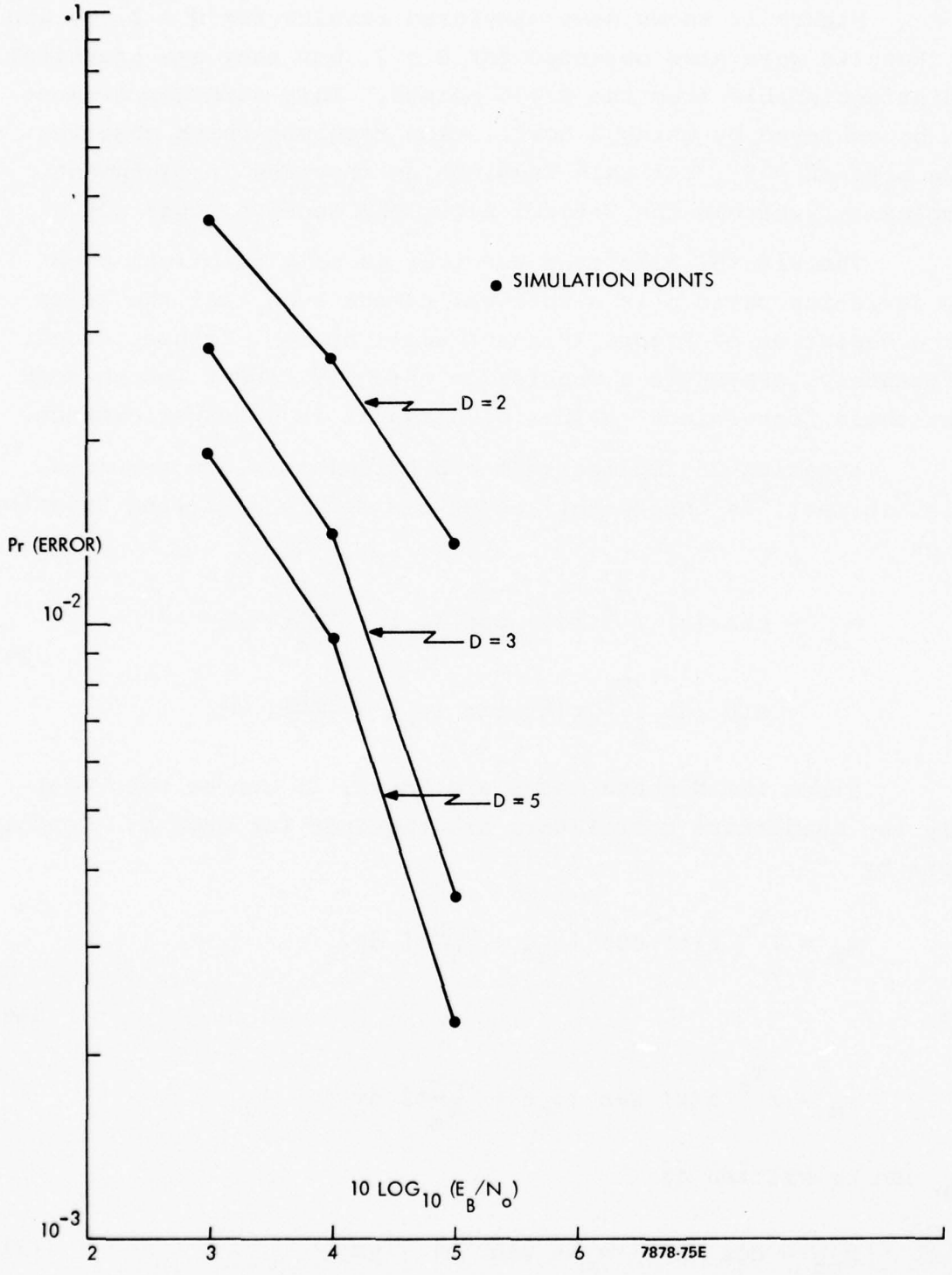


Figure 12: Effect of Change in D on Probability of Bit Error Binary Modulation (h = 2/3)

Hence, a total of 2M correlators are required for M-ary modulation rather than N·M. Figure 13 shows the functional block diagram of a binary receiver ($m = \pm 1$) with $h = 2/3$ ($n = 0, \frac{2}{3}\pi, -\frac{2}{3}\pi$).

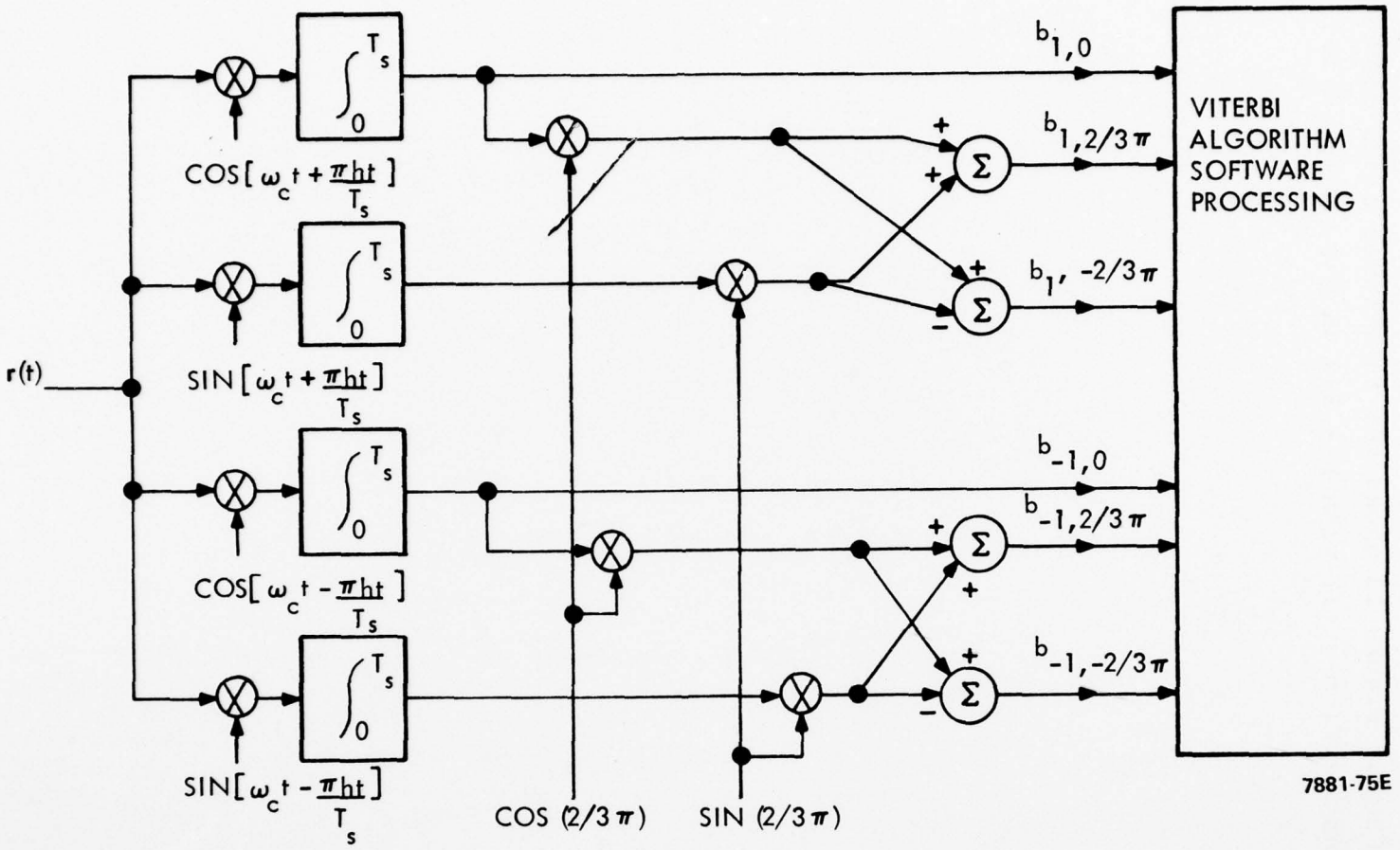


Figure 13: Functional Block Diagram of Binary Receiver with Viterbi Algorithm Demodulation

4. Noise Models

Three noise models were used during the course of the study: two are suitable for theoretical analysis, and one for simulation purposes. Two techniques were used to specify the models. First, the models were required to have finite V_d ratios, which is defined in terms of the rms to average envelope levels as

$$V_d = 20 \log \frac{\sqrt{\mu_2}}{\mu_1} \tag{32}$$

V_d is a commonly used parameter to specify the degree of impulsiveness of the noise. In Eq. 32, μ_j is the jth moment of the envelope of the noise. In terms of Eqs. 6 and 7,

$$\mu_j = \int_0^\infty \eta^j \, p_N(\eta) \, d\eta \tag{33}$$

where $p_N(\eta)$ is the envelope probability density function (pdf). For Gaussian (Rayleigh envelope) noise, V_d is 1.05 dB, whereas common values are 2-4 dB for HF channels and 10-15 dB for VLF channels.

The second technique used to specify the models is the empirical APD curves of [6]. Models which match these curves are preferred since they are obtained from measured data. The APD curve is a plot of the probability that the noise envelope exceeds a threshold R, i.e.

$$Pr(\eta > R) = \int_R^\infty p_N(\eta) \, d\eta \tag{34}$$

4.1 Analytical Noise Models

In this study, two basic noise models which achieve the joint goals of analytical tractability and correspondence with empirical APD curves and V_d ratios were considered. One of these models has been previously proposed by Hall [12], although for some V_d ratios, modification of the model was required. The other model, called a mixture model, represents the envelope noise process as a mixture of a Rayleigh process and an impulsive process to be defined.

4.1.1 The Hall Model

The Hall model can be represented by its envelope pdf

$$p(\eta) = \frac{(\theta-1)\gamma^{\theta-1}\eta}{\left[\eta^2+\gamma^2\right]^{\frac{\theta+1}{2}}} \qquad (35)$$

where θ is an integer ≥ 2 which is selected to match first order statistics. γ is a parameter related to the variance of the noise if this variance exists. The j^{th} moment of this process does not exist if $j \geq \theta-1$ so that in these cases modifications of the process is required to define a V_d ratio. Hall suggests one method of modifying the model so that finite moments result. The method proposed here is described below and differs from Hall's suggestion. Marginal density functions which represent the inphase and quadrature voltages n_c and n_s can be derived. For this model APD's can easily be determined and as seen in Figures 14 and 15 the match between the theoretical and empirical curves is quite evident.

The two parameters, θ and γ, of the Hall model whose envelope pdf is given in Eq. 35 above can be selected to provide good fits to the measured distributions of atmospheric noise. Integral values of θ in the range $2 \leq \theta \leq 5$ are commonly used. The distributions for which $\theta = 4$ and 5 represent moderately impulsive noise with $V_d = 3$ and 2 dB respectively and are parti-

cularly suited for modeling the first order noise statistics in mid-ocean regions. However, the moments, μ_j, of the Hall distributions diverge for $j \geq \theta-1$. Thus, the second moment of the distribution for $\theta = 3$ and the first and second moments for the $\theta = 2$ distribution do not exist. Consequently, for these distributions, the V_d ratio as defined in Eq. 32 is undefined and the distributions cannot be constrained to match the V_d ratio of the empirical data. However, truncation and appropriate normalization of these distributions force the moments to converge and result in a set of distributions whose V_d ratio is defined in terms of θ and the truncation level.

The truncation and normalization is accomplished by defining an envelope pdf as

$$P_E(\eta) = \begin{cases} \dfrac{b(\theta-1)\gamma^{\theta-1}\eta}{\left[\eta^2 + \gamma^2\right]^{(\theta+1)/2}} & 0 \leq \eta \leq E \\ 0 & \eta > E \end{cases} \tag{36}$$

and selecting b to provide

$$\int_0^E P_E(\eta)\, d\eta = 1 \tag{37}$$

These truncated distributions with $\theta = 2$ and 3 and the unmodified distributions with $\theta = 4$ and 5 constitute a family of curves which can be used to represent a wide range of measured data by exhibiting the same V_d ratio as the data and providing good fits to the observed APD's. The family is well-defined analytically and expressions can be obtained in closed form for the moments of the envelope, APD's and marginal pdf's of the quadrature voltage components. These statistics are summarized in Table 5.

Table 5. First Order Statistics of Truncated Hall Model

	HALL $\theta = 5$	HALL $\theta = 4$	TRUNCATED HALL $\theta = 3$	TRUNCATED HALL $\theta = 2$
ENVELOPE PDF $0 \le v \le \infty$	$\dfrac{4\gamma^4 v}{(v^2+\gamma^2)^3}$	$\dfrac{3\gamma^3 v}{(v^2+\gamma^2)^{5/2}}$	$\dfrac{D^2}{D^2-1}\ \dfrac{2\gamma^2 v}{(v^2+\gamma^2)^2}$, $0 \le v \le \gamma\sqrt{D^2-1}$ 0, $v > \gamma\sqrt{D^2-1}$	$\dfrac{D}{D-1}\ \dfrac{\gamma v}{(v^2+\gamma^2)^{3/2}}$, $0 \le v \le \gamma\sqrt{D^2-1}$ 0, $v > \gamma\sqrt{D^2-1}$
μ_1	$\dfrac{\gamma\pi}{4}$	γ	$\gamma\left\{\dfrac{D^2 \tan^{-1}(\sqrt{D^2-1})}{D^2-1} - \dfrac{1}{\sqrt{D^2-1}}\right\}$	$\dfrac{\gamma D}{D-1}\left\{\dfrac{-\sqrt{D^2-1}}{D} + \ln(D+\sqrt{D^2-1})\right\}$
μ_2	$\dfrac{3\pi\gamma}{4}$	2γ	$\gamma^2\left\{\dfrac{2D^2 \ln D}{D^2-1} - 1\right\}$	$\gamma^2(D-1)$
V_d	2.0 dB	3.0 dB	$20 \log\left\{\dfrac{\sqrt{D^2-1}\,(2D^2 \ln D - D^2+1)^{1/2}}{D^2 \tan^{-1}(\sqrt{D^2-1}) - \sqrt{D^2-1}}\right\}$	$20 \log\left\{\dfrac{(D-1)^{3/2}}{-\sqrt{D^2-1} + \ln(D+\sqrt{D^2-1})}\right\}$
APD $\Pr\{v > R\}$	$\dfrac{1}{\left(1+\dfrac{R^2}{\gamma^2}\right)^2}$	$\dfrac{1}{\left(1+\dfrac{R^2}{\gamma^2}\right)^{3/2}}$	$\dfrac{D^2}{D^2-1}\left[\dfrac{1}{\left(1+\dfrac{R^2}{\gamma^2}\right)} - \dfrac{1}{D^2}\right]$	$\dfrac{D}{D-1}\left[\dfrac{1}{\left(1+\dfrac{R^2}{\gamma^2}\right)^{1/2}} - \dfrac{1}{D}\right]$
VOLTAGE PDF	$\dfrac{3\gamma^4}{4(x^2+\gamma^2)^{5/2}}$	$\dfrac{2\gamma^3}{(x^2+\gamma^2)^2}$	$\dfrac{D^2}{(D^2-1)\pi}\ \dfrac{\gamma}{(x^2+\gamma^2)^{3/2}}\left\{\tan^{-1}\sqrt{\dfrac{\gamma^2D^2}{x^2+\gamma^2}-1} - \dfrac{\sqrt{\gamma^2D^2-(x^2+\gamma^2)}\ \sqrt{(x^2+\gamma^2)}}{\gamma^2D^2}\right\}$, $\lvert x\rvert < \gamma\sqrt{D^2-1}$ 0, $\lvert x\rvert > \gamma\sqrt{D^2-1}$	$\left[\dfrac{1}{(D-1)\pi}\ \dfrac{\sqrt{\gamma^2D^2-(x^2+\gamma^2)}}{(x^2+\gamma^2)}\right]$, $\lvert x\rvert \le \gamma\sqrt{D^2-1}$ 0, $\lvert x\rvert > \gamma\sqrt{D^2-1}$

The marginal pdf is obtained from the envelope pdf through the transformation $n_c = \eta \cos \phi$ and $n_s = \eta \sin \phi$ where ϕ is independent of η and is assumed to be uniformly distributed in the interval $(0, 2\pi)$. The details of the derivation of the expressions in Table 5 are provided in Appendix B.

The correspondence between the theoretical APD expressions which are presented in Appendix B and the empirical CCIR results given in [6] are graphically displayed in Figures 14 and 15. A normalized parameter Δ is defined as

$$\Delta = 20 \log_{10} \left(\frac{\eta}{\eta_{rms}}\right) \tag{38}$$

where $\eta_{rms} = \sqrt{\mu_2}$ and the figures display the probability that Δ is exceeded. These parameters correspond to those used in reference [6], and the empirical results displayed in [6] are shown as isolated points in the figures. The solid or dotted lines correspond to the theoretical APD expressions as stated in Table 5.

Figures 14 and 15 show the results for the Hall and truncated Hall model. Only for $V_d = 2$ dB, for which $\theta = 5$, can the original Hall model be used. For all other results in the figures, it was necessary to use the truncated models with either $\theta = 3$ or $\theta = 2$. It was found experimentally that $\theta = 3$ gives the best fit to the CCIR curves when $4 \leq V_d \leq 6$. For V_d larger than 6, $\theta = 2$ gives the best fit. Clearly the fit is good for all the curves.

This noise model has also been used in a study to evaluate low probability of intercept communications in a broadband spread spectrum system using PSK as a modulation [13].

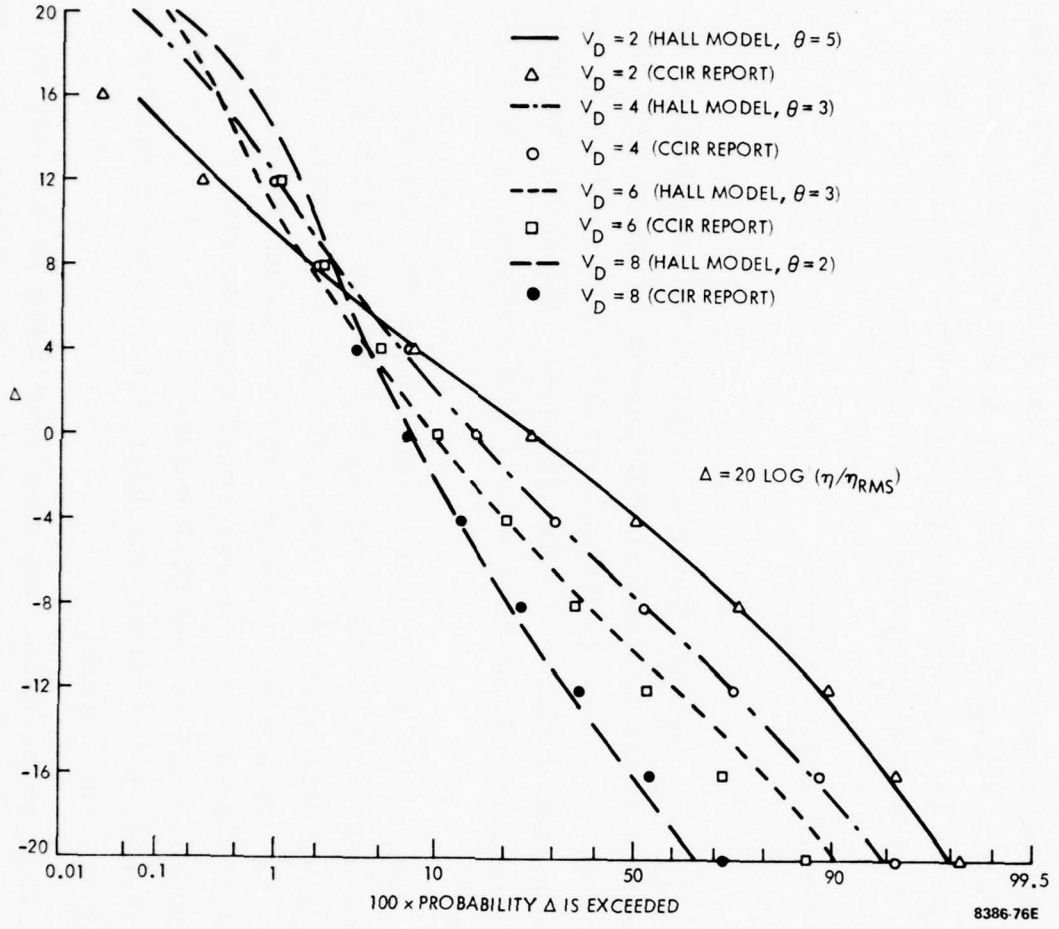


Figure 14: APD for Empirical and Truncated Hall Model (V_d=2,4,6, and 8)

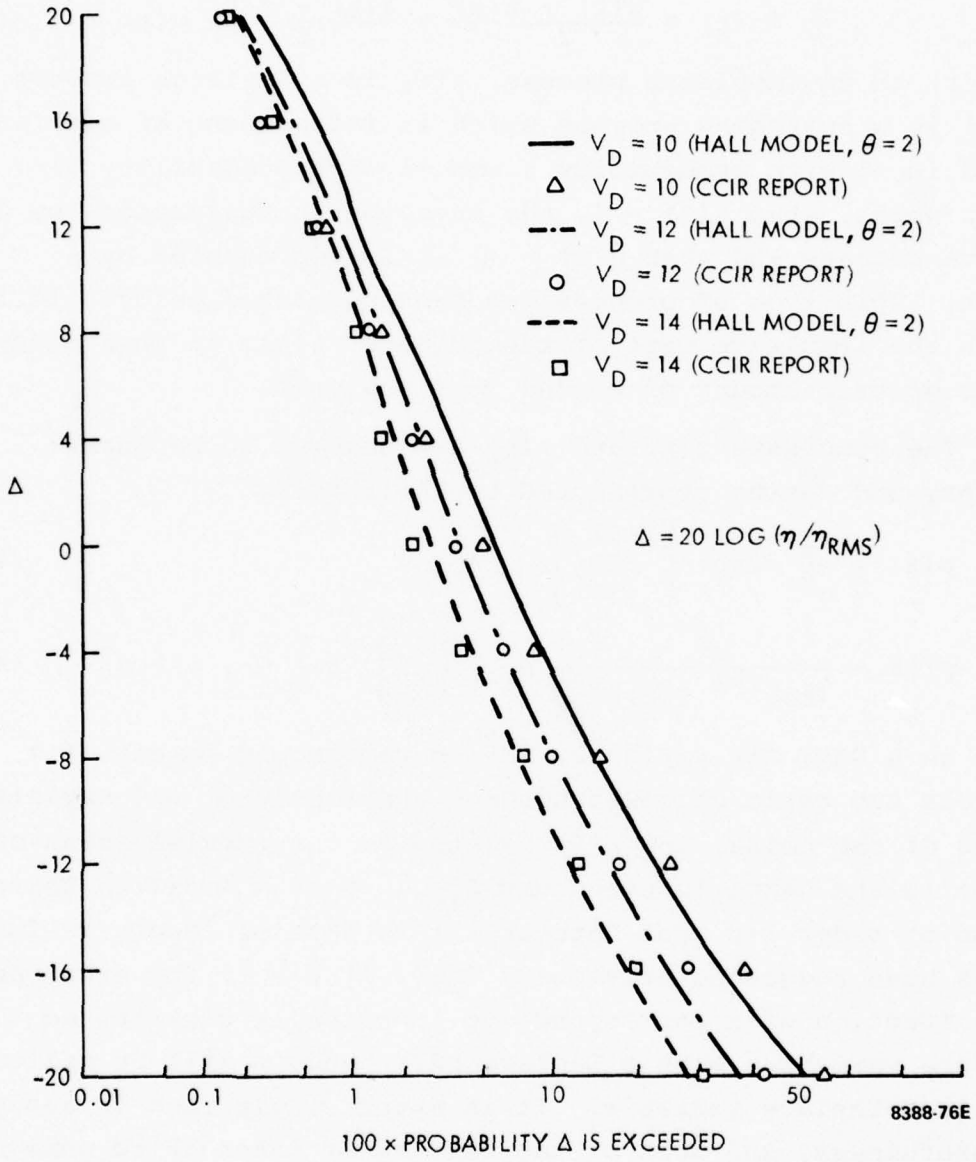


Figure 15: APD for Empirical and Truncated Hall Model (V_d=10, 12, and 14)

4.1.2 The Mixture Model

The mixture model considered here is represented by its envelope process

$$\eta(t) = \frac{s(t) + z(t)}{2} + \frac{s(t) - z(t)}{2} u(t) \qquad (39)$$

where s(t) is an impulsive process, z(t) is a Rayleigh process, and u(t) is a switching process which is independent of s(t) and z(t) and is +1 with probability ε and -1 with probability 1-ε. In other words, when u(t) = 1, the envelope is represented by an impulsive process and when u(t) = -1 it is represented by a Rayleigh. This type of process has been suggested before [14,15], although the impulsive part of the process, s(t), in this study allows a greater amount of closed form analysis.

The processes z(t) and s(t) are assumed to be quasi-stationary and can be represented by their pdf's

$$p(z) = \frac{z}{\sigma^2} \exp\left[-\frac{z^2}{2\sigma^2}\right], \quad z \geq 0 \qquad (40)$$

$$p(s) = \frac{s^r}{(k\sigma)^{r+1}\,\Gamma(r)\,2^{r-1}} K_{1-r}\left[\frac{s}{k\sigma}\right], \quad s \geq 0\ ,\ r > 0 \qquad (41)$$

where z is a Rayleigh variable, $2\sigma^2$ is the second moment of z, k controls the ratio of power between the impulsive and Rayleigh portions of the noise, and r is related to the impulsiveness of s. $\Gamma(r)$ is the Gamma function and $K_{1-r}(\ )$ is a modified Bessel function of order 1-r. For integer r this form of impulsive function has been suggested previously [16]. If r = 1, the envelope density function of s corresponds to identically distributed quadrature variables with a Laplace pdf; hence s will be called a generalized Laplace variable. It is surprisingly rich in analytical usefulness, and most of the results of interest to communications engineers can be expressed in closed form.

The j^{th} moment of s can be found from equation (41) using item 6.561-16 in [17], i.e.,

$$E\{s^j\} = \frac{(2k\sigma)^j}{\Gamma(r)} \Gamma(1+\tfrac{j}{2}) \Gamma(r+\tfrac{j}{2}) \tag{42}$$

Specifically the mean is

$$E\{s\} = \frac{k\sigma \sqrt{\pi}\Gamma(r+\frac{1}{2})}{\Gamma(r)} \tag{43}$$

and the second moment is

$$E\{s^2\} = 4r(k\sigma)^2 \tag{44}$$

The probability that s exceeds some fixed threshold R is

$$Pr\{s > R\} = \int_R^\infty p(s)ds = \left(\frac{R}{k\sigma}\right)^r \frac{1}{2^{r-1}\Gamma(r)} K_r\left(\frac{R}{k\sigma}\right) \tag{45}$$

If it is assumed that s is the envelope of two quadrature variables x and y, the pdf of x (or y) is

$$p(x) = \frac{|x|^{r-\frac{1}{2}}}{(k\sigma)^{r+\frac{1}{2}} \sqrt{\pi}\Gamma(r) 2^{r-\frac{1}{2}}} K_{\frac{1}{2}-r}\left(\frac{|x|}{k\sigma}\right) \tag{46}$$

Eqs. (45) and (46) are derived in Appendix C. Returning to the mixture model, it is clear that the j^{th} moment of η is

$$\begin{aligned} \mu_j &= E\{\eta^j | u = 1\} \; Pr\{u = 1\} + E\{\eta^j | u = -1\} \; Pr\{u = -1\} \\ &= \varepsilon \; E\{s^j\} + (1-\varepsilon) \; E\{z^j\} \end{aligned} \tag{47}$$

Specifically, the mean is

$$\mu_1 = \frac{\varepsilon k\sigma\sqrt{\pi}\,\Gamma\left(r+\frac{1}{2}\right)}{\Gamma(r)} + (1-\varepsilon)\sqrt{\frac{\pi}{2}}\,\sigma\ , \tag{48}$$

the second moment is

$$\mu_2 = \varepsilon 4rk^2\sigma^2 + (1-\varepsilon)2\sigma^2 \tag{49}$$

It follows that

$$V_d = 20\ \log\left[\frac{\sqrt{4rk^2\varepsilon + (1-\varepsilon)2}}{\frac{\varepsilon k\sqrt{\pi}\,\Gamma\left(r+\frac{1}{2}\right)}{\Gamma(r)} + (1-\varepsilon)\sqrt{\frac{\pi}{2}}}\right]. \tag{50}$$

Similarly, the APD is

$$\Pr\{\eta > R\} = \Pr\{\eta > R|u = 1\}\ \Pr\{u = 1\} + \Pr\{\eta > R|u = -1\}$$

$$\Pr\{u = -1\} \tag{51}$$

$$= \varepsilon\left(\frac{R}{k\sigma}\right)^r \frac{1}{2^{r-1}\Gamma(r)} K_r\left(\frac{R}{k\sigma}\right) + (1-\varepsilon)\ \exp\ -\left(\frac{R^2}{2\sigma^2}\right)$$

Figures 16 and 17 display the results for the mixture model. For $V_d = 2$, this model does not achieve as good a fit as does the Hall model. Nevertheless there is still a clear correspondence between the theoretical APD curves as derived in the model and the empirically determined results from [6].

There are three parameters, namely r, ε, and k, to pick in the mixture model. The parameters were chosen to best match the empirical results with the constraint that the theoretical

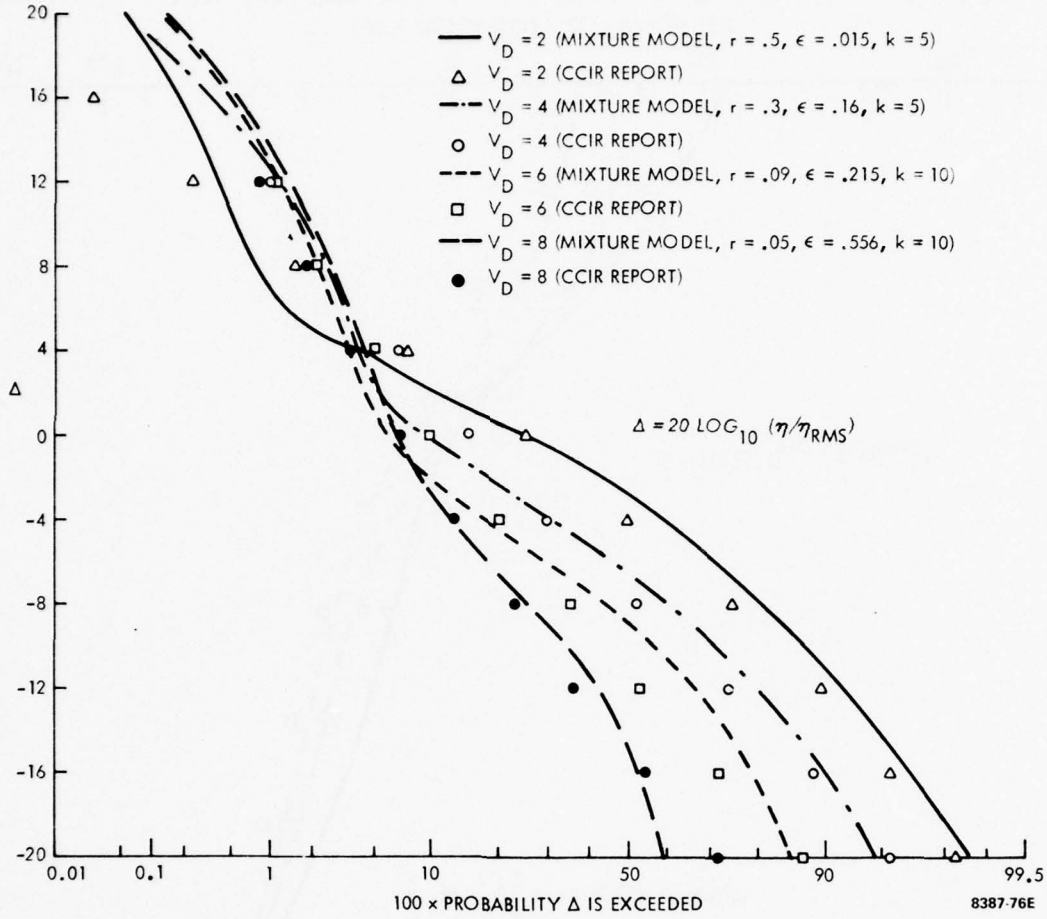


Figure 16: APD for Empirical and Mixture Model (V_d = 2,4,6, and 8)

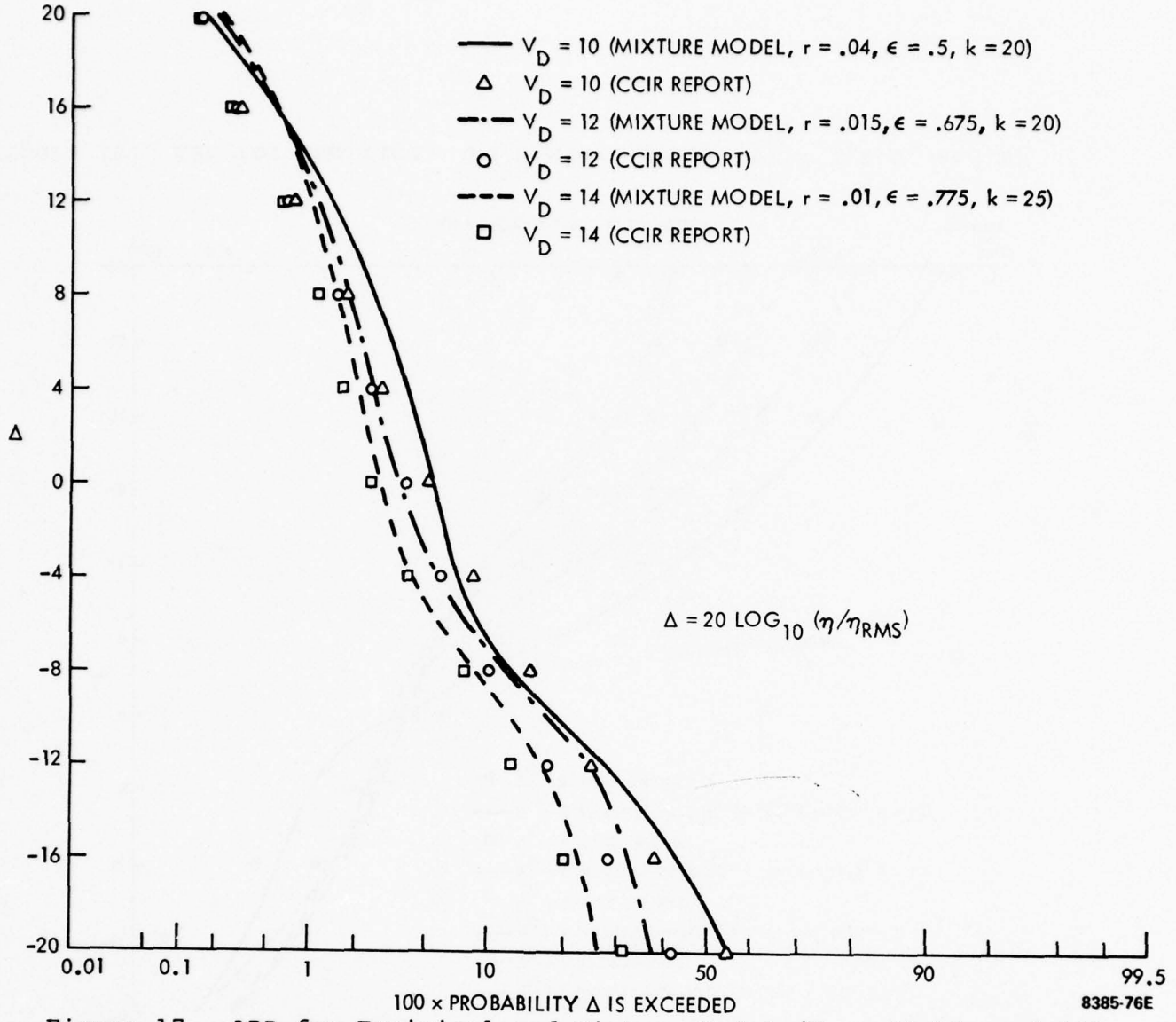


Figure 17. APD for Empirical and Mixture Model (V_d = 10,12, and 14)

V_d ratio as defined in Eq. (50) be met. It can be seen that as the noise becomes more impulsive, i.e., the V_d ratio get larger, r becomes smaller and ε and k get larger.

It is of interest to note that all the moments of x and the exceedance probabilities of x can also be derived where x is a quadrature variable of the impulsive envelope s(Eq. 46).

Namely, the moments are seen to be

$$E\{x^j\} = \int_{-\infty}^{\infty} x^j\, p(x)\, dx = \begin{cases} 0, & j \text{ odd} \\ \dfrac{(2k\sigma)^j}{\sqrt{\pi}\,\Gamma(r)} \cdot \Gamma\left(\dfrac{1+j}{2}\right) \Gamma\left(r+\dfrac{j}{2}\right), & j \text{ even} \end{cases} \tag{52}$$

Regarding the exceedance probabilities,

$$\int_R^{\infty} p(x)\, dx = \int_R^{\infty} \frac{x^{r-\frac{1}{2}}}{(k\sigma)^{r+\frac{1}{2}}\sqrt{\pi}\,\Gamma(r)\,2^{r-\frac{1}{2}}} K_{\frac{1}{2}-r}\left(\frac{x}{k\sigma}\right)$$

$$= \frac{1}{2} - \int_0^R \frac{x^{r-\frac{1}{2}}}{(k\sigma)^{r+\frac{1}{2}}\sqrt{\pi}\,\Gamma(r)\,2^{r-\frac{1}{2}}} K_{\frac{1}{2}-r}\left(\frac{x}{k\sigma}\right) \tag{53}$$

From [17, item 6.561(4)] with a suitable change of variable, this results in

$$\int_R^{\infty} p(x)\, dx = \frac{1}{2} - \frac{R}{2k\sigma}\left[K_{\frac{1}{2}-r}\left(\frac{R}{k\sigma}\right) L_{\frac{3}{2}-r}\left(\frac{R}{k\sigma}\right) + L_{\frac{1}{2}-r}\left(\frac{R}{k\sigma}\right) K_{\frac{3}{2}-r}\left(\frac{R}{k\sigma}\right)\right] \tag{54}$$

where $L_u(\cdot)$ is the Modified Struve Function.

4.2 Simulation Noise Model

The simulation noise model used in this study is based upon the Crichlow graphical model for the APD of the noise envelope [18].

The Crichlow model works with a special type of probability graph paper; paper on which the power Rayleigh functions plot as straight lines (a Rayleigh function plots as a straight line with slope = -0.5). The coordinate transformations for the probability paper are (see Appendix D):

$$x' = -20 \log_{10} (-\ln x)$$

$$y' = 20 \log_{10} y \qquad (55)$$

where x = the precentage of time for which the ordinate is exceeded; and $y = n/n_{rms}$.

On this probability paper, the APD of atmospheric noise can be represented by a three-section curve (see Figure 18). The lower region of the curve, representing random low voltages and high probabilities, approaches a Rayleigh distribution. It can be, therefore, approximated by a straight line (R). The higher region of the curve, representative of impulsive high voltages and low probabilities, approaches a power Rayleigh distribution. It can also be approximated by a straight line (PR). The center region of the curve corresponds to an arc of a circle tangent to the two straight lines.

The arc is also tangent to the line (T), which is parallel to line (BI) which bisects the acute angle formed by the intersection of the Rayleigh and power Rayleigh lines.

Four parameters are necessary in order to specify a unique pair of lines and an arc. They are:

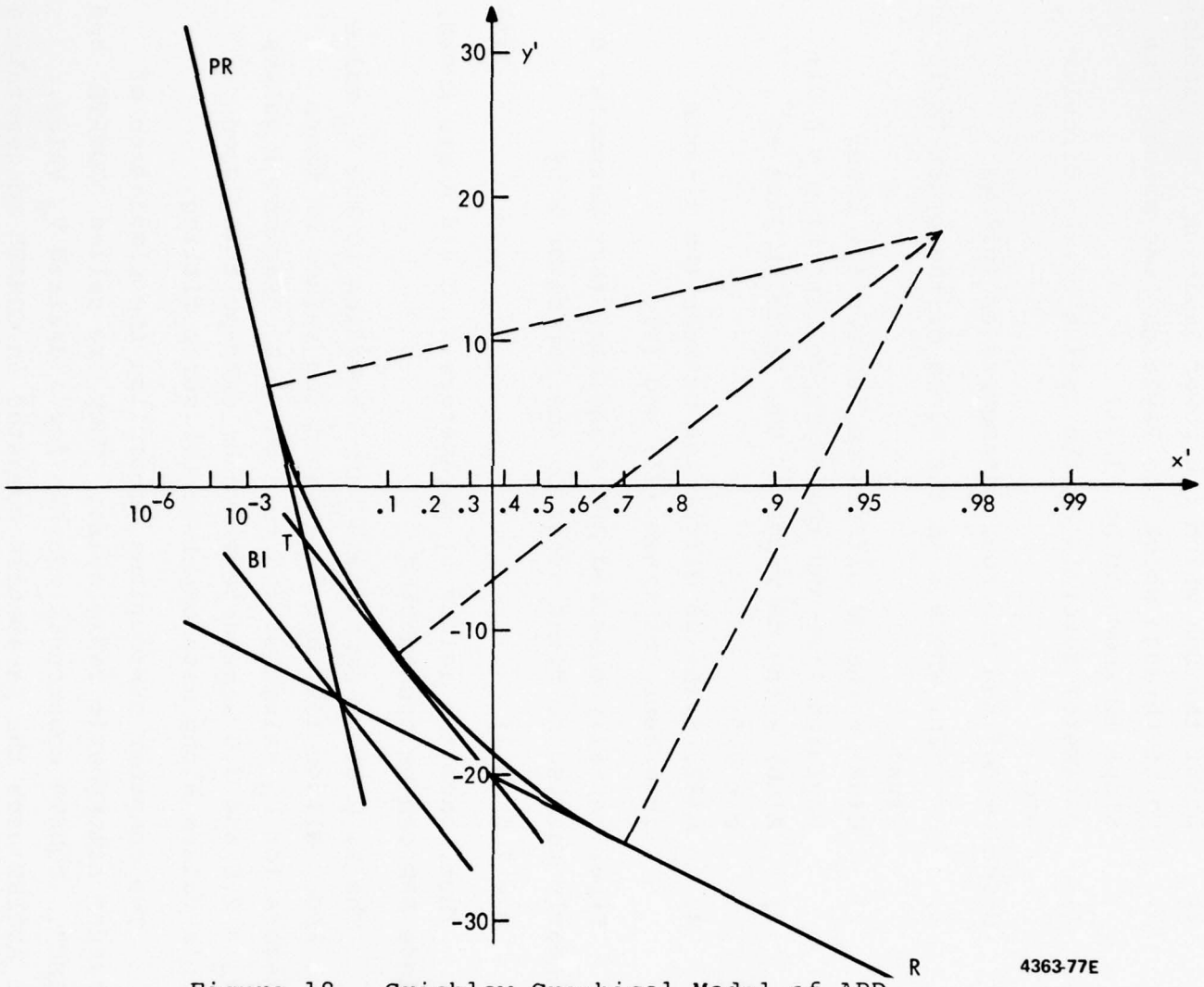


Figure 18. Crichlow Graphical Model of APD of Atmospheric Noise

1) slope of the power Rayleigh line;
2) point through which the power Rayleigh line passes;
3) point through which the Rayleigh line passes (the Slope is known to be -1/2);
4) parameter determining the radius of the circular arc.

Crichlow defined the four parameters as follows

1) X = -2s, where s is the slope of the power Rayleigh line;
2) C(dB) = the dB difference between the power Rayleigh line and the Rayleigh line at p = 0.01;
3) A(dB) = the dB value of the Rayleigh line at p = 0.5;
4) B(dB) = the dB difference between the y'-axis intercepts of lines (BI) and (T).

Experimentally measured APD's indicate that parameter B is linearly related to first order to the parameter X by

$$B = 1.5\ (X-1) \tag{56}$$

Thus, once the values of parameters X, C and A are known, a unique APD can be constructed.

The X, C and A parameters vary according to the V_d value of the APD. Wilson [19] has calculated the values of these parameters for V_d values of 4.0 through 30.0. Parameter values for V_d = 2.0 and 3.0 were determined by extrapolating upon Wilson's values along with experimental curve fitting.

Two computer subroutines accomplish the simulation of the random atmospheric radio noise. They are called "CONSTR" and "ANOISE". CONSTR constructs the APD for a desired V_d value, while ANOISE uses the parameters computed in CONSTR to generate a random number with APD of atmospheric noise. The simulation is broken up into two separate procedures since in order to simulate

atmospheric radio noise with a certain V_d value subroutine ANOISE will be called repetitively; while the parameters for the APD for this certain V_d value have to be calculated only once.

Subroutine CONSTR accepts for input the value of V_d variable. It then looks-up the X, C and A parameters corresponding to the V_d value. At present, the subroutine has memory of the three parameters for V_d values of 2.0 through 16.0, in steps of 1.0. Parameters for the intermediate values of V_d are computed by linear interpolation. Using the three parameters, CONSTR then "constructs" the APD according to the Crichlow graphical model.

The output of the CONSTR subroutine consists of the two parameters defining the borders between the three regions of the APD; and the seven parameters necessary for the construction of different sections of the APD:

1-2) slope and y'-intercept of the Rayleigh line;
3-4) slope and y'-intercept of the power Rayleigh line;
5-7) x' and y' coordinates of the center of the circular arc, and its radius.

The nine parameters computed by the subroutine CONSTR constitute the input to the subroutine ANOISE.

In subroutine ANOISE, first a uniform random number between 0 and 1.0 is generated; this number represents the abscissa value. It is then transformed into the x' coordinate. Decision is made as to within which of the three regions of the APD the random value falls, and the y' coordinate (n/n_{rms}) is computed using the appropriate equation. The value of n/n_{rms} is then transformed from dB to volts. If an instantaneous quadrature voltage is desired, the resulting n/n_{rms} voltage is multiplied by cos $2\pi u$ where u is another random number between 0 and 1.

The above pair of subroutines was thoroughly tested with a total of 20,000 random numbers generated by CONSTR and ANOISE, for each of ten different V_d values. The APD's were then determined for the ten types of noise. These APD's of atmospheric radio noise as determined by experimental measurements [6]. This can be seen in Figure 19 for V_d ratios of 2, 6, 10, and 14 dB.

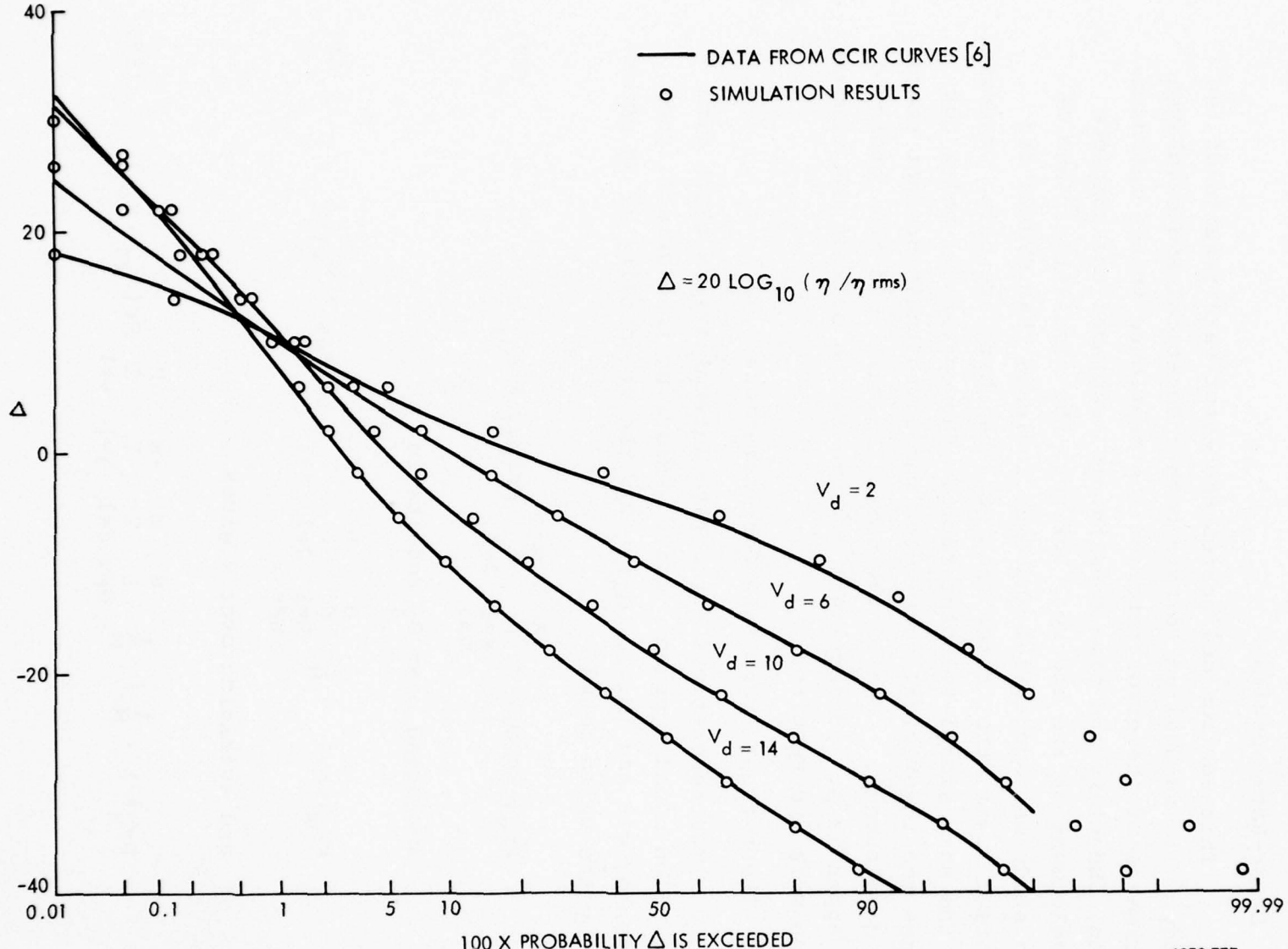


Figure 19 . APD for Empirical and Simulation Model

5. Error-Rate Results

This section delineates the error-rate results of the study. It was desired to have both theoretical and simulated estimates of the error rate, but as mentioned in the introduction, budgetary and time constraints precluded the complete development of the theory. However, the simulation phase of the study was successful and does indicate that CPMFSK can achieve lower error rates than MSK when both are being processed at the same signal-to-noise ratio. Subsection 5.1 below outlines the theoretical considerations up to their present stage of development. Much of the detail calculations are consigned to Appendix A. Subsection 5.2 presents the bulk of the simulation work and results.

5.1 Theoretical Error Rate Considerations

The theoretical error rate determinations start with the union bound approach [2,4]. Referring to Figure 1, and given $d_1 = \nu$ and $\{d_2,\ldots,d_n\} = D_j$, the probability of an error is by the union bound

$$Pr_M(\varepsilon|\nu,D_j) < \sum_{\substack{N=1 \\ N\neq\nu}}^{M} \sum_{J=1}^{m} Pr(x_{NJ} > x_{\nu j}). \tag{57}$$

Averaging over D_j results in

$$Pr_m(\varepsilon|\nu) < \frac{1}{M} \sum_{\substack{N=1 \\ N\neq\nu}}^{M} \sum_{J=1}^{m} \sum_{j=1}^{m} Pr(x_{NJ} > x_{\nu j}) \tag{58}$$

and averaging over ν gives

$$Pr_M(\varepsilon) < \frac{1}{M} \cdot \frac{1}{m} \sum_{\substack{N=1 \\ N\neq\nu}}^{M} \sum_{J=1}^{m} \sum_{j=1}^{m} \sum_{\nu=1}^{M} Pr(x_{NJ} > x_{\nu j}) \tag{59}$$

We have now reduced the problem from the determination of error rates for M-ary communications to the binary problem of the probability that one variable x_{NJ} exceeds another $x_{\nu j}$. Referring to Eq. 19, we can see that the binary probability can be written as

$$\Pr\,(x_{NJ}>x_{\nu j}) = \Pr\{\mathrm{Re}[\int_0^{nT_s} z(t)s^*(t,d_N,D_J)\,dt > \int_0^{nT_s} z(t)s^*(t,\,d_\nu,\,D_j)dt]\} \tag{60}$$

or

$$\Pr(x_{NJ}>x_{\nu j}) = \Pr\{\mathrm{Re}[\int_0^{nT_s} z(t)\{s^*(t,\,d_N,\,D_J) - s^*(t,\,d_\nu,\,D_j)\}dt]\} \tag{61}$$

Eq. 61 indicates that the problem requires the evaluation of stochastic integrals. It is possible to do this for Gaussian noise and linear receivers, however there are few general approaches that can be used to evaluate these integrals. Specifically, there are three difficulties with evaluating Eq. 61 in the general case of CPMFSK:

(1) If the receiver is nonlinear, the statistics of z(t) are difficult to determine. On the other hand, if the receiver is linear,

$$z(t) = \sqrt{\frac{2E_s}{T_s}}\; s(t,\,d_\nu,\,D_j) + \eta\,(t)\; e^{\,j\phi(t)}$$

and techniques can be developed to estimate the integral. This is outlined below in section 5.1.1.

(2) $s^*(t,\,d_N,\,D_j)$ and $s^*(t,\,d_\nu,\,D_j)$ are functions of time which change appreciably during the integral period nT_s. This is different than the approach which could be taken with PSK type modulations, for which the baseband equivalent representations are constant during symbol intervals.

(3) $s^*(t, d_N, D_J)$ and $s^*(t, d_\nu, D_j)$ are not orthogonal in general. In specific instances where the deviation ratio h is a multiple of 1/2, the different baseband equivalent signals are orthogonal, and certain simplifying calculations can be made to Eq. 61. This is explained in Section 5.1.2.

5.1.1 Linear Receiver Approach

As is well known [8] when a waveform z(t) is correlated as in Eq. 61 with a local signal $[s^*(t, d_N, D_J) - s^*(t, d_\nu, D_j)]$, this is equivalent mathematically to passing the signal z(t) through a filter with impulse response

$$\bar{h}(t) = s^*(nT_s - t, d_N, D_J) - s^*(nT_s - t, d_\nu, D_j) \tag{62}$$

and sampling the output at time nT_s. Furthermore, if the receiver is linear the input can be represented as

$$z(t) = \sqrt{\frac{2E_s}{Ts}}\, s(t, d_\nu, D_j) + \eta(t)e^{j\phi(t)} \tag{63}$$

where $\eta(t)$ and $\phi(t)$ are the envelope and phase of an impulsive noise process. It is known [20] that when an impulsive process is passed through a filter whose noise bandwidth is less than the spectral occupancy of the original process, the output noise is still impulsive but with a smaller V_d ratio.

Hence, if we define y to be the decision variable

$$y = \mathrm{Re}\int_o^{nT}\left[\sqrt{\frac{2E_s}{T_s}}\, s\,(t, d_\nu, D_j) + \eta(t)\, e^{j\phi(t)}\right]\left[s^*(t, d_N, D_J) - s^*\,(t, d_\nu, D_j)\right] dt \tag{64}$$

where we have suppressed the functional dependence of y on N, J, ν, and j, y is an impulsive voltage function with nonzero mean. Thus, we can model y in terms of the analytical noise models of Section 4.1. As can be surmised in Table 5 and Eqs. 39 and 46, three parameters will suffice to model y; the mean and variance of the voltage and the V_d ratio of the envelope. From Eq. 64,

$$E\{y\} = \sqrt{\frac{2E_s}{T_s}} \cdot nT_s \ (\rho_{NJ',\nu j}-1) \tag{65}$$

where

$$\rho_{NJ,\ \nu j} = \frac{1}{nT_s} \int_0^{nT_s} \mathrm{Re}\left[s(t,\ d_\nu,\ D_j)\ s^*(t,\ d_N,\ D_J)\right] dt \tag{66}$$

Similarly, the variance of y is

$$\mathrm{Var}\{y\} = \sigma_\eta^2 \int_0^{nT_s} |h(t)|^2 \tag{67}$$

where h(t) is as defined in Eq. 62, and σ_η^2 is of course the variance of the input noise process. From this, we can see that

$$\mathrm{Var}\{y\} = 2\sigma_\eta^2\ nT_s\ (1-\ \rho_{NJ',\nu j}) \tag{68}$$

To determine the modeled V_d ratio of y, we assume that the input V_d ratio of η is known, and that the RF/IF input noise bandwidth is B_1 where

$$B_1 > \frac{1}{T_s} .$$

The noise bandwidth of a filter with impulse response h(t) is

$$B_n = \frac{\frac{1}{2\pi}\int_{-\infty}^{\infty} |H(\omega)|^2\ d\omega}{|H(0)|^2} \tag{69}$$

where $H(\omega)$ is the Fourier transform (transfer function of the filter) of $h(t)$. Using Parseval's Theorem

$$B_n = \frac{\int_{-\infty}^{\infty} |h(t)|^2}{|H(0)|^2} = \frac{\int_0^{nT} |h(t)|^2 \, dt}{\left|\int_0^{nT_s} h(t) \, dt\right|^2} \tag{70}$$

Again, it is useful to note that B_n is a function of ν, j, N, and J, so using the V_d conversion formulas of [20], a different V_d ratio will in general be required for each term in Eq. 59.

Recapping, for linear receivers, Eq. 59 can be rewritten as

$$P_{FM}(\varepsilon) < \frac{1}{M} \cdot \frac{1}{m} \sum_{N \neq \nu}^{M} \sum_{J=1}^{m} \sum_{j=1}^{m} \sum_{\nu=1}^{M} \Pr\{y(N,J,\nu,j) > 0\} \tag{71}$$

where the mean of $y(N,J,\nu,j)$ is given by Eq. 65, the variance by Eq. 68, and the effective V_d ratio by knowledge of B_n (Eq. 70) B_1, and the input V_d ratio.

This basic approach to linear receiver performance has been used before [5, 21, 22] for the cases of PSK, MSK, and CFSK modulations.

5.1.2 Nonlinear Receiver Approach

When zero-memory nonlinearities are used in the receiver, the input to the correlators (or matched filters) can no longer be considered impulsive. We have chosen in this case to model the stochastic integral of Eq. 61 as a finite sum using the trapezoidal rule.

$$y = \mathrm{Re} \int_0^{nT_s} z(t) \, h(nT_s - t) \, dt \approx \mathrm{Re}\left\{\frac{\tau}{2}(f(0)+f(L)) + \tau \sum_{\ell=1}^{L-1} f(\ell)\right\} \tag{72}$$

where $f(\ell) = z(t_\ell)\ h\ (nT_s - t_\ell)$ (73)

and $\tau = t_\ell - t_{\ell-1}\ , \quad \ell \geq 1.$ (74a)

and $L = \frac{nT_s}{\tau}$ (74b)

In Eq. 72, h(t) is given by Eq. 62, and again we have suppressed the functional notation of y on ν,j,N, and J.

$z(t_\ell)$ can be expressed in amplitude and phase notation using Eq. 16 as

$$z(t_\ell) = \xi(t_\ell) e^{j\zeta(t_\ell)}. \tag{75}$$

Similarly, $h(nT_s - t_\ell)$ can be expressed in envelope and phase form as (using Eq. 62).

$$h(nT_s - t_\ell) = s^*(t_\ell, d_N, D_J) - s^*(t_\ell, d_\nu, D_j) = h(t_\ell) e^{-j\delta(t_\ell)} \tag{76}$$

Hence,

$$f(\ell) = \xi(t_\ell)\ h(t_\ell)\ e^{j[\zeta(t_\ell) - \delta(t_\ell)]} \tag{77}$$

Using this notation we can rewrite Eq. 72 as

$$y = \sum_{\ell=0}^{L} a_\ell\ \xi(t_\ell)\ \cos\ (\zeta(t_\ell) - \delta(t_\ell)) = \sum_{\ell=0}^{L} a_\ell\ y_\ell \tag{78}$$

where a_ℓ is a constant

$$a_\ell \begin{cases} \frac{\tau}{2} h(t_\ell)\ , & \ell = 0 \text{ and } L \\ \\ \tau h(t_\ell)\ , & 1 \leq \ell \leq L-1 \end{cases} \tag{79}$$

and

$$y_\ell = \xi(t_\ell)\cos\ (\zeta(t_\ell) - \delta(t_\ell)) \tag{80}$$

Two questions arise in the further development of Eq. 78. First, how many samples or points should be used to approximate the integral, and second, what are the statistics of the samples $\xi(t_\ell)$ and $\zeta(t_\ell)$ and how might they be used to determine $Pr\{y > 0\}$, which is the desired computation (see Eq. 61) ? All of the results in this report assume that samples of the signal at time t_ℓ are independent from samples at any other time t_m, $m \neq j$. This implies that samples are taken at the Nyquist rate relative to the baseband equivalent bandwidth of the bandpass zero memory nonlinearity and that the noise is white. If samples are taken at any other rate, there will in general be correlation between samples at t_ℓ and t_m. This can be handled in the theory, but it does complicate the development. (More is mentioned in this regard in Appendix A).

If the number of samples L becomes very large, the law of large numbers can be used to argue that y in Eq. 78 is approximately Gaussian. With this assumption, the pdf of y can be determined with knowledge of only the mean and variance of y. Furthermore, as can be seen from Eq. 78, knowledge of the first and second moments of each of the samples y_ℓ would allow determination of the mean and variance of y. Namely, from Eq. 78

$$E\{y\} = \sum_{\ell=o}^{L} a_\ell \ E\{y_\ell\} \tag{81}$$

and

$$E\{y^2\} = \sum_{\ell=o}^{L} a_\ell{}^2 \ E\{y_\ell{}^2\} + 2 \sum_{\ell=o}^{L} \sum_{\substack{j=o \\ j\neq\ell}}^{L} a_\ell a_j \cdot E\{y_\ell y_j\}. \tag{82}$$

Because of our assumption of independent samples, in Eq. 81, $E\{y_\ell y_j\} = E\{y_\ell\}E\{y_j\}$ and

$$\text{Var}(y) = \sum_{\ell=o}^{L} a_\ell^2 \ \text{Var}(y_\ell) \tag{83}$$

If the number of samples L is not very large ($L<20$), then one approach which can be taken is to use a Gram-Charlier expansion of the pdf of y. This approach has been used previously to determine error rate estimates [22, 23] when nonlinear receives are used on the VLF/LF channel. This technique requires the knowledge of higher moments of the time samples y_ℓ, but it is a general approach which has proven to be useful in many diverse fields and computations for which the Gaussian assumption is not warranted. Details of the present development of this approach is given in Appendix A.

In general, a numerical approach is necessary to determine the moments of the time samples y_ℓ. This is further explained in Appendix A, and it seems to be a result of the following:

The zero-memory nonlinearity is handled as a transformation of random variables on the incoming signal and noise. As a result of these nonlinearities, the output envelope pdf's are finite, i.e. the envelope cannot exceed some point t_h. After more transformation of variables, we arrive at pdf's of each of the y_ℓ's. These pdf's are also finite. Hence, the k^{th} moment of y_ℓ is of the form

$$E\{y_\ell^k\} = \int_a^b y_\ell^k \ p(y_\ell) \ dy_\ell \tag{84}$$

None of the noise models known to the author to date, including those in this study, are sufficiently rich in analytical usefulness that closed form solutions exist for all the computations of interest. It is interesting to note that even in the case

of Gaussian noise, if a nonlinearity is present, integrals such as Eq. 84 cannot always be solved in closed form.

5.2 Simulation Error-Rate Results

In this section, we present the simulation estimates of the probability of error for various CPMFSK modulations. Estimates are presented for CPMFSK of different modulation index M, different deviation ratios h, different V_d ratios, different receiver types, and at a range of signal-to-noise ratios. Because of the vast number of variables of interest, it is of course implausible to display or evaluate results which are exhaustive over the range of these variables. Hence, the emphasis has been to understand trends and the general phenomena of using different receiver structures to process CPMFSK signals which are corrupted by impulsive noise.

From Eqs. 5, 6, and 10, the baseband equivalent signal plus noise is during the i^{th} symbol interval

$$r(t) = \sqrt{\frac{2E_s}{T_s}} \exp\left\{j\left[\frac{d_i \pi h (t-(i-1)T_s}{T_s} + \pi h \sum_{j=1}^{i-1} d_j\right]\right\} + \eta(t)\, e^{j\phi(t)} \tag{85}$$

No filtering effects have been included in the results to be presented in this section, however the received signal plus noise is sampled four times per bit (for quaternary modulation, 8 times per symbol). This implies an RF/IF bandwidth (one-sided) of $2/T_b$ Hz, where T_b is the bit period. Reference to section 3.1 indicates that filters with bandwidths of this magnitude will have negligible distortion effects on the signal, hence the filtering effects were not included in the simulation.

During each iteration within the simulation, n random data symbols are generated which correspond to $d_1, \cdots, d_n$. A complex signal array is then constructed corresponding to the first term on the r.h.s. of Eq. 85. The length of the array is 4n for binary modulation and 8n for quaternary modulation (4 samples per bit X $\log_2$ M x n bits). To this array is added complex noise samples corresponding to the second term in Eq. 85. These noise samples are derived from the simulation noise model described in section 4.2 where the variance of the noise is σ^2 (E_B/σ^2)is an input parameter to the simulation). The phase samples of the noise $\phi(t_\ell)$ are uniformly distributed on the range (0, 2π).

After the signal plus noise is generated, it is either processed in a linear receiver as shown in Figure 1, or it is first passed through one of the nonlinearities of Figure 3 and then processed in the linear receiver. The linear receiver is also a sampled version so that the various voltage outputs can be modeled as a sum rather than the integral of Eq. 19. That is

$$x_{\lambda j} \approx \mathrm{Re} \sum_{k=1}^{4 \log_2 Mn} z(t_k)\, s^*(t_k, d_\lambda, D_j) \qquad (86)$$

The M^n different outputs, $x_{\lambda j}$, are then compared to make a decision on d_1. The number of errors are counted and the simulation program was exercised until enough iterations were taken to assure the estimated error rate was reasonably accurate. To determine this number of iterations, the following calculations were used:

Assume errors occur with a binomial probability p. Hence, in N trials, the expected number of errors is Np and the variance of the errors would be Npq where q=1-p.

For p very small, the ratio of standard deviation to mean is

$$\varepsilon_r \quad \frac{\sqrt{Npq}}{Np} \approx \frac{\sqrt{Np}}{Np} = \frac{1}{\sqrt{Np}} \tag{87}$$

For the bulk of the results in this study, it was desired to have an error bracket $\varepsilon_r = \frac{1}{5}$, i.e. the simulated points are accurate with a one standard deviation range of $\frac{1}{5}$ of the value. From Eq. 87, this implies that Np = 25. For an estimated error rate of $p = 10^{-3}$, up to 25000 iterations would then be required. This indicates the relatively high expense of determining low error rates using Monte Carlo simulation.

Since results can logically be split up depending upon what receiver type was used, the following sections will display results for linear, clipper, and hole punch receivers respectively.

5.2.1 Simulation Results for Linear Receivers

One of the first considerations which must be examined with respect to CPMFSK signaling is the choice of the deviation ratio, h. So far, no general techniques have arisen for determining the optimum h, and different approaches have been used.

The value of h which should be chosen is obviously the one that minimizes the probability of error. Some authors in the past have alternately examined the minimum distance criterion, wherein a value of h is chosen which maximizes the minimum distance between pairs of signals in the signal set [3, 24]. In this study, an attempt was made to find the value of h for which $Pr_M(\varepsilon)$ was smallest.

Table 6 shows the error rate results for various binary CPFSK signals, including MSK (h=1/2). The results were generated at 3 different V_d ratios, however at each V_d ratio only one signal-to-noise ratio (E_B/σ^2) was used.

Table 6: Error Rates for Binary CPFSK vs. Deviation Ratios

h	V_d = 2 dB E_B/σ^2 = 3 dB	V_d = 8 dB E_B/σ^2 = 3 dB	V_d = 14 dB E_B/σ^2 = 3 dB
.4	2.45×10^{-2}	2.13×10^{-2}	1.26×10^{-2}
.5	2.44×10^{-2}	1.96×10^{-2}	1.30×10^{-2}
2/3	1.5×10^{-2}	1.53×10^{-2}	1.1×10^{-2}
.715	1.46×10^{-2}	1.36×10^{-2}	1.06×10^{-2}
.75	1.48×10^{-2}	1.46×10^{-2}	1.1×10^{-2}
.8	1.77×10^{-2}	1.50×10^{-2}	1.1×10^{-2}

All the data except for h = 0.5 was derived with a reciever of memory length n = 3, i.e. three bit are observed before a decision is made.

Three things must be noted with respect to the data of Table 6:

(1) The data is derived from simulation results, so there is a certain amount of expected randomness in it.

(2) The error rates for values of h other than those listed is not necessarily a smooth function which could be surmised from interpolation. [3] This is why the data was presented tabularly rather than in a figure. The h's which were investigated were found to be locally optimum points on the

Gaussian channel, but this statement cannot be made in general on the impulsive channel.

(3) The signal-to-noise ratio (E_B/σ^2) was kept constant, so it is conceivable that other values of h could be better at different E_B/σ^2

Nonetheless, the data does indicate that h = .715 (which was found optimum in the Gaussian case) is a good choice for binary communications when error rate is the primary consideration.

Table 7 shows similar data for quaternary CPMFSK signaling. Again all data was derived using n = 3 which implies a receiver with memory extending over 3 symbols.

Table 7: Error Rates for Quaternary CPMFSK vs. Deviation Ratio

h	V_d = 2 dB E_B/σ^2 = 0 dB	V_d = 8 dB E_B/σ^2 = 0 dB	V_d = 14 dB E_B/σ^2 = -3 dB
.4	6.3×10^{-2}	3.33×10^{-2}	3.47×10^{-2}
.5	6.4×10^{-2}	3.87×10^{-2}	3.87×10^{-2}
.6	4.8×10^{-2}	3.73×10^{-2}	4.0×10^{-2}
.8	4.53×10^{-2}	3.06×10^{-2}	2.94×10^{-2}
.9	6.67×10^{-2}	3.33×10^{-2}	3.07×10^{-2}

The same three cautions given above also of course apply to Table 7. h values of .4, .6, and .8 were shown to achieve good performance improvement on the Gaussian channel. h = .5 is minimal orthogonal spacing. From Table 7, it appears that h = .4 and .8 still achieve error rates lower than orthogonal signaling, however h = .6 does not seem to be as good for V_d = 14. This could be a statistical anomaly.

It was determined that for linear receivers, the best signaling scheme in terms of probability of error is quaternary CPMFSK with h = .8. This agrees with previous Gaussian results [4]. All of the other binary and quaternary signals which achieved better error rates than MSK were somewhere between MSK and quaternary CPMFSK with h = .8. Consequently, all the data on linear receivers and most of the data on nonlinear receivers will be presented in terms of MSK performance and quaternary CPMFSK with h = .8 performance. The MSK performance can be considered a benchmark because it has been used on some impulsive channels (VLF/LF) and it is the minimum orthogonal frequency spacing. The quaternary CPMFSK with h = .8 signaling is the best that has been found so far in terms of error rate vs. E_B/σ^2. It is probably a reasonable assumption to imagine that all the other modulations which are better than MSK would achieve error rates between MSK and quaternary CPMFSK with h = .8.

A curve showing the linear receiver error rate performance of MSK and quaternary CPMFSK with h = .8 for three different V_d ratios is shown in Figure 20. The degradation caused by impulsive noise is apparent from the flattenning of the curves as the noise becomes more impulsive (higher V_d ratio).

In Figure 20 the probability of bit error is plotted with respect to E_B/σ^2 where E_B is the received energy per bit and σ^2 is the variance of the impuslive noise. For M-ary modulation, the received energy per symbol E_s is related to E_B by

$$E_s = \log_2 M \cdot E_B \tag{88}$$

Again, it is reiterated that Figure 20 is the result of Monte Carlo simulation, so that plotted points are expected to have some statistical jitter on them. Nonetheless, it is seen that CPMFSK can offer improvement in E_B/σ^2 from 1.5 dB to 3.5 dB at error rates of 10^{-3}. This corresponds to the 2.3 dB improvement

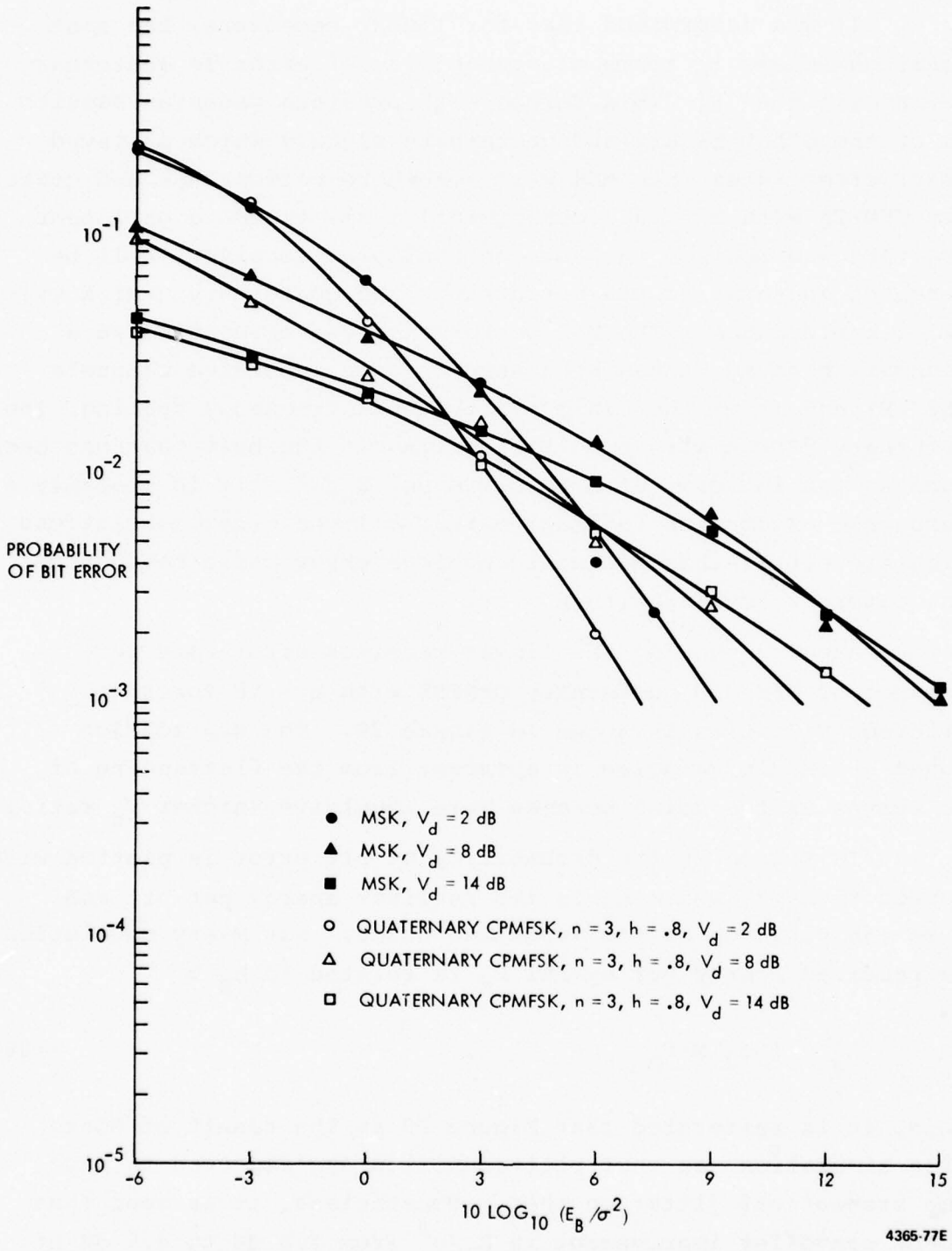


Figure 20: Linear Receiver Performance

possible on the Gaussian channel[4] at the same error rate. On the other hand, as mentioned above, the overall performance of the linear receiver is much worse when impulsive noise rather then Gaussian noise is present. This was to be expected from theoretical studies [12, 16, 25, 26] which derived optimum receiver structures. Although the details of these structures depend upon knowledge of the noise pdf, it is clear that for impulsive noise, linear receivers are decidedly suboptimum.

5.2.2 Simulation Results for Nonlinear Receivers

In addition to the considerations given in the last section on linear receivers, additional related considerations must be addressed in the case of nonlinear receivers. Only nonlinear receivers which are composed of the linear receiver of Figure 1 preceded by zero-memory nonlinearities are considered in this study. Furthermore, only two types of nonlinearities are considered, namely the hole punch (or blanker) and the clipper. The transfer functions of these are shown in Figure 3. For both of these nonlinearities, one further parameter to investigate is the threshold level t_h. All results in this study were determined where the threshold level is set relative to the mean of the signal plus noise envelope. As indicated in Eq. 9, the received signal preceding the nonlinearity can be represented as

$$r(t) = \mathrm{Re}\left\{ v(t)e^{j\alpha(t)}e^{j\omega_c t}\right\} \tag{89}$$

The threshold level can then be represented as

$$t_h = k\int_{\sigma}^{\infty} vp(v)\,dv = k\bar{v} \tag{90}$$

where $p(v)$ is the pdf of the signal plus noise envelope, and k is a proprotionality constant. Results are displayed with t_h indicated in dB relative to $\bar{v}$.

Figure 21 shows a plot of $\bar{v}$ for three different V_d ratios and a normalized signal energy $E_B = 1$. The simulation noise model explained in Section 4.2 was used and results are displayed as a function of E_B/σ^2. Clearly, as E_B/σ^2 gets larger, $\bar{v}$ approaches 1 as expected. The rest of this section presents results for the clipper and hole punch nonlinear receivers.

5.2.2.1 Clipper Results

The nonlinear clipper has an envelope transfer function as shown in Figure 3a. It is perhaps the most commonly used nonlinearity for noise suppression. The technique shown in Figures 22 and 23 was used to determine the optimum threshold. The signaling waveform, noise V_d ratio, and E_B/σ^2 were all fixed while the nonlinearity threshold t_h was varied. Threshold values of 0, $\pm$1, $\pm$2, $\pm$3, $\pm$6, and $\pm$10 dB relative to $\bar{v}$ were investigated. Although E_B/σ^2 remained fixed for each curve, as can be seen in the figure, different E_B/σ^2 were used for different signals and V_d ratios. This was done to more clearly display the effect of varying t_h. As is seen in Figure 22, the best threshold setting in the investigated range for the MSK signals is -10 dB relative to $\bar{v}$. On the other hand, in Figure 23, the curves for V_d = 2 dB and V_d = 8 dB show a clear improvement for t_h = -2 dB and -6 dB relative to $\bar{v}$ respectively. It is suspected that optimum threshold values might exit below -10 dB for the other signals and V_d ratio, but these were not investigated. For each of the points in Figures 22 and 23, the Monte Carlo noise model was exercised from the same starting number. Hence, the relative differences between points should be fairly accurate.

Figure 24 shows the probability of bit error when the optimum clipper threshold was chosen. The word 'optimum' is used where it is understood that the threshold setting is in the range as shown in Figures 22 and 23. A number of things become clear when investigating Figure 24. For one thing, comparison with Figure 20 shows that significant performance improvement

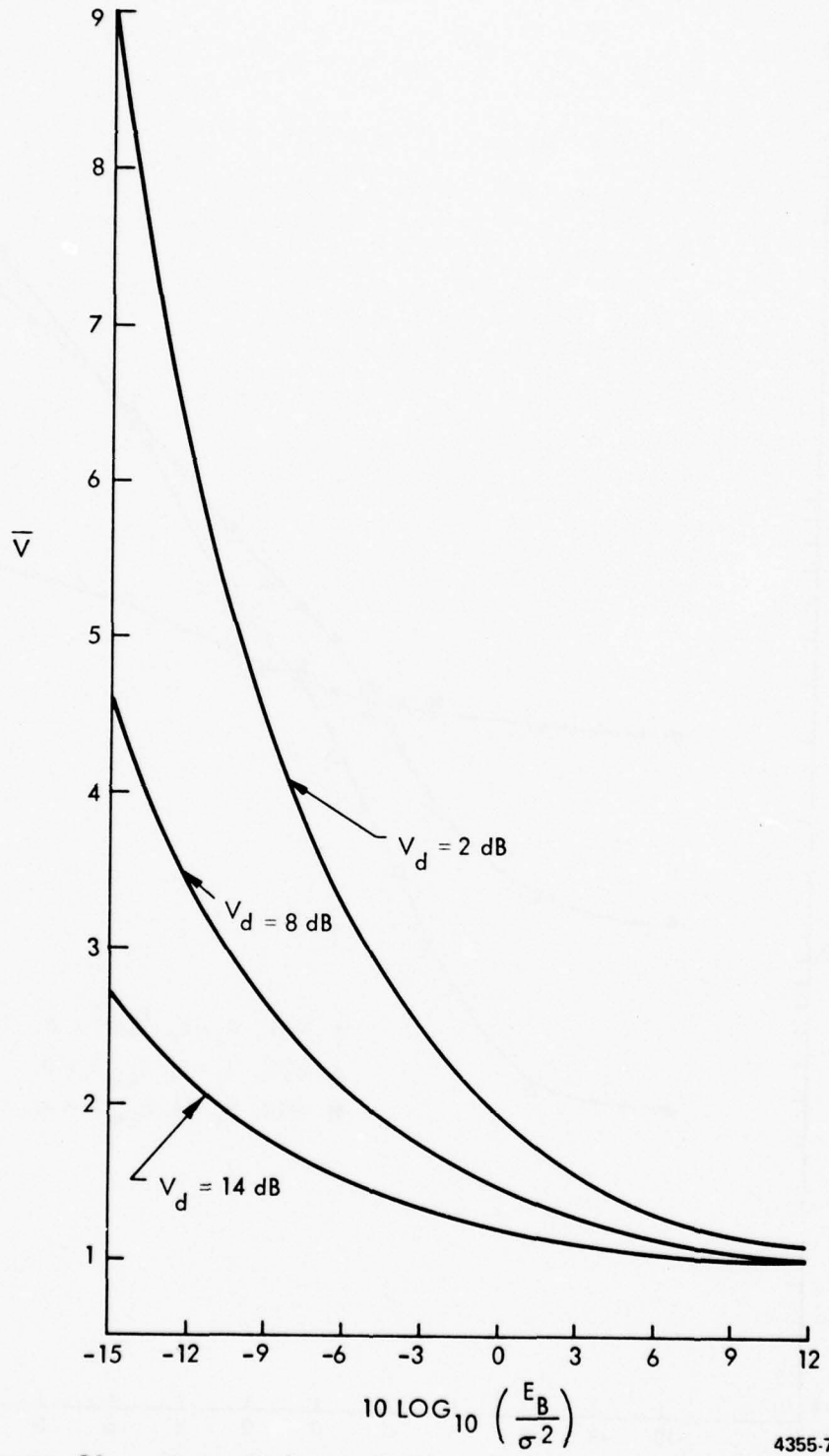


Figure 21: Mean Value of Signal Plus Noise Envelope vs. $10 \log_{10} \frac{E_B}{\sigma^2}$

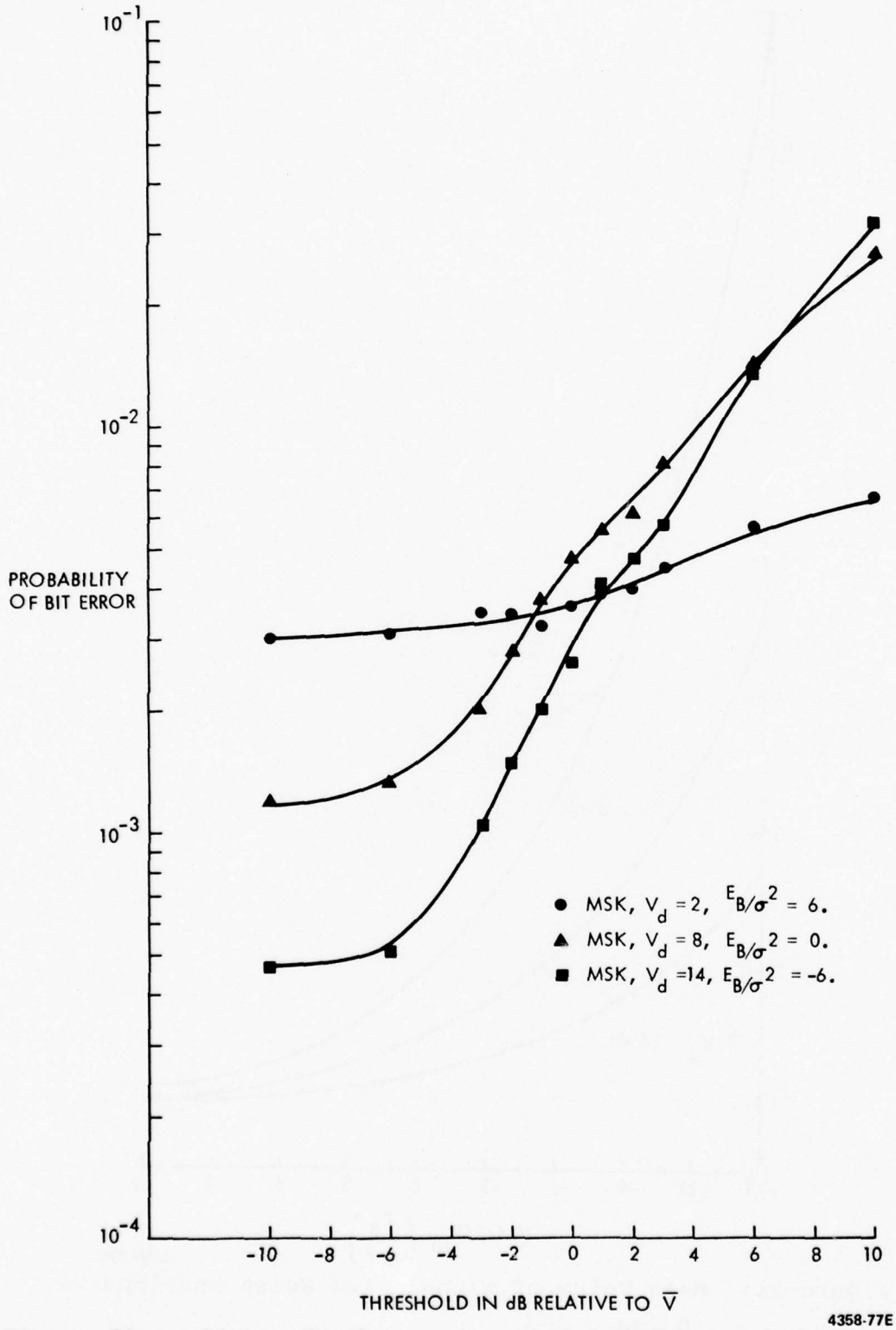


Figure 22: Clipper Performance vs. Threshold Level (Binary)

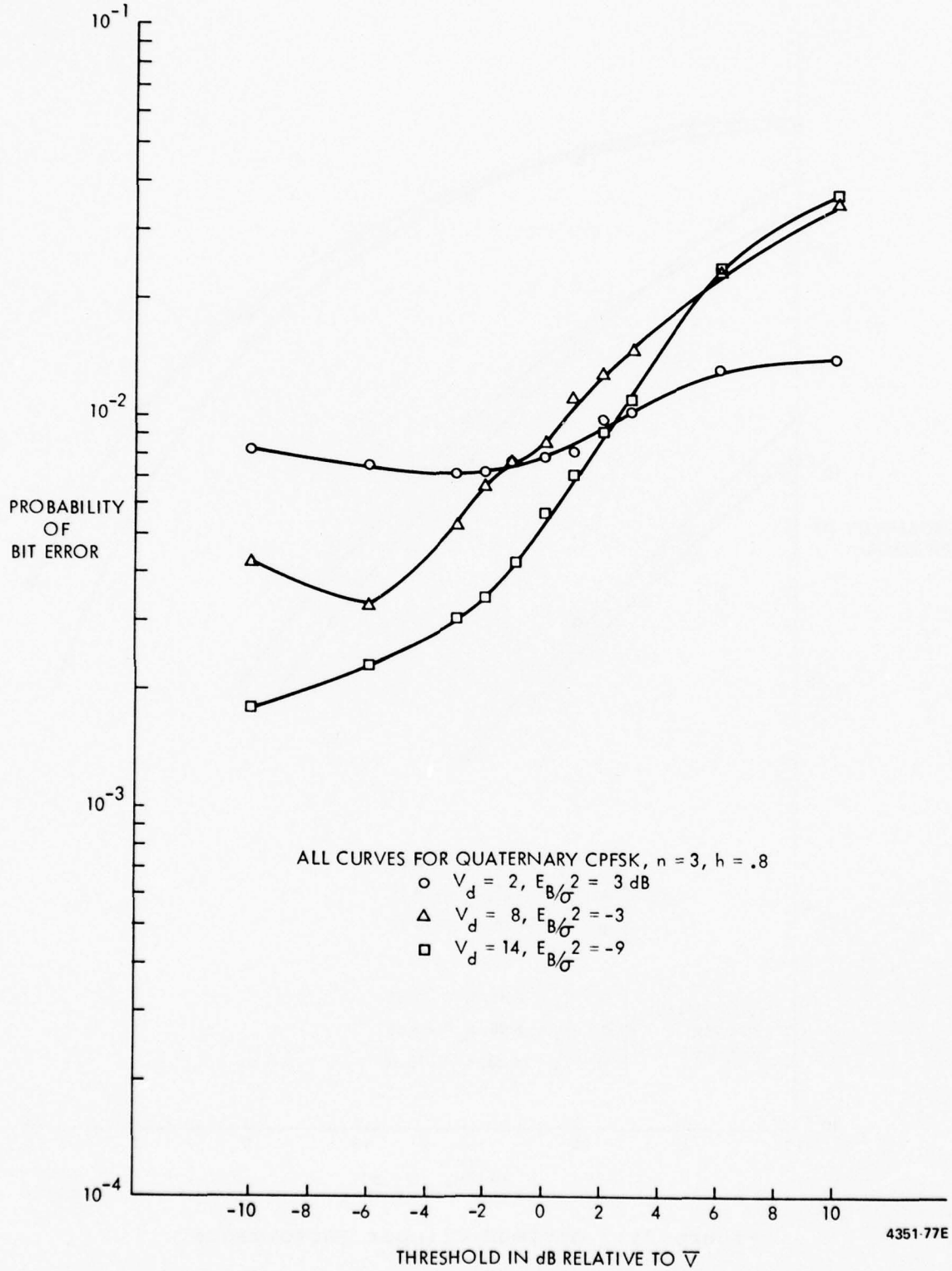


Figure 23: Clipper Performance vs. Threshold Level (Quarternary)

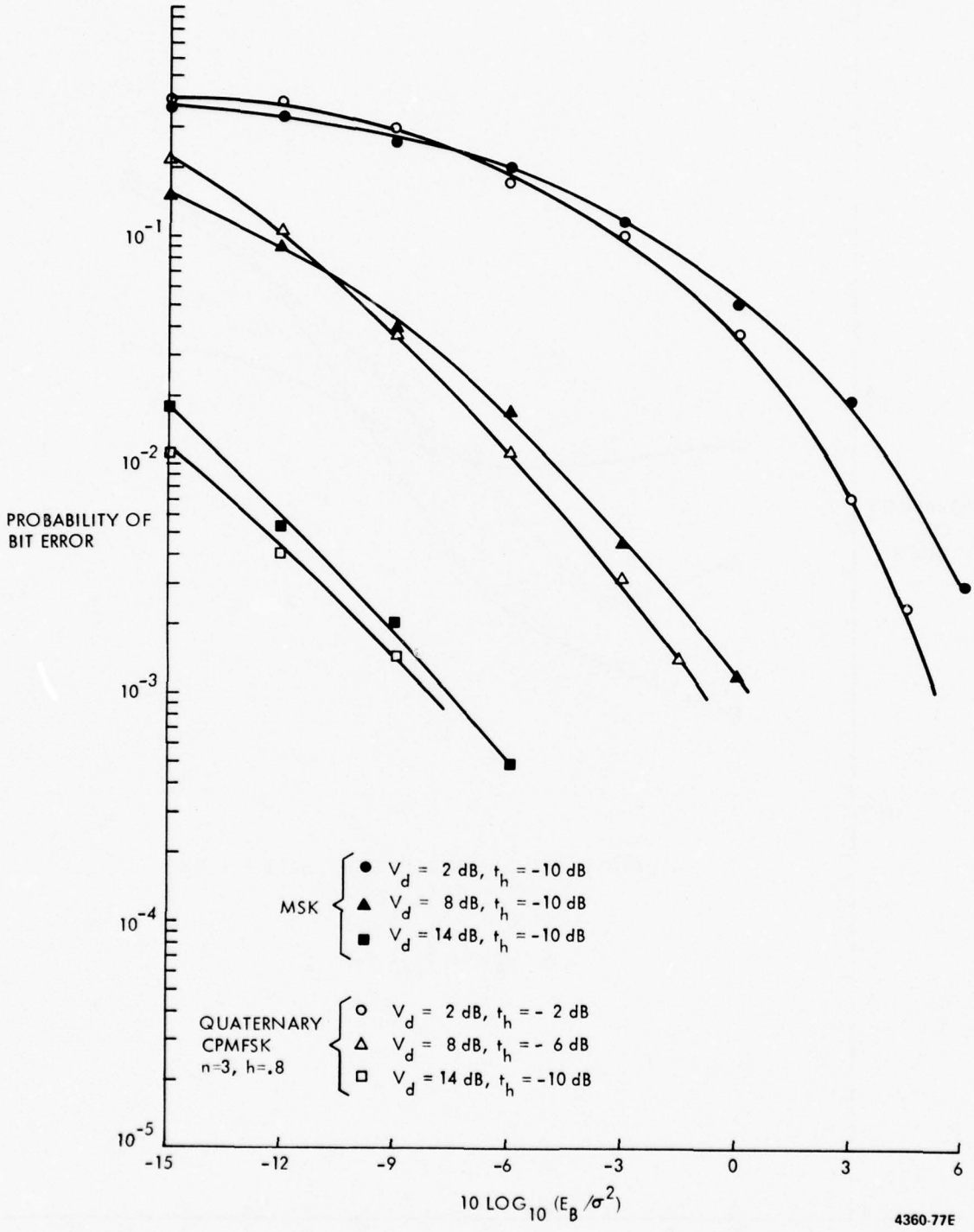


Figure 24: Optimum Clipper Performance

over linear receivers can be achieved when nonlinear noise suppression techniques are used. The improvement in E_B/σ^2 is on the order of 1.5 dB when the V_d ratio is 2 dB, however it is on the order of 21 -22 dB when the V_d ratio is 14 dB. These improvement are for error rates of 10^{-3}.

It is also clear from Figure 24 that CPMFSK still achieves a lower error rate than MSK at the same E_B/σ^2, however the performance improvement does not seem to be as great when nonlinear receivers are used as when linear receivers are used. Not only is the E_B/σ^2 improvement of CPMFSK over MSK not as great in Figure 24 as it is in Figure 20, but the improvement seems to become less as the noise becomes more impulsive. For example, at error rates of 10^{-3}, CPMFSK offers an advantage in E_B/σ^2 over MSK of $\approx$3 dB for V_d = 2 dB, whereas the improvement appears to be about 0.5 dB for V_d = 14 dB. On the other hand, it must be remembered that all the points in Figure 24 are derived from simulation so there is a certain expected randomness in their accuracy. Also, simulation expenses precluded the determination of points much below 10^{-3}, so it is unclear if the V_d = 14 dB curves will tend to diverge at low error rates as it appears the lower V_d curves do.

The importance of picking the correct threshold level t_h is again shown in Figure 25, where all results are shown for a threshold setting $t_h = \bar{v}$ (0 dB). Comparison with Figure 24 shows that for V_d ratios of 8 and 14 dB, the optimum threshold setting achieves perforance improvements (required E_B/σ^2 for bit error rates of 10^{-3}) of 2-3 dB over what would be achieved if t_h were simply chosen to be $\bar{v}$.

5.2.2.2 Hole Punch Results

The nonlinear hole puncher has an evelope transfer function as shown in Figure 3b. As in the case of the clipper, an investigation of the optimum threshold setting t_h was done for the hole punch. Results are shown in Figures 26 and 27. In

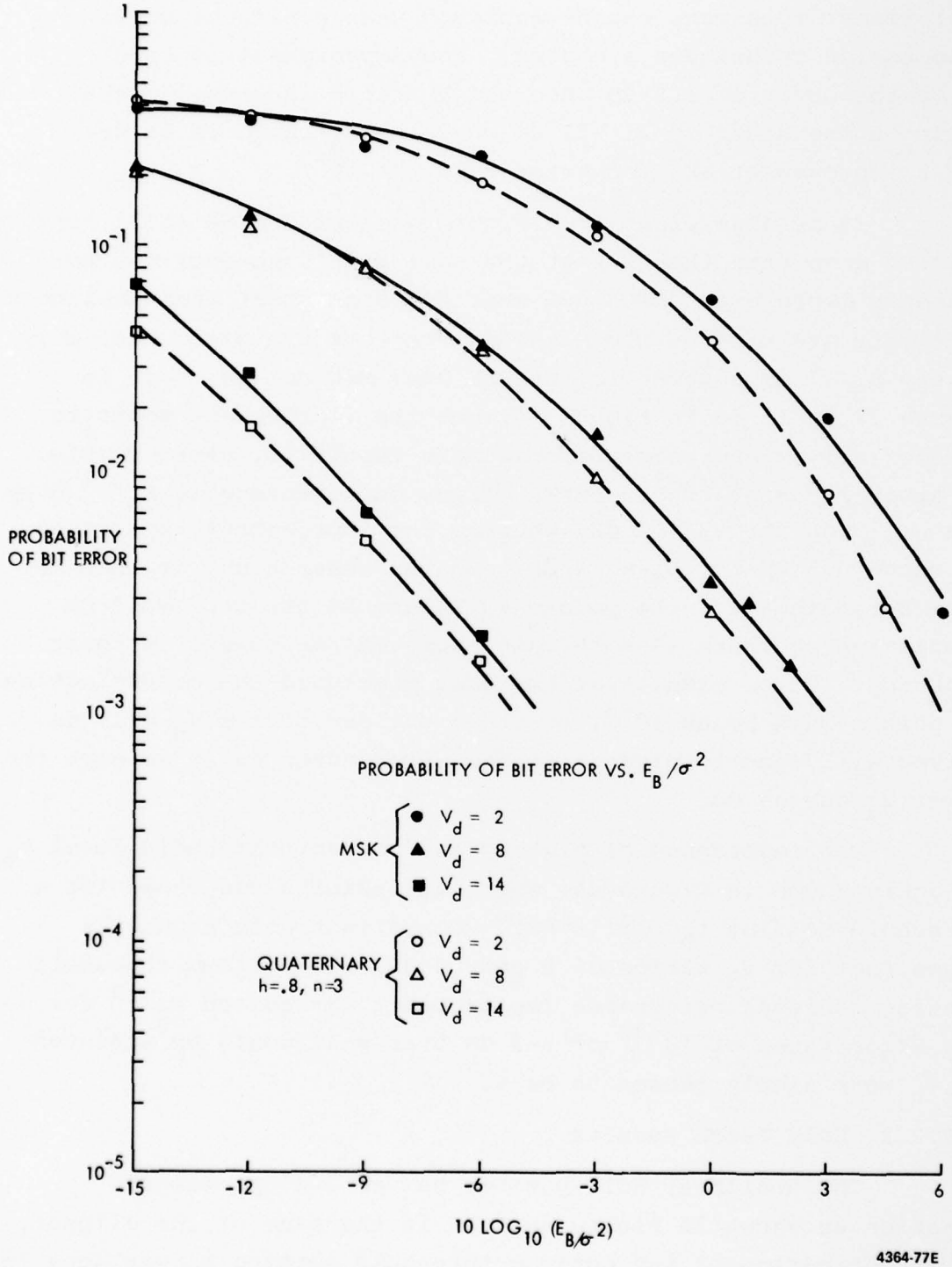


Figure 25: Clipper Performance Threshold @ 0 dB

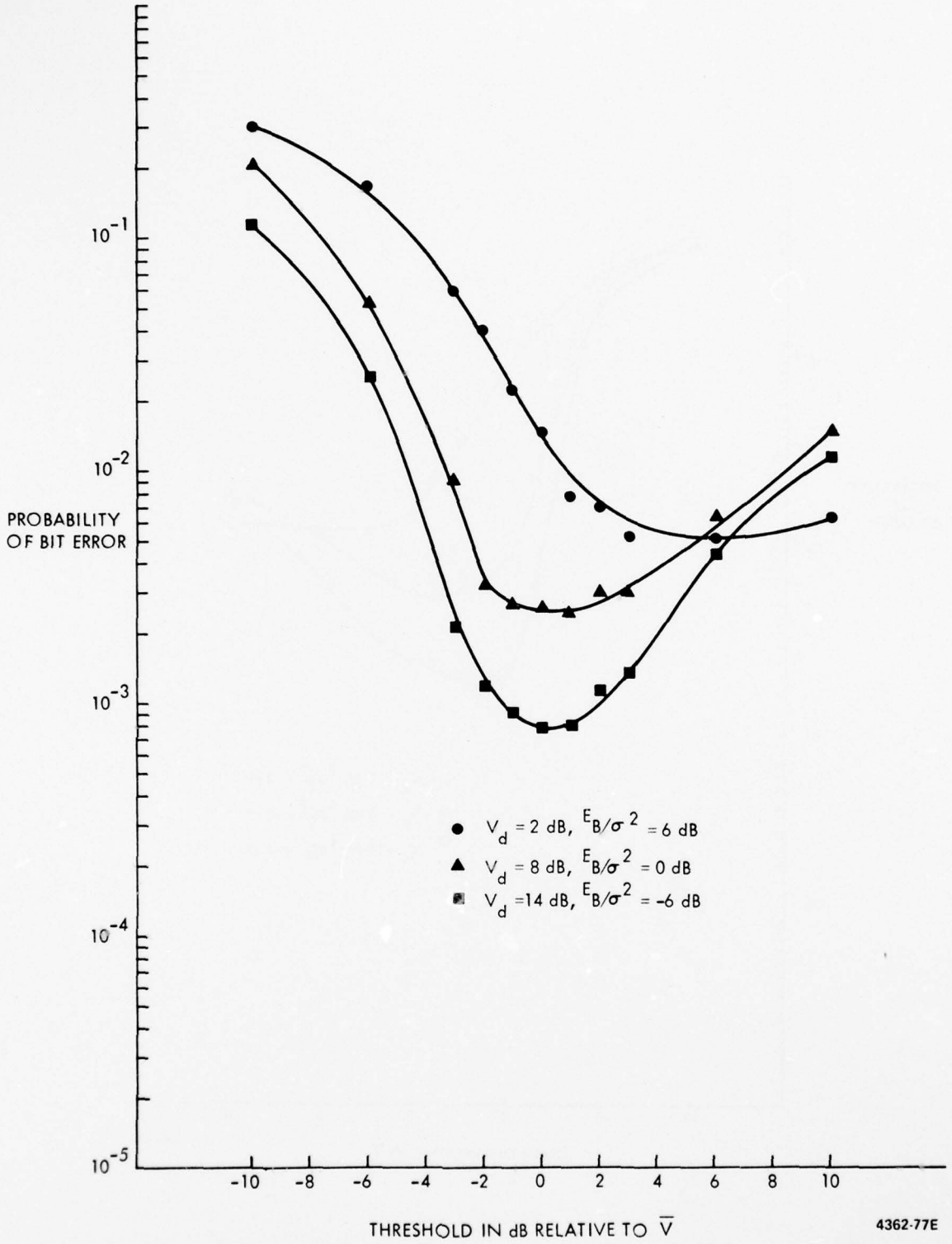


Figure 26: Hole Punch Performance vs. Threshold Level (Binary)

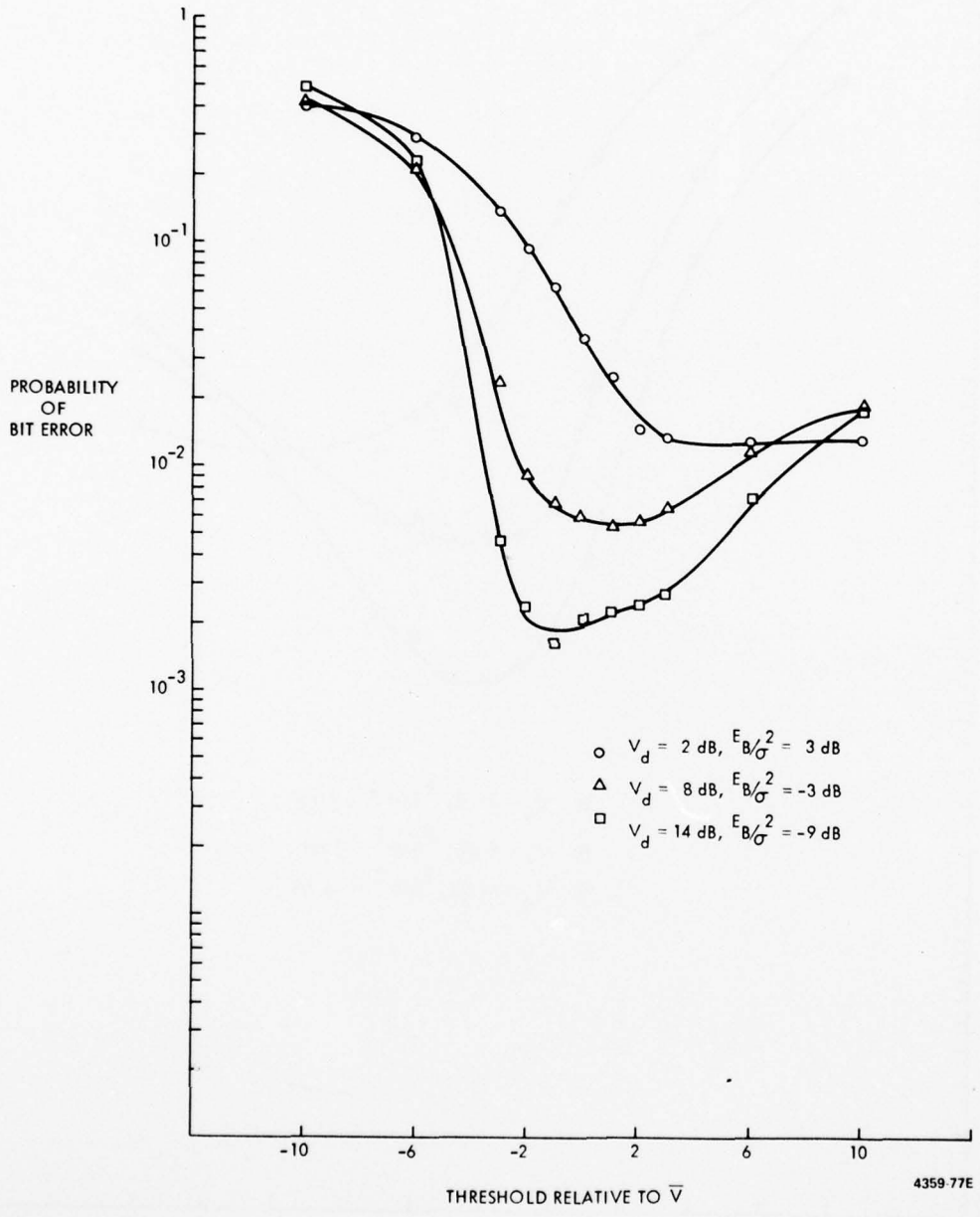


Figure 27: Hole Punch Performance vs. Threshold Setting (Quaternary)

contradistinction to the variation of clipper error rate vs. t_h, Figures 26 and 27 show that hole punch performance is very sensitive to t_h and optimum values of t_h are more evident. Also, all of the optimum values of t_h are greater than or equal to -1 dB relative to $\bar{v}$. This is intuitively satisfying because it indicates that performance degrades if the threshold value is set at a value lower than the desired signal level.

Figure 28 shows the error rate results when the optimum threshold setting is used. Again, it is clear that nonlinear processing of the signals can achieve significantly improved performance over the linear receiver (refer to Figure 20). On the other hand, comparison of Figures 24 and 28 shows that optimum hole punch performance is not as good as optimum clipper performance, where again the E_B/σ^2 required to achieve an error rate of 10^{-3} is used as a criterion for goodness.

Figure 29 shows the error rate curve if the threshold value t_h is set equal to $\bar{v}$. Since the optimum thresholds are close to $\bar{v}$ from Figures 26 and 27 for all curves except V_d = 2 dB, the error rate curves are not significantly different from Figure 28. Comparison with Figure 25 shows that the hole puncher with $t_h = \bar{v}$ outperforms the clipper with $t_h = \bar{v}$ for V_d = 8 and 14 dB impulsive noise ratios. This is pontentially useful in a situation where an AGC-type signal can estimate $\bar{v}$ but little or no knowledge is available about the V_d ratio. In such a situation, it might be desirable to set the threshold level approximately equal to $\bar{v}$ and a hole punch can give better performance than a clipper for largely impulsive noise (V_d ratio high).

Both Figures 28 and 29 show that CPMFSK can still outperform MSK when hole punchers are used. However, there is a tendency for performance improvement of CPMFSK over MSK to become less pronounced as the noise becomes more impulsive (higher V_d). This was also seen in the case of noise suppression by clipping (Section 5.2.2.1).

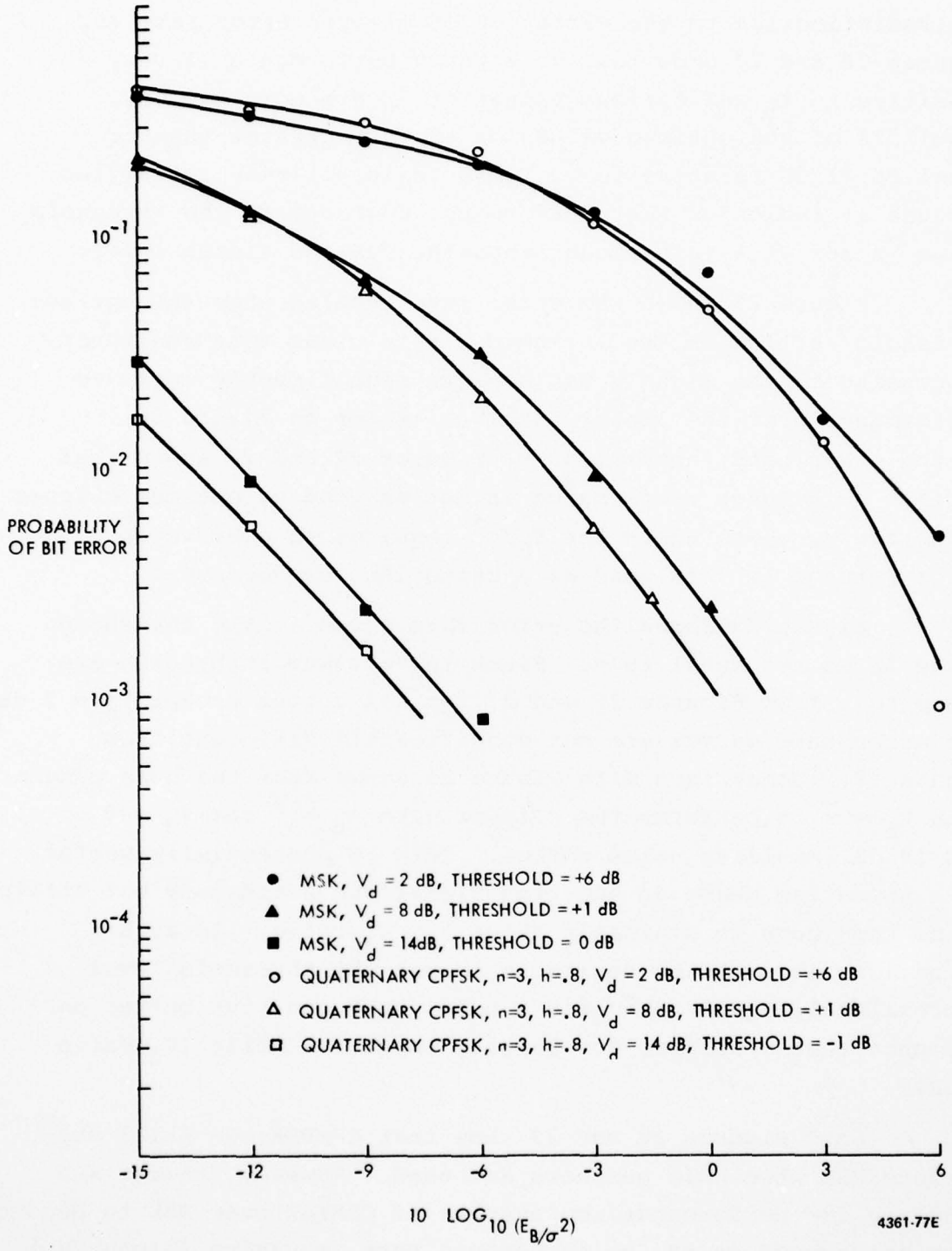


Figure 28: Optimum Hole Punch Performance

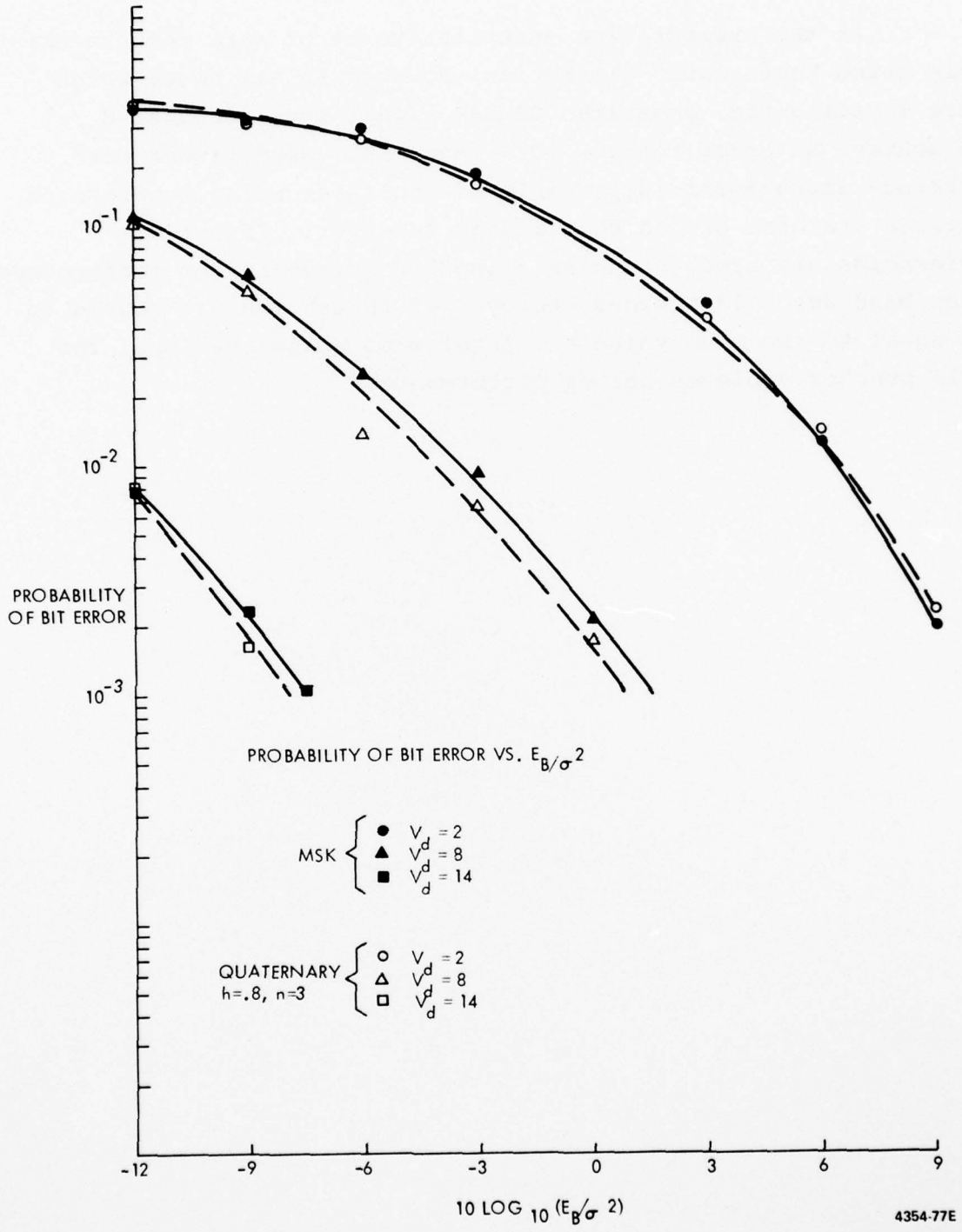


Figure 29: Hole Punch Performance Threshold @ 0 dB

5.3 Summary of Error Rate Results

At the present time quantitative error rate results exist only using Monte Carlo simulation, however in all cases which were investigated, a general CPMFSK signal required less E_B/σ^2 to achieve an error rate of 10^{-3} than MSK. Significant performance improvement is possible if nonlinear noise suppression devices are used preceding a linear receiver. If optimum thresholds are used, bandpass clippers achieve better performance than bandpass hole punches, however if thresholds are chosen to be equal to the mean value of signal plus noise envelope, the hole puncher achieves better performance.

6.0 Power Spectra for CPMFSK

The one-sided power spectral density for CPMFSK is known from [1] and can be written in a normalized form as

$$\frac{G(\beta)}{A^2 T_s} = \frac{1}{M} \sum_{n=1}^{M} \left[\frac{1}{2} \frac{\mathrm{Sin}^2 \gamma_n}{\gamma_n^2} + \frac{1}{M} \sum_{m=1}^{M} B \frac{\mathrm{Sin}\gamma_n}{\gamma_n} \frac{\mathrm{Sin}\gamma_m}{\gamma_m} \right] \tag{91}$$

where

$$A^2 = \frac{E_s}{T_s}$$

$$\beta = \frac{(\omega - \omega_c) T_s}{2\pi},$$

$$\gamma_n = (\beta - \frac{d_n h}{2})\pi, \tag{92}$$

$$B = \frac{\mathrm{Cos}(\gamma_n + \gamma_m) - C\ \mathrm{Cos}(\gamma_n + \gamma_m - 2\pi\beta)}{1 + C^2 - 2C\ \mathrm{Cos}\ 2\pi\beta},$$

and

$$C = \frac{2}{M} \sum_{n=1}^{M/2} \mathrm{Cos}\pi h(2n - 1)$$

This is a formidable looking set of expressions, but they are relatively easy to calculate on a computer. Figure 30 shows the results for the special case of MSK (h = .5) whereas Figures 31 and 32 show the results for binary and quaternary modulation. Also indicated on the figures are the numerically determined 50 percent and 99 percent normalized bandwidth.

It must be noted that Figure 32 is plotted in terms of the symbol time T_s and symbol energy E_s whereas Figures 30 and 31 are plotted in terms of the bit time T_B and bit energy E_B.

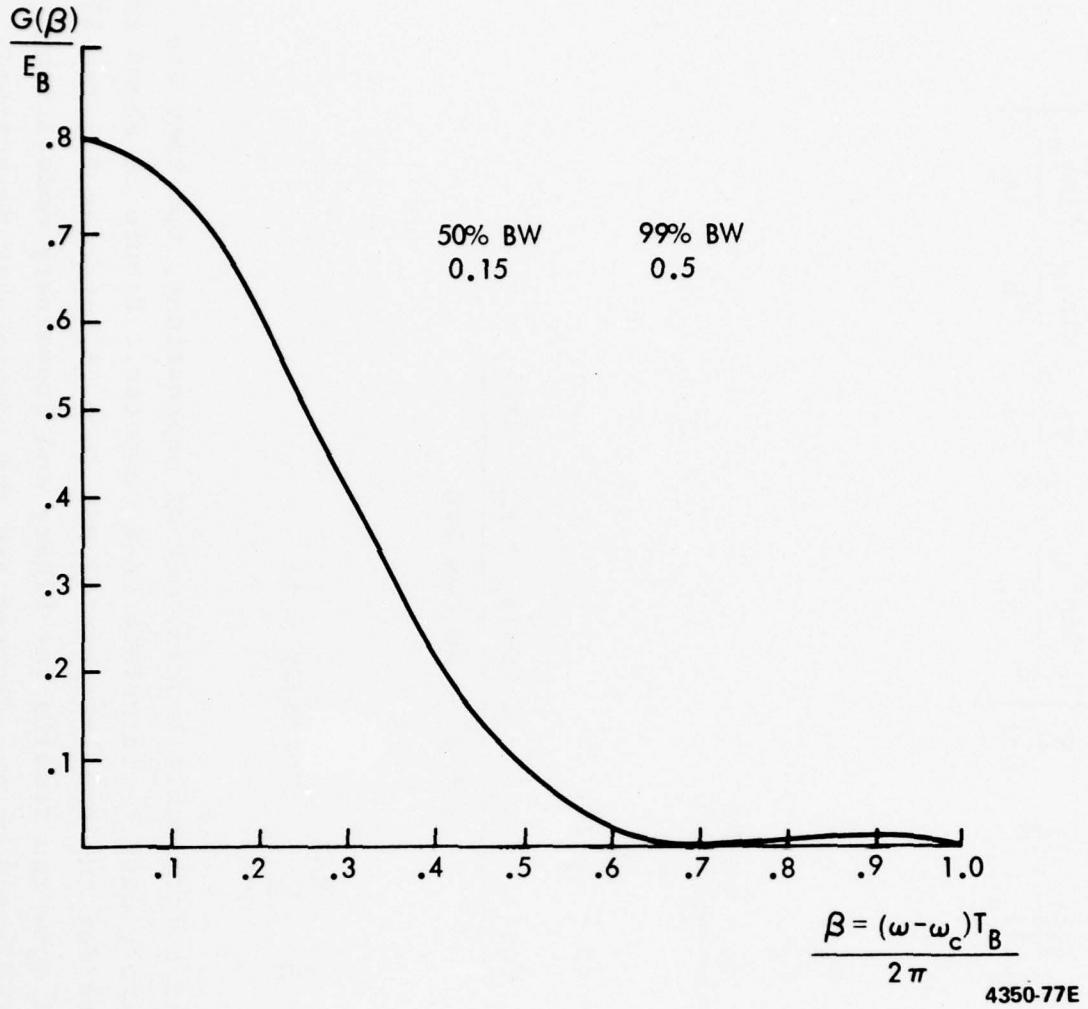


Figure 30: One-Sided Spectrum of MSK

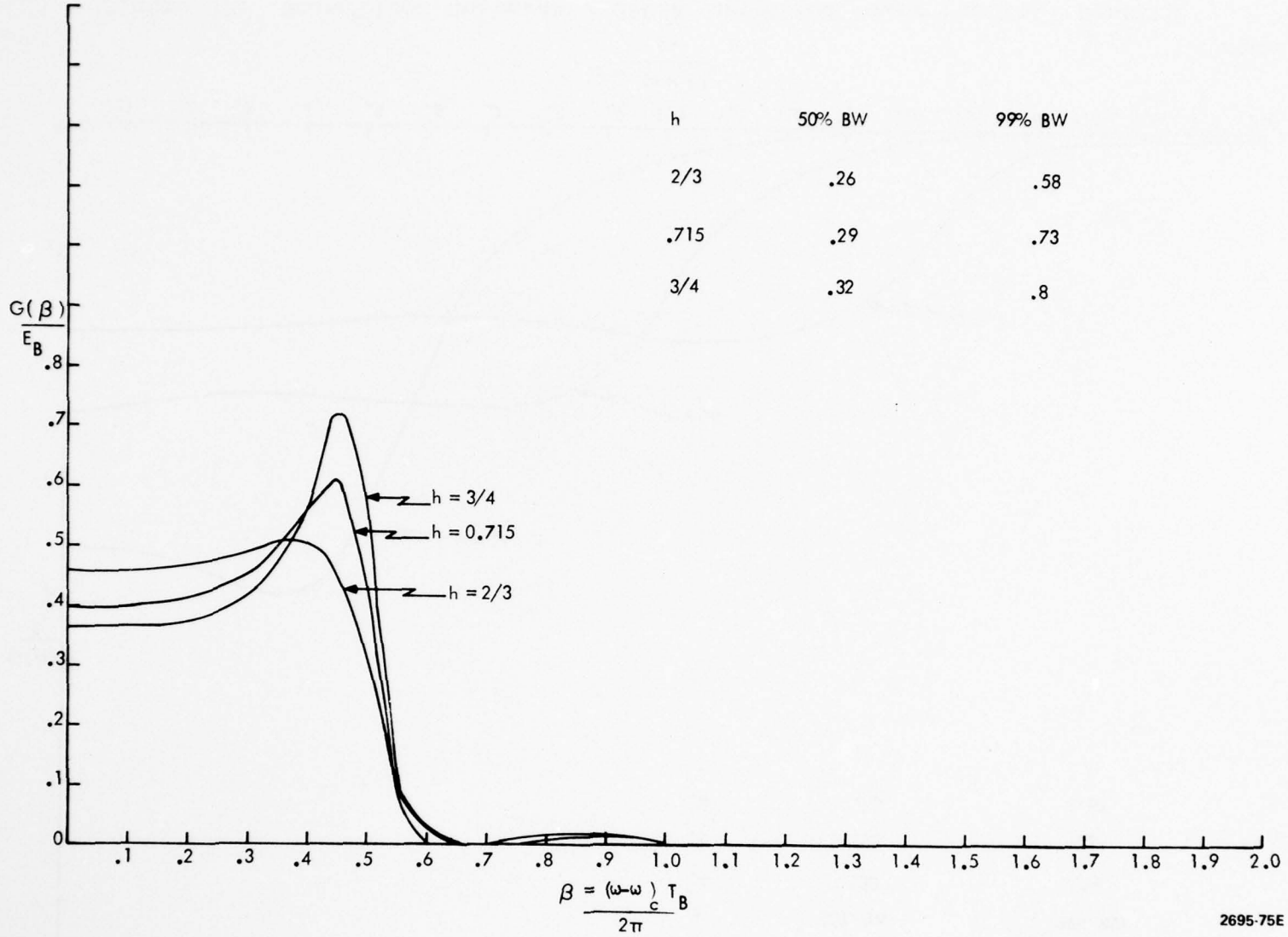


Figure 31: Normalized Binary CPFSK One-Sided Power Spectral Density

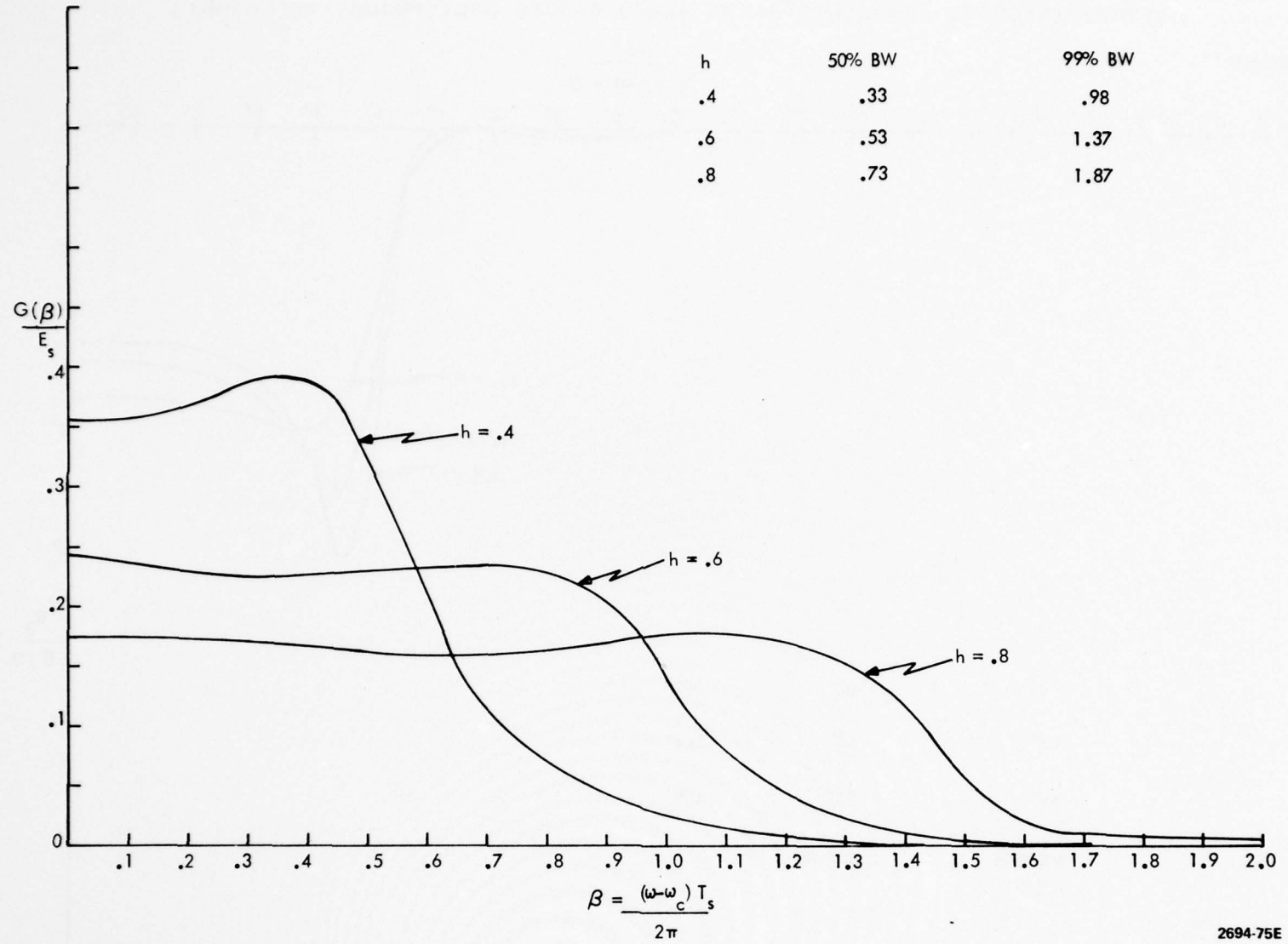


Figure 32: Normalized Quaternary CPFSK One-Sided Power Spectral Density

The two are related by Eq. 88 and

$$T_s = \log_2 M \cdot T_B \tag{93}$$

so that if Figure 32 were plotted in terms of T_B and E_B, the curves would appear twice as high and half as narrow as they do in Figure 32. The quoted 50 percent and 99 percent bandwidths of Figure 32 would also be halved. This is shown in Figure 33 which displays again the spectra of MSK and quaternary CPMFSK with h = .4, where both curves are plotted on the same scale. It is interesting to note that the quaternary CPMFSK with h = 0.4 has a smaller 99 percent bandwidth than MSK.

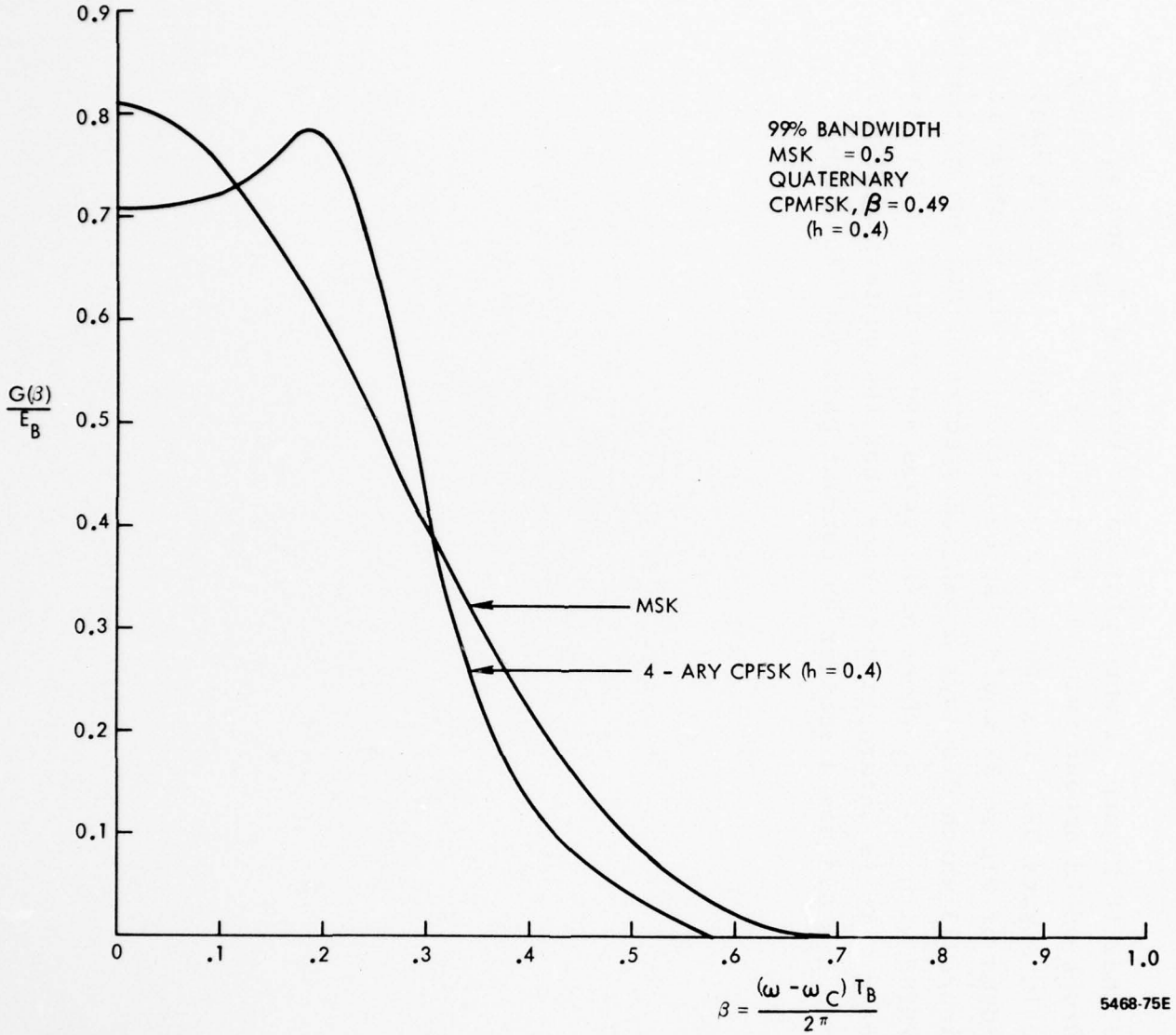


Figure 33: Normalized Spectra of MSK and Quaternary CPMFSK (h = 0.4)

7. Conclusions and Recommendations for Further Work

The results of this study show conclusively that the use of CPMFSK as a modulation on channels with additive atmospheric noise requires less signal to noise ratio to achieve a given error rate than would be necessary with more conventional modulations such as PSK, MSK, or CFSK. Furthermore, transmitted signal power spectral densities have comparable or smaller 99% bandwidths than these more conventional modulations.

A Monte Carlo simulation to determine error rate performance was developed and exercised. A theoretical approach to determine error rate based upon a Gram-Charlier series was formulated, however time constraints precluded its full development and appraisal.

Specific recommendations for further work include the following:

1. The theoretical approach should be further investigated to determine its applicability and feasibility. If the approach proves to be feasible, the following subjects should be investigated.

   a) Determine the optimum deviation ratios to ascertain if they differ from those which are optimum in Gaussian noise.

   b) Determine the effect of correlated noise on the error rate performance.

2. Other additive atmospheric noise models may be more amenable to either analytic determination of required parameters or to quicker numerical determinations. This should be investigated.

3. In the HF band, fading becomes an important signal impairment along with additive atmospheric noise. These fading effects should be included in both the theoretical and simulation phases of the study.

4. A hardware development to determine implementation and quantization losses should be instigated.